

# High Precision Raman Lasers

By

Muye Li

A thesis submitted to Macquarie University for the

degree of Doctor of Philosophy

Department of Physics and Astronomy,

Faculty of Science and Engineering

April 2021





This thesis is submitted to Macquarie University in fulfilment of the requirement for the Degree of Doctor of Philosophy.

The work presented in this thesis is, to the best of my knowledge and belief, original except as acknowledged in the text. I hereby declare that I have not submitted this material, either in full or in part, for a degree at this or any other institution.

---

Muye Li

# Acknowledgements

I would like to express my gratitude to all those who supported me during my PhD candidature. Without their care and assistance, there would not be the fruits of my PhD.

First and foremost, to my supervisor, David Spence, thank you for giving me this opportunity. Only you gave me a positive response among the two hundred emails I sent to all over the world. Your elastic thoughts, and great perception when solving the issue really inspired me a lot. The way you showed me how to build models and explain the laser world is very interesting. It expanded my research skills and knowledge, and I am not scared of theoretical work anymore.

To my "real" co-supervisor, and also my big brother, Ondrej Kitzler (no typo :P). Thank you for your patience and help with everything I encountered in the lab every day. The interesting discussions with you always benefited me a lot. As a recognized fireman in our group, you are so busy as a bee every day. Sorry to encroach on your time. Hope I can see you on steam in the near future.

I would also like to thank all colleagues in the group, your projects in the meeting were nice and interesting, they broadened my horizon and enriched my experience. Special thanks to Rich and Helen for your support and advice in my work and life. I am also grateful to the staff teams for their support and care.

---

To my family, thank you for your encouragement and support, without you, I may not have the courage to start my PhD career.

To my dearest wife, thank you for forgiving me for my caprice and being in Australia for me. Thank you to make my PhD life colorful and abundant with joy. I am honored to share the rest of my life with you.

To myself twenty years ago, thanks to my stupid insistence on lasers. En Taro laser!

# Abstract

Solid-state Raman lasers have emerged as powerful technology for wavelength shifting of conventional lasers. After recent advances in diamond growth technology, there is interest in diamond Raman lasers (DRLs) owing to their supreme thermal performance. While steady progress has been made in high-power Raman lasers including access to a wider range of wavelengths, single longitudinal mode (SLM) operation of Raman laser is a less-studied topic of investigation. Also, to date little effort has been made in the field of Raman cavity-enhanced pumping. In this thesis, we investigate cavity enhanced pumping of cascaded Raman lasers, both theoretically and experimentally.

A theoretical model was derived to describe the behavior of the pump resonant Raman lasers. The model can describe the output performance of such lasers for arbitrary cascading of the Stokes process. The impact of the configuration parameters of the cavity (e.g., beam radius, mirror reflectivities, crystal length etc.) on laser performance are analyzed. The equations for optimum mirror designs are derived and studied.

We design and build several different pump resonant Raman lasers to verify the model and generate commercially-useful laser designs. A diamond Raman laser pumped at 851 nm achieved up to 364 mW of second Stokes output at 1101.3 nm, with stable SLM output up to 140 mW. The slope efficiency was 33%. Under 1064 nm pumping, we generated 1548 mW of second Stokes lasing at 1485 nm using 17.05 W of pump power. For the further verification of our model, a vanadate-based pump resonant Raman laser was built. This laser reached 417.5 mW of second Stokes lasing with a slope efficiency 10% using 1064 nm

---

pumping. The thermal effects in the vanadate laser confirmed the benefits of using diamond even at these power levels.

Finally, we investigated a different Raman laser design, with the pump not resonated but instead just double passed. Such lasers tend not to run on a single longitudinal mode. By inserting a frequency-doubling crystal and adjusting the doubled power, we could use this to stabilize the infrared output power to achieve SLM operation. We get stable first Stokes operation at 4.3 W with the aid of 1250 mW of frequency doubled conversion. We analyse the stabilizing mechanism of axial mode suppression due to the doubling process.

The presented experimental and theoretical work is a big step towards bringing our understanding of pump-resonant Raman lasers up to the level of other Raman designs. The model derived in this thesis provides a good reference to predict the laser performance, and to aid people to design lasers for optimum output. The methods to achieve SLM operation show the potential of narrow linewidth Raman lasers, and close the capability gap between Raman lasers and other wavelength shifting technologies.

# Contents

Acknowledgements .....	iii
Abstract .....	v
Contents .....	vii
Chapter 1    Introduction .....	1
1.1    Stimulated Raman scattering.....	1
1.2    Raman laser theory.....	5
1.2.1    Classical Raman theory.....	5
1.3    Building Raman lasers.....	11
1.3.1    Raman laser classification.....	11
1.3.2    Raman gain medium.....	14
1.3.3    Development of diamond Raman lasers.....	18
1.4    Narrowband Raman lasers .....	19
1.4.1    Single longitudinal mode operation .....	20
1.4.2    SLM operation of CW Raman lasers .....	22
1.5    Thesis outline.....	26
Chapter 2    Modelling of continuous wave resonantly pumped Raman lasers.....	28
2.1    Introduction .....	28
2.2    First Stokes model.....	29
2.2.1    Model derivation .....	29
2.2.2    Model analysis .....	33
2.3    Second Stokes model.....	38
2.3.1    Model derivation .....	38
2.3.2    Model analysis .....	41
2.4    The mode mismatch factor.....	46
2.5    Crystal length selection.....	47
2.6    Laser performance for optimum mirrors.....	48
2.7    The arbitrary order Stokes model.....	53
2.8    Conclusion .....	56
Chapter 3    Continuous wave resonantly pumped diamond Raman laser .....	57
3.1    The experimental design .....	57
3.1.1    Cavity design overview .....	57
3.1.2    Mirror design .....	60
3.1.3    Locking system design .....	64



3.1.4	Optical component selection .....	66
3.2	Setup installation .....	68
3.2.1	Note on the cavity installation .....	68
3.2.2	Cavity alignment .....	69
3.2.3	Stokes alignment.....	71
3.2.4	Locking alignment .....	74
3.3	Results and discussion .....	76
3.3.1	First Stokes generation.....	76
3.3.2	Second Stokes generation .....	79
3.3.3	Mirror optimization.....	84
3.3.4	PDH locking and HC locking .....	85
3.3.5	Locking asymmetry .....	86
3.4	Conclusion.....	88
Chapter 4	Continuous wave resonantly pumped vanadate Raman laser.....	89
4.1	Introduction .....	89
4.2	Experimental Setup.....	90
4.2.1	Design overview.....	90
4.2.2	Mirror design .....	91
4.2.3	Thermal lensing management .....	93
4.2.4	Cavity design .....	95
4.3	Result and discussion.....	96
4.3.1	Stokes Power I/O.....	96
4.3.2	Pump coupling issue .....	98
4.3.3	Spectrum.....	100
4.4	Diamond Raman laser using a 1064 nm pump .....	102
4.5	Optimization .....	104
4.6	Conclusion.....	105
Chapter 5	Single longitudinal mode external cavity diamond Raman laser.....	106
5.1	Introduction .....	106
5.2	Experimental setup.....	107
5.2.1	Setup design.....	107
5.2.2	Setup overview .....	112
5.3	Results and disscussion.....	114
5.3.1	Output power .....	114
5.3.2	Stokes beam quality .....	116
5.3.3	Spectrum analysis .....	118
5.3.4	Stability analysis dicussion .....	121
5.4	Conclusion.....	123
Chapter 6	Conclusion.....	124
6.1	Summary.....	124
6.2	Implications and future work.....	126
6.2.1	Raman laser model .....	126
6.2.2	SLM operation of Raman laser .....	127
6.2.3	Stabilization of Raman lasers .....	128

---

6.3	Closing words.....	128
	General effective area derivation .....	129
	List of Publications .....	131
	References .....	149

---



## 1

## Chapter 1. Introduction

### 1.1 Stimulated Raman scattering

Since the laser was first operated in 1960 [1], it has received considerable attention across a number of disciplines for its high intensity, high coherence, single wavelength and highly directional propagation. The main difference between lasers and other sources of light is high coherence. Spatial coherence allows lasers to be highly directional - highly collimated - which means lasers can be applied in applications like laser pointers or lidar [2]. The spatial coherence also allows lasers to be focused tightly, reaching high intensity and small spots enabling applications like laser machining and lithography [3,4]. Temporal coherence is associated with a narrow spectrum, which can be applied in fields like precise measurement or spectroscopy [5,6]. Lasers can operate as continuous wave (cw) or pulsed. Pulsed lasers can reach the highest peak powers, while cw lasers can achieve narrower output spectra.

The output wavelength of most laser materials is quite limited, with notable exceptions of media with naturally broad emissions like Ti:sapphire with a tuning range from 650 nm to 1000 nm [7] and Yb-doped laser materials with ranges from 970 nm to 1200 nm [8]. We can access more wavelengths from any laser source by using nonlinear effects, with methods splitting into second order nonlinear effects and third order nonlinear effects.

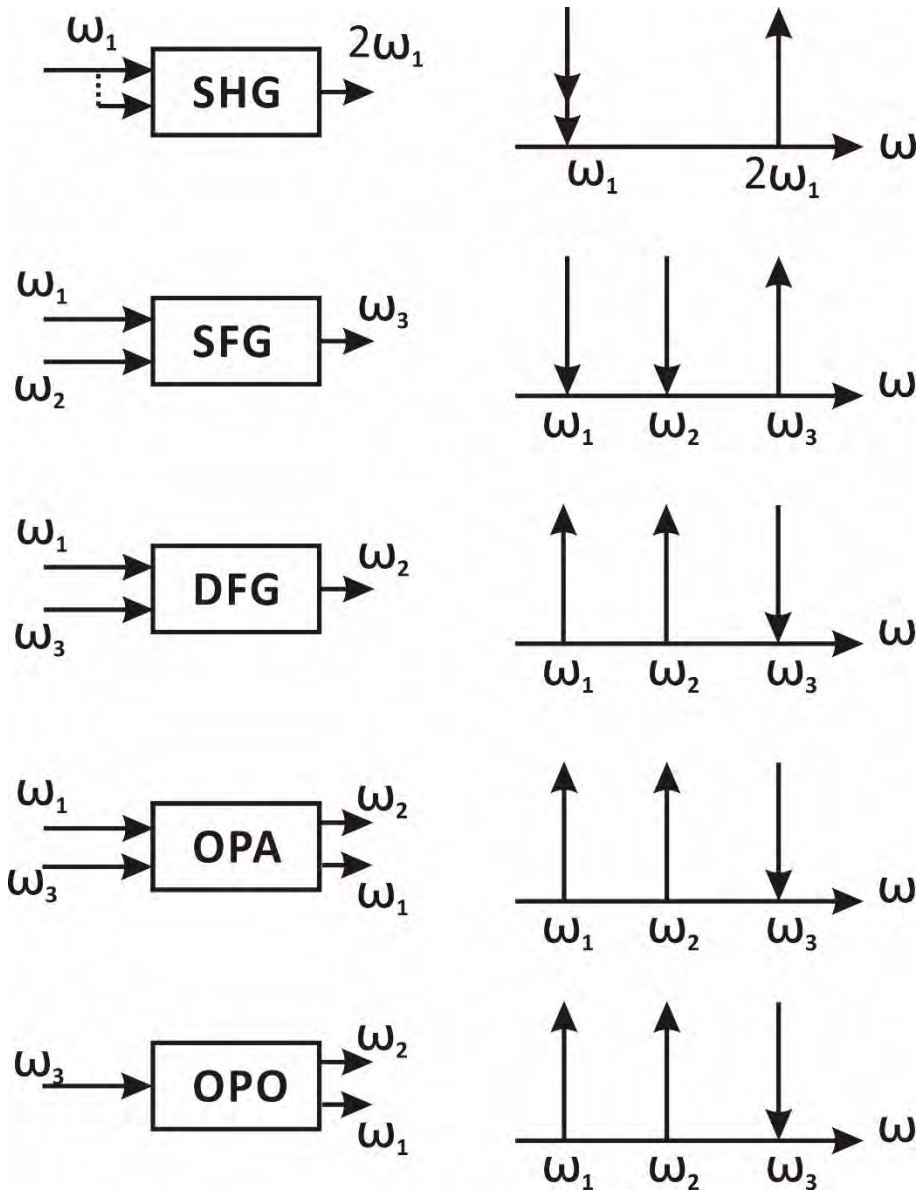


Figure 1-1 Second order nonlinear effects. In the right diagrams, up-arrows are created photons, down-arrows are depleted photons.

Figure 1-1 shows second order nonlinear processes. Second harmonic generation (SHG) is a second order nonlinear process that is based on the annihilation of two input photons with the same angular frequency  $\omega_1$  when a laser passes through the nonlinear medium, while simultaneously one photon at frequency  $2\omega_1$  is generated. Sum-frequency generation (SFG) is a similar process to SHG with different photons inputs at  $\omega_1$  and  $\omega_2$ , and the output photon is generated at the frequency of  $\omega_3 = \omega_1 + \omega_2$ . Difference-frequency generation (DFG) is a bit different as the desired output frequency is  $\omega_2 = \omega_3 - \omega_1$ . The selection

between SFG and DFG depends on the chosen phase matching conditions. The DFG process also amplifies the lower-frequency input field  $\omega_1$ , and if this is the desired outcome we call the process optical parametric amplification (OPA), where  $\omega_3$  is the pump source,  $\omega_1$  is the amplified signal beam, and the created  $\omega_2$  beam is called the idler beam.

If we put the nonlinear medium into a resonator to resonate the signal beam and idler beam, we call this an optical parametric oscillator (OPO). Note the only input beam is the pump field because the signal (and idler) can be generated by optical parametric scattering and amplified by the resonator. OPOs can be divided as single-resonant OPO and double-resonant OPO based on how many frequencies are resonated. With various pump wavelengths, OPOs can achieve continuous wavelength tuning, covering the ultra violet to infrared by continuously changing the phase-matching condition [9,10]. Thus, OPOs are the main commercial technology for a wide range of applications needing wavelength versatility.

Using third order nonlinearity, four-wave mixing (FWM) is another one of the effects that generates new wavelengths. As shown in Figure 1-2, the input fields and generated field meet the energy conservation  $\omega_4 = \omega_1 + \omega_2 + \omega_3$  and momentum conservation  $k_4 = k_1 + k_2 + k_3$ . A special case is when  $\omega_1 = \omega_2 = \omega_3$ , and the generated field is called the third harmonic. Another third order nonlinear effect is called stimulated Raman scattering (SRS). In 1962, E. J. Woodbury et al. first observed the stimulated Raman scattering in the nitrobenzene of the Q-spoiling Kerr shutter when they studied the Q-switched laser [11]. The SRS process can be viewed as a “resonant”  $\chi^{(3)}$  where two pump photons interact with two Stokes photons. In SRS process, the frequency difference between the pump and Stokes field is resonant with a material vibration (the phonon mode), and that material vibration converts pump energy into Stokes energy. For better understanding, this process can be viewed as a pump photon exciting the material to a virtual level and leaving the material in an excited state, as Figure 1-2 right shows. Momentum is automatically conserved in the process so there is no phase matching required, but power is transferred to the material as phonons are created.

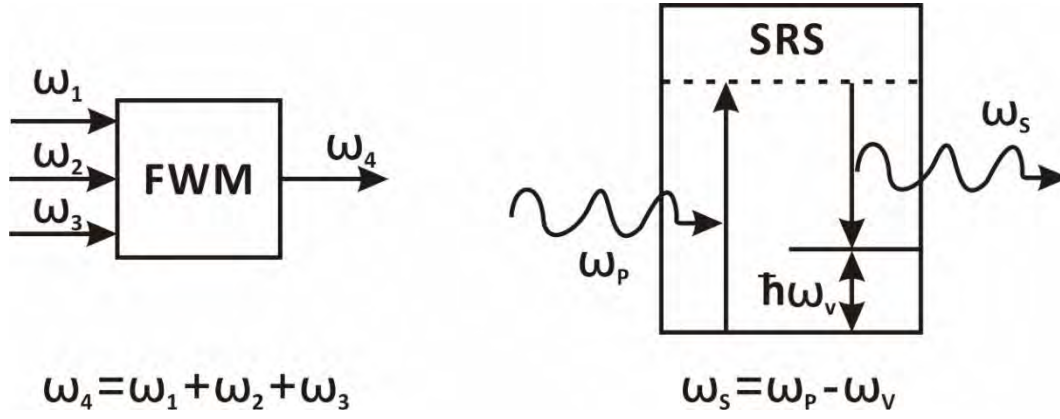


Figure 1-2 The FWM (left) and SRS (right) processing

SRS gain can be used to build lasers to shift the wavelength of existing laser sources. The output Stokes field wavelength is dependent on the combination of the input field wavelength and the Raman shift, which is a property of the Raman gain medium. One of the characteristics of the SRS is it can be cascaded, which means the wavelength output can be easily expanded by multiple cascaded Raman shifts. By choosing various Raman gain media that have different Raman shifts, and using different pump sources, we can access a wide range of different wavelengths.

Compared to the OPO process, phase-matching in SRS is automatically met by the flexible k-vector of the phonon vibration, which means the Raman process is automatically phase-matched [12]. Although we lose the ability to continuously adjust the output wavelength by tuning the phase match condition, this automatic phase matching can simplify the laser cavity setup and make lasers more robust, and easier to maintain.

The nature of the auto phased-matching of SRS can also help to improve the generated beam quality, improving on the beam quality of the incoming pump and avoiding problems caused by thermal dephasing. The spatial gain profile of Stokes field is a convolution of the pump and Stokes fields, and after multiple round trips in the resonator, the output Stokes can tend towards a TEM<sub>00</sub> shape even for lower beam quality pump lasers. This is called Raman beam clean-up [13,14].

## 1.2 Raman laser theory

We now review Raman laser theory, before further describing how Raman lasers are built.

### 1.2.1 Classical Raman theory

The classical Raman theory focuses on the macroscopic nonlinear interaction of waves, while the quantum description of the Raman interaction can provide details about the origin of spontaneous scattering and how it seeds the stimulated process. Here we only describe the classical Raman theory which is easier to understand; a quantum description of Raman scattering can be found from Ref. [12,15] by Penzkofer and Boyd respectively.

The classical Raman theory starts from the Maxwell's equations in the form as.

$$\begin{cases} \nabla \times \mathbf{E} = -\frac{\partial \mathbf{B}}{\partial t} \\ \nabla \times \mathbf{H} = \mathbf{J} + \frac{\partial \mathbf{D}}{\partial t}, \\ \nabla \cdot \mathbf{D} = \rho \\ \nabla \cdot \mathbf{B} = 0 \end{cases} \quad (1-1)$$

where the  $\mathbf{E}$  is electric field,  $\mathbf{H}$  is magnetic field,  $\rho$  is charge density,  $\mathbf{J}$  is current density,  $\mathbf{D}$  is electric displacement,  $\mathbf{B}$  is magnetic induction, and  $t$  is time. The magnetic induction  $\mathbf{B}$ , current density  $\mathbf{J}$  and electric displacement  $\mathbf{D}$  have the relationships as follows

$$\mathbf{D} = \epsilon_0 \mathbf{E} + \mathbf{P} = \epsilon \mathbf{E}, \quad (1-2)$$

$$\mathbf{B} = \mu_0 (\mathbf{H} + \mathbf{M}) = \mu \mathbf{H}, \quad (1-3)$$

$$\mathbf{J} = \sigma \mathbf{E}, \quad (1-4)$$

where  $\mathbf{P}$  is electric polarization of material while  $\mathbf{M}$  is magnetization of material, and for linear materials  $\epsilon = \epsilon_0 \epsilon_r$  is the permittivity,  $\mu = \mu_0 \mu_r$  is the permeability, the subscript 0 and  $r$  represent the free space and relative value in the material.  $\sigma$  is called conductivity, is the proportionality constant between  $\mathbf{J}$  and  $\mathbf{E}$ . The electric polarization  $\mathbf{P}$  can be described as

$$\mathbf{P} = \epsilon_0 (\epsilon_r - 1) \mathbf{E} = \epsilon_0 \chi^{(1)} \mathbf{E}, \quad (1-5)$$



where  $\chi^{(1)}$  is the linear electric susceptibility which measures the degree to which the material can be polarized.

In order to derive the Raman theory, here we add some assumptions, which are valid for propagation and Raman scattering in gases, and some liquids; for anisotropic crystals, the assumptions remain valid but with  $\epsilon$  and  $\chi$  as tensors. The assumptions include the dielectric is isotropic, homogeneous, source free and non-conducting. Isotropic means the dielectric can be fully rotational symmetrical; homogeneous is the dielectric has translational symmetrical; source free means the free charge density is zero; Non-conducting means  $\mathbf{J} = 0$ . In nonlinear media, the electric polarization  $\mathbf{P}$  can be written as the linear part and nonlinear part.

$$\mathbf{P} = \epsilon_0(\chi^{(1)}\mathbf{E} + \chi^{(2)}\mathbf{E}^2 + \chi^{(3)}\mathbf{E}^3 + \dots) = \mathbf{P}_L + \mathbf{P}_{NL}, \quad (1-6)$$

where  $\mathbf{P}_L = \epsilon_0\chi^{(1)}\mathbf{E}$ , and  $\chi^{(1)}$  describes the refractive index. The  $\chi^{(2)}, \chi^{(3)} \dots$  describe the second-order, third-order... nonlinear effects as the second, third nonlinear electric susceptibility. Note that the even-order nonlinear effects only happen in the media without inversion symmetry.

The next step is to derive the wave equation with nonlinear electric polarization included. We apply the curl operator cross to Eq. (1-1) ( $\nabla \times \text{Eq. (1-1)}$ ), to get

$$\nabla \times \nabla \times \mathbf{E} = -\nabla \times \frac{\partial \mathbf{B}}{\partial t} = -\frac{\partial}{\partial t}(\nabla \times \mu \mathbf{H}) = -\mu \frac{\partial}{\partial t}(\mathbf{J} + \frac{\partial \mathbf{D}}{\partial t}). \quad (1-7)$$

Substitute Eq. (1-2), Eq. (1-4), and note  $\mathbf{J} = 0$ . We can rewrite Eq. (1-7) as

$$\nabla \times \nabla \times \mathbf{E} = -\mu \frac{\partial^2 \mathbf{P}_{NL}}{\partial t^2} - \mu \epsilon \frac{\partial^2 \mathbf{E}}{\partial t^2}. \quad (1-8)$$

From the property of the curl operator, we can say

$$\nabla \times \nabla \times \mathbf{E} = -\nabla^2 \mathbf{E} + \nabla(\nabla \cdot \mathbf{E}), \quad (1-9)$$

where  $\nabla \cdot \mathbf{E} = 0$ . Therefore Eq. (1-8) can be rewritten as

$$-\nabla^2 \mathbf{E} = -\mu \frac{\partial^2 \mathbf{P}_{NL}}{\partial t^2} - \mu \epsilon \frac{\partial^2 \mathbf{E}}{\partial t^2}. \quad (1-10)$$

Note that the refractive index is defined as

$$n = \frac{c_0}{c} = \frac{c_0}{\sqrt{\epsilon\mu}}, \quad (1-11)$$

where the  $c_0$  is the speed of light in vacuum. Substituting Eq. (1-11) into Eq. (1-10), we can get the form as

$$\nabla^2 \mathbf{E} - \frac{n^2}{c_0^2} \frac{\partial^2 \mathbf{E}}{\partial t^2} = \frac{1}{\epsilon_0 c_0^2} \frac{\partial^2 \mathbf{P}_{NL}}{\partial t^2}. \quad (1-12)$$

This is a wave equation, with a nonlinear source term on the right-hand side. The next step is the derivation of the nonlinear electric polarization  $\mathbf{P}_{NL}$  [15], which can describe stimulated Raman scattering. Note that the following derivation is only in the scalar approximation for easier understanding.

When an optical field passes through the dielectric, a polarization proportional to the molecule dipole moment  $\mathbf{p}$  and the number of molecules  $N$  can be induced in the dielectric material as

$$\mathbf{p}(z, t) = \alpha \mathbf{E}(z, t), \quad (1-13)$$

in which  $\alpha$  is molecular polarizability. The polarization can be rewritten as

$$\mathbf{P} = N\alpha \mathbf{E}(z, t). \quad (1-14)$$

In the Placzek approximation [16],  $\alpha$  depends on the distance between atoms  $q(t)$  as follows rather than being constant.

$$\alpha(t) = \alpha_0 + \left( \frac{\partial \alpha}{\partial q} \right)_0 q(t). \quad (1-15)$$

This means that when the molecule is periodically oscillating (driven by the applied harmonic field) the polarizability is also periodically fluctuating. Therefore, in turn, the refractive index of the dielectric is modulated in time. The transmitted electromagnetic wave acquires frequency sidebands at the resonant frequency of the oscillator  $\pm\omega_r$ . This molecule oscillation can be described by the harmonic oscillator model shown below

$$\frac{d^2 q}{dt^2} + 2\gamma \frac{dq}{dt} + \omega_r^2 q = \frac{F(t)}{m}, \quad (1-16)$$

where  $\gamma$  is the damping constant,  $m$  is the reduced atom mass,  $F(t)$  is the driving force of oscillation.  $F(t)$  derives from the optical fields: the energy of the optical fields can be expressed as

$$W = \frac{\alpha E^2(z, t)}{2}, \quad (1-17)$$

and so the force can be written as

$$F(z, t) = \frac{dW}{dq} = \frac{1}{2} \left( \frac{d\alpha}{dq} \right)_0 \langle E^2(z, t) \rangle, \quad (1-18)$$

in which the angled brackets  $\langle \rangle$  means a time average over an optical period.

We define the pump laser frequency  $\omega_p$ , and a Stokes frequency  $\omega_s = \omega_p - \omega_r$ . The total electric field can be written as

$$E(z, t) = A_p \exp[i(k_p z - \omega_p t)] + A_s \exp[i(k_s z - \omega_s t)] + c. c, \quad (1-19)$$

so the Eq. (1-18) is

$$F(z, t) = \left( \frac{d\alpha}{dq} \right)_0 A_p A_s^* \exp[i(kz - \Omega t)] + c. c, \quad (1-20)$$

where  $k = k_p - k_s$ ,  $\Omega = \omega_p - \omega_s$ . For crystals, the counter-propagating pump and Stokes have the same end results, with a different  $k$  vector associated with the material excitation.

Substitute Eq. (1-20) into Eq. (1-16), we can solve:

$$q(\Omega) = \frac{\left( \frac{d\alpha}{dq} \right)_0 A_p A_s^*}{m(\omega_r^2 - \Omega^2 - 2i\Omega\gamma)}. \quad (1-21)$$

After the substitution of Eq. (1-15) and Eq. (1-20), Eq. (1-14) can be rewritten as

$$\mathbf{P}_{NL}(\mathbf{z}, t) = N \left( \frac{d\alpha}{dq} \right)_0 [q(\Omega) e^{i(kz - \Omega t)} + c. c] \times [A_p e^{i(k_p z - \omega_p t)} + A_s e^{i(k_s z - \omega_s t)}] + c. c. \quad (1-22)$$

Here we see the polarization includes frequency components at  $\omega_p$ ,  $\omega_s$ , and  $(\omega_p - \omega_s)$ ; for now we can extract the  $\omega_s$  components as

$$\mathbf{P}_{NL}(\omega_s) = N \left( \frac{d\alpha}{dq} \right)_0 q^*(\Omega) A_p e^{ik_s z} = 6\epsilon_0 \chi_R^{(3)}(-\omega_s; \omega_p, -\omega_p, \omega_s) |A_p|^2 A_s e^{ik_s z}. \quad (1-23)$$

In this equation we have written the polarization in the form of a third order nonlinearity, and we recognise  $\chi_R^{(3)}$  as the third order susceptibility applied in Raman theory, which takes the value [17]

$$\chi_R^{(3)}(-\omega_s; \omega_p, -\omega_p, \omega_s) = \frac{N \left( \frac{d\alpha}{dq} \right)_0^2 (\omega_r^2 - \Omega^2) - 2\Omega\gamma N \left( \frac{d\alpha}{dq} \right)_0}{6\epsilon_0 m [(\omega_r^2 - \Omega^2)^2 + 4\Omega^2\gamma^2]}. \quad (1-24)$$

Using this nonlinearity as the driving term, the wave equation Eq. (1-12) predicts the amplitudes of pump and Stokes field under the slowly varying amplitude approximation as

$$\frac{dA_S}{dz} = i \frac{3\omega_S}{n_S c_0} \chi_R^{(3)}(\omega_S) |A_P|^2 A_S, \quad (1-25)$$

$$\frac{dA_P}{dz} = i \frac{3\omega_P}{n_P c_0} \chi_R^{(3)}(\omega_P) |A_S|^2 A_P. \quad (1-26)$$

The intensity of pump and Stokes field can be expressed based on the equation  $I = \frac{|E|^2 c_0 n \epsilon_0}{2}$ .

For the pump field we get

$$\frac{dI_P}{dz} = \frac{c_0 n \epsilon_0}{2} \left( \frac{dA_P}{dz} A_P^* + \frac{dA_P^*}{dz} A_P \right). \quad (1-27)$$

Setting  $k_P = \frac{c_0 n_P \epsilon_0}{2}$ , and substituting in Eq. (1-25) and Eq. (1-26), the Eq. (1-27) can be rearranged as

$$\frac{dI_P}{dz} = k_P \left[ \frac{3\omega_P}{n_P c_0} \frac{I_P I_S}{k_P k_S} (i \chi_R^{(3)}(\omega_P) + i^* \chi_R^{(3)*}(\omega_P)) \right]. \quad (1-28)$$

As  $i^* = -i$ ,  $\chi_R^{(3)}(\omega_P) = \text{Re} \chi_R^{(3)}(\omega_P) + i \text{Im} \chi_R^{(3)}(\omega_P)$ ,  $\chi_R^{(3)*}(\omega_P) = \text{Re} \chi_R^{(3)}(\omega_P) - i \text{Im} \chi_R^{(3)}(\omega_P)$ , we can rearrange the Eq. (1-28)

$$\begin{aligned} \frac{dI_P}{dz} &= k_P \left[ \frac{3\omega_P}{n_P c_0} \frac{I_P I_S}{k_P k_S} \left( i \text{Re} \chi_R^{(3)}(\omega_P) - \text{Im} \chi_R^{(3)}(\omega_P) - i \text{Re} \chi_R^{(3)}(\omega_P) - \text{Im} \chi_R^{(3)}(\omega_P) \right) \right], \\ \frac{dI_P}{dz} &= - \frac{6\omega_P I_P I_S}{n_P n_S \epsilon_0 c_0^2} \text{Im} \chi_R^{(3)}(\omega_P). \end{aligned} \quad (1-29)$$

In the same way, for  $\frac{dI_S}{dz}$  we find it can be rewritten as

$$\frac{dI_S}{dz} = - \frac{6\omega_P I_P I_S}{n_P n_S \epsilon_0 c_0^2} \text{Im} \chi_R^{(3)}(\omega_S). \quad (1-30)$$

Since  $\text{Im} \chi_R^{(3)}(\omega_S)$  is negative,  $\text{Im} \chi_R^{(3)}(\omega_P)$  must be positive based on the result of Eq. (1-24); therefore  $\frac{dI_P}{dz}$  is negative, which predicts attenuation of the pump field. On the other hand,  $\frac{dI_S}{dz}$  is positive, predicting the Stokes component increases during Raman process.

The classical theory thus explains the amplifying process of the Stokes field: The pump beam is incident into the Raman medium, where the spontaneous Stokes field is generated,

with phase-matching conditions auto matched; the weak spontaneous Stokes field and strong pump field can generate a beat frequency at the oscillation frequency of the Raman gain medium; that drives the molecules' oscillation to force the polarization  $P_{NL}$ , and as a result, the pump field is weakened while the Stokes field gets stronger. The stronger Stokes field enhances the beat frequency oscillation amplitude, and the positive feedback loop creates exponential Stokes gain.

Adding a loss coefficient for pump and Stokes fields  $\alpha_{P,S}$ , and defining a Raman gain coefficient  $g_{P,S}$ , we can write

$$\begin{cases} \frac{\partial I_P}{\partial z} = -g_P I_P I_S - \alpha_P I_P \\ \frac{\partial I_S}{\partial z} = g_S I_P I_S - \alpha_S I_S \end{cases} \quad (1-31)$$

The Raman gain coefficient is can be read off above as [12,15] as

$$g_S = N \left( \frac{\partial \alpha}{\partial q} \right)_0^2 \frac{4\pi\omega_S}{n_S n_P c_0^2 m \omega_r \Gamma_r} = N \frac{\partial \sigma}{\partial \Omega} \frac{8\pi c_0^2}{n_S^2 \hbar \omega_S^3 \Gamma_r}, \quad (1-32)$$

where  $\frac{\partial \sigma}{\partial \Omega}$  describes the integrated scattering cross-section of pump and Stokes,  $\Gamma_r$  is the Raman linewidth. The Raman gain is also related to the molecule density  $N$ , reduced mass  $m$ , and deformation potential  $\frac{\partial \alpha}{\partial q}$ , which are related to material properties. We can add the simplification  $g_P = g_S \omega_S / \omega_P$ , which is valid for most Raman materials.

While these equations predict exponential Stokes growth for fixed pump power, and exponential pump depletion for fixed Stokes power, their solution is more complex when the Stokes and pump fields are both changing. We model various Raman laser designs by making appropriate assumptions to simplify their solution. For the cw external cavity laser, the analytical model was derived by Ondrej Kitzler et al. [18], while the model for pulsed external cavity Raman laser was done by Shuanghong Ding et al. [19]. Analytical models for intracavity lasers were developed by David Spence et al. and Shuanghong Ding et al. [20,21].

## 1.3 Building Raman lasers

We now review how Raman lasers are built, and the course their development has taken. We then review the lasers most closely related to the work in this thesis, with a focus on narrow-band CW lasers.

### 1.3.1 Raman laser classification

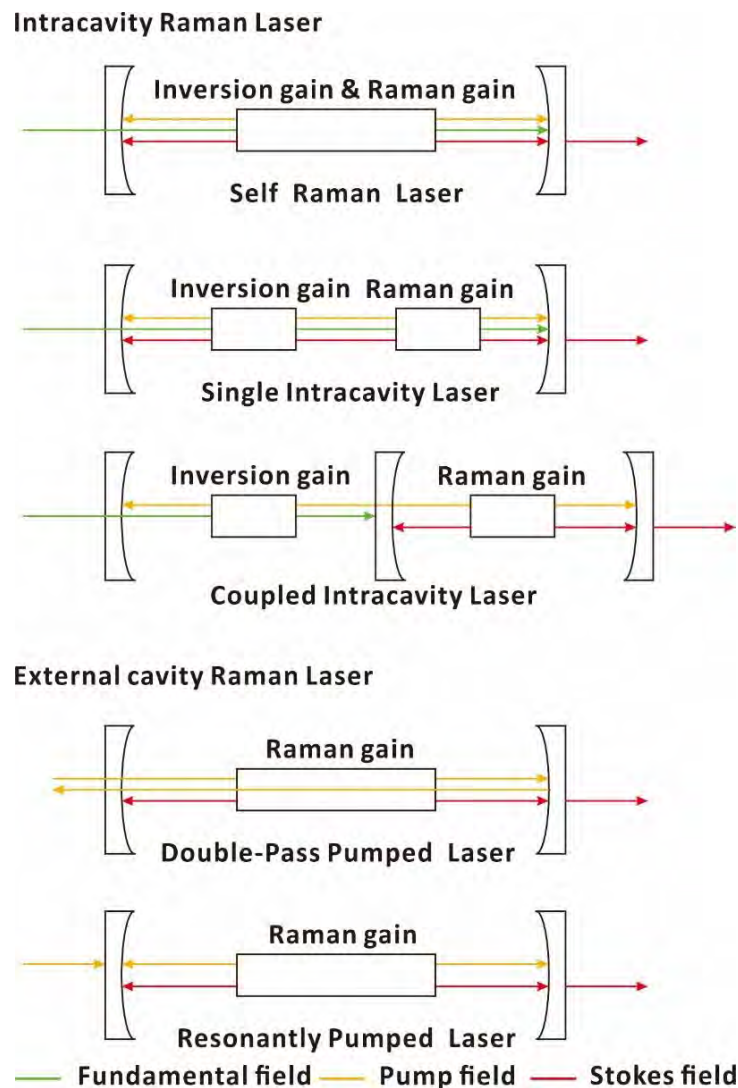


Figure 1-3 The different Raman laser configurations

Figure 1-3 shows the cavity setups of the different kinds of Raman lasers. Note that here we only discuss them in the cw and quasi-cw operation regime. For intracavity lasers, the

‘fundamental beam’ is the pump source for the inversion laser medium, which generates the ‘pump beam’ that drives the SRS and generates the Stokes beam. Due to the high intensity required to get reasonable Raman gain, intracavity Raman lasers are designed to reduce the threshold for the pump field by doing the SRS conversion inside the cavity of a conventional laser. ‘Self-Raman’ lasers from the most compact intracavity setup [22,23]. A single crystal can generate the pump beam and SRS together, which means the components in the cavity can be minimised, and the performance, maintenance, and stability can be excellent. However, as the same crystal must be the gain medium and do the Raman shifting, it limits the selection of the gain medium to those that also have high Raman gain. Besides, the heat deposition in the single crystal is higher than other setups as heat results from the quantum defect of both the inversion and the SRS processes. As a result, the maximum power is often limited by thermal effects. Self-Raman lasers based on infrared laser materials can achieve visible output by using intracavity SHG/SFG conversion [24,25].

In order to break through the limit of the gain medium selection, the ‘single intracavity laser’ can be designed by assigning the pump field generation and Stokes field generation to different gain media [26–28]. The separate selection of the Raman medium and the pump generation medium also makes the single intra cavity laser more flexible to access different wavelengths. In addition, the thermal load is divided between the two media, which gives more flexibility in design but still results in thermal effects that are complex and the cavity design should consider the thermal management (for example, thermal lensing) carefully.

The ‘coupled intracavity laser’ is often a more efficient design [29]. Compared to the other intracavity lasers we discussed above, the coupled intracavity laser adds a mirror in the cavity to isolate the Stokes field to a subsection of the cavity. The AR coating of the gain medium can be simpler compared to the other intracavity setups, and we can control the pump field separately. For example, the linewidth of pump can be controlled separately by inserting an etalon in that field only. The flexibility of the coupled intracavity laser is at the cost of adding a mirror into the cavity, therefore, the total passive loss for the pump field can be higher than in other intracavity configurations, but on the other hand losses can be lower for the Stokes field that now does not need to propagate through the laser crystal [30,31].

Therefore, intracavity Raman lasers have the benefit of low threshold and compact setup. Another advantage is that intracavity lasers can use various pump sources, like flash-lamps or electricity pump for diodes. However, as in the intra cavity Raman lasers the pump field with the Stokes field are generated at the same time, handling of thermal effect is more difficult. It also makes it harder to control the beam quality and spectrum of the laser as the complex processes are all happening together in the same cavity. Therefore, the maximum output power of intracavity laser is usually not above 5 W. Besides, intracavity Raman lasers are difficult to stabilize to operate on a single-longitudinal mode, which also limits their application.

For the external cavity laser design, the pump generation part is totally independent from the Raman shifting part. This provides more flexibility for pump source selection, and means that the beam quality and spectral control of the pump laser are separately optimized first, independent of the Raman laser. We can directly choose commercial pump lasers, and design the Raman laser setup just for the SRS generation part knowing that this cannot affect the pump source properties. However, now when we are not Raman shifting inside the pump laser cavity, the pump intensity is much lower, and the threshold of the external cavity laser is much higher than the intracavity setup. That means that methods to decrease the SRS threshold play a dominant role in external cavity Raman laser design: Double pass pumping setups (see the Figure 1-3), very tight focus spots, minimized passive loss, and very low Stokes output coupling are required to reduce the Raman threshold. Even so, most external cavity lasers are designed for pulsed output. The first cw Raman output using an external cavity was reported by A. S. Grabtchikov et al. in 2004 [32]. He demonstrated an external cavity Raman laser with a barium nitrate crystal as the Raman medium. The Stokes output was only 164 mW with 3.3% conversion efficiency with a threshold of 2.5 W. The combination of the poor thermal performance and low gain (compared to inversion lasers) limited the performance. The gain coefficient of  $\text{Ba}(\text{NO}_3)_2$  is actually really high for a Raman crystal, comparable to diamond. But the gain is low due to low intensity of the pump, as in all cw Raman systems. The performance of the gain medium has limited the usage of the external cavity until the advent of high quality CVD diamond. The diamond Raman laser,



which brings new vitality to the external cavity Raman laser, will be discussed in the next part.

One way to decrease the Raman threshold is the ‘pump-resonant cavity’ configuration. This can significantly decrease the Raman threshold by coupling the pump field resonantly to the separate Raman cavity. This cavity-enhances the pump in a similar way to the intracavity setup, but to couple the pump with the external cavity requires a cavity locking system to lock the cavity length. This makes a new demand on the linewidth stability of the pump source. Resonantly pumped lasers are the subject of this thesis.

### 1.3.2 Raman gain medium

In this thesis we focus on crystalline Raman media. While the first Raman laser used a liquid Raman gain medium [11], since then liquid Raman gain media are quite rare [33,34], due to intrinsic disadvantages of suitable liquids such as instability, toxicity, low Raman gain and poor thermal properties.

The gain coefficient of gas Raman media also tends to be small compared to that of crystals, however, there are some gas media like  $H_2$  and  $D_2$  that have quite excellent performance for narrow emission linewidths [35–37]. Another application of a Raman gas medium is to fill the gas into the core of hollow fibers to make a Raman laser [38,39].

One special gain format to be acknowledged in the Raman laser field is the fiber-based gain media [40,41]. Fiber lasers can significantly reduce the threshold by extending the gain medium length under the same pump intensity, and the fiber design can effectively control the thermal effects inside the fiber. Therefore, the fiber Raman laser makes high power Stokes output relatively easy to achieve [42]. Besides, the fiber can make the setup robust and easy to design. The limitation of the fiber laser is its gain medium; only a few suitable doped glasses can be drawn into a fiber. For high power lasers, the linewidth of the Stokes output in the fiber laser can be difficult to make very narrow, because in a long fiber stimulated Brillouin scattering (SBS) can occur. Pump and Stokes laser fields need to be

broadband to suppress the SBS effect. Such broadband Stokes output makes the fiber Raman laser less applicable to some fields.

Table 1-1 Raman crystal parameters and the thermal performance

	LiIO <sub>3</sub> [31,43, 44]	CaWO <sub>4</sub> [45]	Ba(NO <sub>3</sub> ) <sub>2</sub> [46,47]	KGd(WO <sub>4</sub> ) <sub>2</sub> (KGW) [48]	YVO <sub>4</sub> [49,50]	BaWO <sub>4</sub> [51–53]	Diamond [54]
Raman shift (cm <sup>-1</sup> )	770, 822	908	1047	768, 901	890, 814	926	1332.3
Raman linewidth (cm <sup>-1</sup> )	5	4.8	0.4	7.8, 5.9	2.6	1.6	1.5
Raman Gain @1064nm (cm/GW)	4.8	3	11	4.4, 3.5	>4.5	8.5	10-12
Damage threshold (GW/cm <sup>2</sup> )	~0.1	~0.5	~0.4	~10	~1	-	~8@1064 nm
Transmission Range (μm)	0.31-4	0.2-5.3	0.35-1.8	0.34-5.5	0.4-5	0.26-5	>0.23
Thermal conductivity K <sub>C</sub> @25 °C (Wm <sup>-1</sup> K <sup>-1</sup> )	1.27, 0.65	16	1.17	2.5-3.4	5.2	3	2000
Thermo-optic coefficient dn/dt (K <sup>-1</sup> ×10 <sup>-6</sup> )	-85, -69	-7.1, -10.2	-20	-9.8	3	<9	15
Thermal expansion α (mK <sup>-1</sup> ×10 <sup>-6</sup> )	48,28	6.35, 12.38	13	1.6-8.5	4.43	6	1.1

Compared to the media above, crystalline media play a significant role as a Raman gain material due to high Raman gain, compact design and flexibility. The common Raman crystals and their Raman performance and thermal performance are listed in the Table 1-1. Among these specifications, Raman gain decides the Stokes output performance, and the Raman shift determines the wavelength that may be generated. A large shift is particularly useful if the pump wavelength is relatively short, like 532 nm. For example, a diamond

Raman laser can directly extend the 532 nm wavelength pump to 572 nm, while for other medium, the Raman shift is too short and so the Stokes wavelength is too close to the pump wavelength, which increases the difficulty in the mirror design. Therefore, for a medium with a shorter Raman shift, researchers often prefer to generate visible wavelengths by using longer wavelength pumping and SHG, at the price of lower efficiency and setup complexity. The thermal conductivity affects the thermal gradients established in the crystal. The thermo-optic coefficient converts those gradients into refractive index profiles that will influence the thermal lensing, which is often the main problem causing degradation of the output performance. Thermal expansion, along with refractive index change, can change the optical length of the crystal and change the size of the resonator indirectly. Thus, the selection of the Raman crystal is crucial for the Raman laser performance.

High quality single crystal CVD diamond has been available for about the last ten to fifteen years and has had a large impact on crystalline Raman laser design [54,55]. Kaminskii et al. first reported pulsed SRS output using the synthetic diamond in 2004 [56], which marked the beginning of a new avenue for Raman laser design. Based on the data shown in Table 1-1, we see that diamond provides excellent specifications in its Raman shift, Raman gain, and thermal performance. The Raman gain of diamond is amongst the highest in common Raman crystals, due to its closely packed lattice, the relatively light atoms, and the high deformation potential  $d\alpha/dq$ . Similar to most crystals, the gain coefficient has an inverse correlation to the wavelength, such that  $g_1\lambda_1 \approx g_2\lambda_2$ , which means the Raman gain coefficient is higher at the visible wavelength ranges than in the infrared.

The outstanding Raman gain and thermal performance of diamond makes the prospects of cw external cavity Raman lasers brighter, as diamond compensates the problems of the external cavity Raman laser of high threshold and associated thermal issues. The amazing thermal conductivity of diamond, which is about 1000 times higher than other Raman crystals, means thermal issues disappear at ‘normal’ powers; the restriction of the pump power range is relaxed, which makes high-power Raman lasers possible. Another advantage of diamond is its transmission range, as Figure 1-4 shows: diamond can be applied from UV

to the far-infrared regime with the aid of AR coating. Note that there is an absorption feature from 2.6 to 6.2  $\mu\text{m}$ .

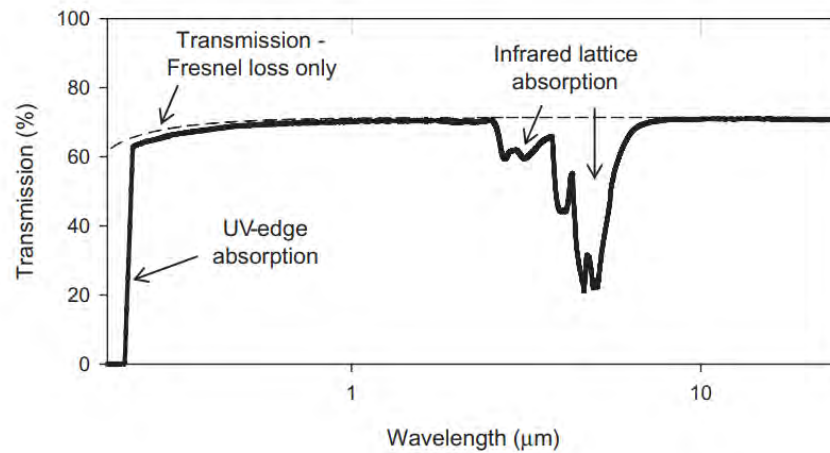


Figure 1-4 Transmission spectrum for a type IIa diamond of 1 mm thickness [54]

Based on the discussion above, diamond is an outstanding Raman material. However, diamond still has its disadvantages. Apart from the high cost of the diamond synthesis, diamond is subject to impurities and structural defects due to the less-developed synthesis technology [55]. The main influence is significant absorption loss and the high birefringence due to defects in the diamond lattice caused by nitrogen atoms during CVD growth. What's more, the uniformity of the birefringence is still hard to control. That restricts the diamond performance as the high birefringence area in the diamond will cause higher loss. Diamond has its unique Bravais lattice, it can be viewed as two interpenetrating face centered cubic lattices, which brings diamond's outstanding performance. However, this structure is hard to dope, and high concentrations of doped atoms will damage the diamond structure and degrade its optical performance. It is also hard to machine the diamond, which makes diamond hard to shape, for example to be applied as a waveguide. Even though improvements in diamond growth are continually reducing loss and birefringence, the progress has been relatively slow. The state-of-the-art technology still cannot guarantee the consistency of diamond batches, and this can make laser performance sensitive to the exact crystal used.

### 1.3.3 Development of diamond Raman lasers

The majority of the lasers in this thesis are based around diamond. The first diamond Raman laser (DRL) was demonstrated by Kaminskii et al. [56] with about 45% energy conversion efficiency from pump to Stokes field. With the improvements of diamond quality, the DRL became dominant as the medium of the external cavity Raman laser.

In the pulsed regime, M. Jelinek, Jr et al. reported an external cavity Raman laser with 47  $\mu\text{J}$  in a 6 ns pulse at 1.63  $\mu\text{m}$  in 2011 [57]. In the next year, A. McKay et al. increased the Stokes output to 35 W average power with 22 ns pulses and 38% conversion efficiency at 1485 nm [58]. The same group also reported 14.5 W of second Stokes lasing at 1485 nm with 22 ns pulses in 2013 [59]. Synchronous pumping of external cavities using mode locked pump lasers gave access to shorter pulse durations: A. M. Warrier et al observed 6 ps pulses for second Stokes lasing at 1485 nm with 59% overall conversion efficiency [60]; sub-100 fs pulses were generated by M. Murtagh et al. at 895 nm output with 33% slope efficiency [61]. Extending wavelengths to the ultraviolet, by pumping with the 4<sup>th</sup> harmonic of the 1064 nm pump, E. Granados et al. accessed an ultraviolet lasing of a picosecond diamond Raman laser. [62]. Alternatively intracavity SHG of the stokes field inside the external cavity is also a good way to reach shorter wavelengths: 620 nm sub-50 ps pulses from the SHG of the 1240 nm Stokes field was reported by J. Nikkinen et al [63] and 597 nm from the SHG of 1419 nm second Stokes under 1030 nm 12 ns pumping by V.P. Pashinin et al. [64].

Researchers also pushed performance in other directions, such as: wavelength tunable output [65,66]; brightness enhanced output [67–70]; high power pulsed DRL [71,72]; compact monolithic designs DRLs [73,74]; and multiple wavelengths for biology imaging [75]. While Raman lasers can result in brightness enhancement of high M squared pump beams, they can also be pumped by independent incoherent pump lasers, leading to the concept of Raman beam combination: using this approach A. McKay et al. achieved 6.7 kW of peak power at 1240 nm using three incoherent pump beams [76].

Lasers designed for continuous wave (cw) output are harder to get to threshold because of the lower pump intensity compared to a pulsed pump. The first cw DRL was reported by

O. Kitzler et al in 2012. They demonstrated 10.1 W Stokes cw operation with 49.7% slope efficiency at 1240 nm [77]. Since then, the maximum output power was continuously improved: R. J. Williams et al. in 2014 reported over 100 W quasi cw DRL output [78]; In 2015 the group demonstrated 145 W cw output and 381 W quasi cw output using a Yb-doped fiber pump laser [79]; In 2017 they demonstrated a second Stokes laser at 114 W cw output at 1.49  $\mu\text{m}$  [80]; in 2018, Z. Bai, R. J. Williams reported a brightness enhanced quasi-cw DRL with maximum second Stokes output of 302 W [70]. The latest update was by S. Antipov, R. J. Williams et al., who in 2019 and 2020 reported a 1.2 kW quasi cw DRL at 1240 nm, with the analysis of an emerging thermal lens at this power level [81,82]. Other groups also built high power lasers, such as M. Heinzig et al who reported a 136 W quasi cw output at 1178 nm with nearly diffraction-limited beam quality [83].

Other studies focused on the wavelength tunable output. In 2013, D. C. Parrotta et al. achieved a tunable DRL from 1209 to 1256 nm with a maximum output over 4 W, by using a diode-pumped InGaAs-based semi-conductor disk laser [84]. This research group also reported a cw DRL with over 40 nm tuning range in 2017 [85].

## 1.4 Narrowband Raman lasers

There are many current and future potential uses for Raman lasers with narrow linewidth. For example, light detection and ranging (LIDAR) can make range-resolved measurements of atmospheric properties or gas detection. It often requires stable narrow linewidth laser (of order 100 kHz) for accurate concentration measurements. Applications often need specific wavelengths, which need the aid of the SRS process to be achieved [86,87].

For laser guide stars as an example, the requirements on the laser are relatively strict; needing high power (the higher the better), narrow linewidth (8 MHz) and specified wavelength (589 nm), in order to match the Doppler broadened width of the sodium D<sub>2</sub> line and have more photons return from the sodium beacon [88]. The diamond-based Raman laser can meet all these requirements [89] and has excellent possibilities for further power scaling.

In the atomic-scale world, Raman lasers can be advantageous they can generate unusual wavelengths with narrow linewidth. For example, atom cooling experiments needs narrow linewidth lasers with specific wavelengths to fit a particular energy level of studied atoms [90,91]. In addition, Raman lasers also show potential as an optical tweezer source [92,93].

### 1.4.1 Single longitudinal mode operation

Laser cavities have longitudinal modes separated by the frequency difference  $\Delta\nu_q = c/p$ , where  $c$  is the speed of light, and  $p$  is the round-trip length of the cavity. As shown in Figure 1-5, most laser gain media have a gain bandwidth considerably larger than this spacing, and there are many longitudinal modes that can operate. Crystalline Raman lasers also have gain bandwidths that generally cover many longitudinal modes. For instance, the Raman linewidth of diamond is 22.5 GHz [94], while the mode spacing of a typical Raman ring cavity is about 500 MHz, and 1 GHz for a linear external Raman cavity. That means the cavity generally has dozens of longitudinal modes within the gain bandwidth. If a laser operates on only one longitudinal mode, we call this a single longitudinal mode laser, or a single-frequency laser. It emits quasi-monochromatic radiation with the narrow linewidth of the mode. Usually, SLM lasers operate with low intensity noise due to elimination of mode beating. Spatial hole burning is an effect in inversion lasers that often prevents SLM operation. Figure 1-6a, shows a cavity with length of  $L$  filled with a gain medium, and there is only one longitudinal mode  $q_1$  lasing. The mode forms a standing wave oscillating in the cavity with nodes and antinodes. Based on the mechanism of the inversion laser, at the antinodes, the population inversion is depleted, while there is undepleted inversion at wave nodes, as Figure 1-6b shows. The imbalance of the population inversion in the cavity is called spatial hole burning, and the population inversion is not exhausted. This allows another longitudinal mode  $q_2$  to lase at a different frequency to  $q_1$ , using the remaining population inversion to oscillate in this cavity, as Figure 1-6c shows. Therefore, it is difficult for an inversion laser to achieve the SLM operation.

Raman lasers have a different gain mechanism to the inversion lasers. Raman laser directly convert the pump beam to Stokes output. There is no local storage of pump energy

and so there can be no concept of locally undepleted areas of gain, which avoids the spatial hole burning effect. Therefore, Raman lasers might be a good choice for trying to achieve narrow linewidth operation. By combining the SLM operation and a tunable pump source (like the Ti:Sapphire laser), Raman lasers can in principle reach tunable SLM operation over a wide spectral range.

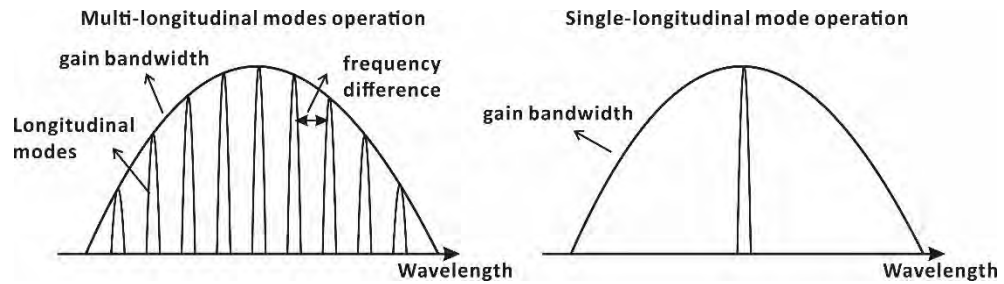


Figure 1-5 multi-longitudinal modes operation and single-longitudinal mode operation of a laser

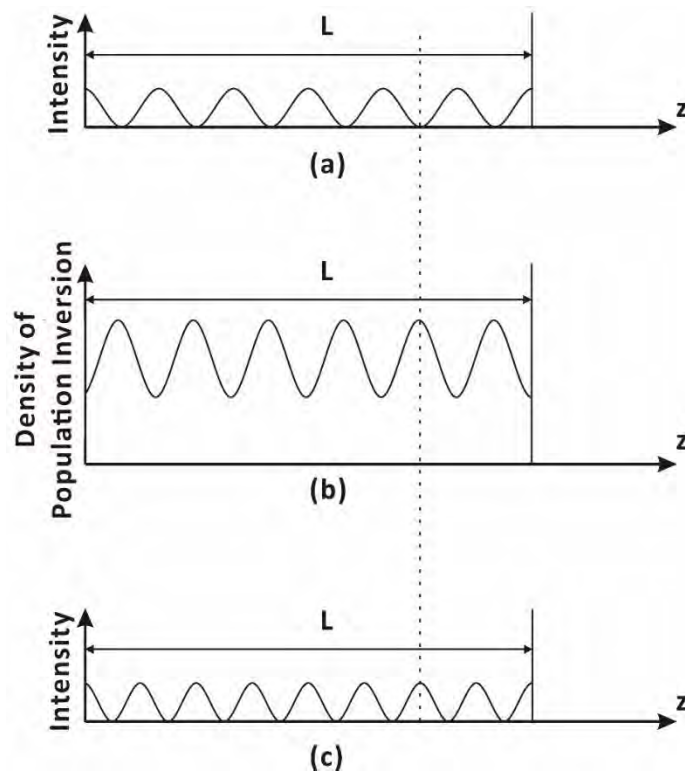


Figure 1-6 The intensity distribution of longitudinal mode  $q_1$  (a) and  $q_2$  (c) in the cavity. (b) shows the density of the population inversion in the cavity when only  $q_1$  mode exists.



### 1.4.2 SLM operation of CW Raman lasers

With cw DRLs becoming more mature, more attention started to be paid to their spectrum, and achieving single-longitudinal-mode (SLM) Raman lasing.

In 2016 Oliver Lux et al. achieved SLM Raman operation in a linear cavity and investigated its spectral behavior [95]. Using a tunable pump source from 1062.8 to 1065.6 nm with high stability of 40 MHz, this laser reached a stable SLM first Stokes (from 1238.1 to 1241.9 nm), up to 4 W with 80 MHz frequency stability. He used a piezo to control the cavity length (shown in Figure 1-7). The piezo was tuned by hand to get the highest Stokes output, but there was no active cavity stabilization. Even though this laser was not designed to enhance the pump field in the cavity, even the very small 2.8% reflectivity of the input mirror for the pump did create a significant change in performance depending on whether the pump was resonant. Stabilization of the surroundings like crystal temperature, vibration, noise, were also important for the laser operation. With the absence of spatial hole burning effect in the Raman laser, it could achieve decent SLM operation for short periods. However, given the high requirement of the surrounding stabilization, it still really needs active stabilization components to achieve SLM laser operation in more scenarios.

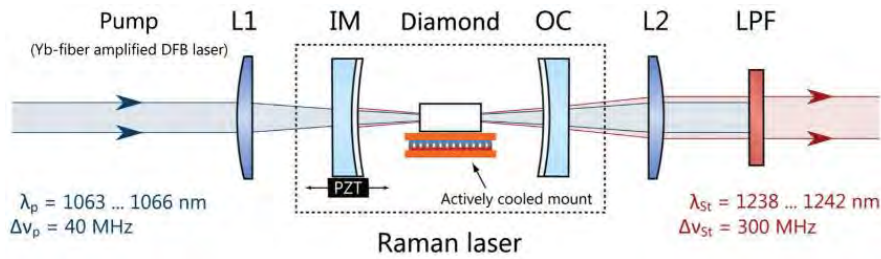


Figure 1-7 Schematic of the diamond Raman oscillator. IM: input mirror, OC: output coupler, LPF: long-pass filter, L1, L2: lenses [95].

In another work [86] (shown in Figure 1-8), by using the same pump source he achieved 1486 nm stable second Stokes output at 0.5 W with 40 MHz frequency stability. In this laser setup, besides the passive stabilization of temperature control and cavity length, he added a volume Bragg grating as an output coupler to do the mode selection (the second Stokes

output can only achieve SLM operation at 0.1 W without the Bragg grating). The VBG here acts as a Fabry-Perot resonator with small free spectral range (FSR), therefore providing a frequency selective feedback to the laser, encouraging SLM output.

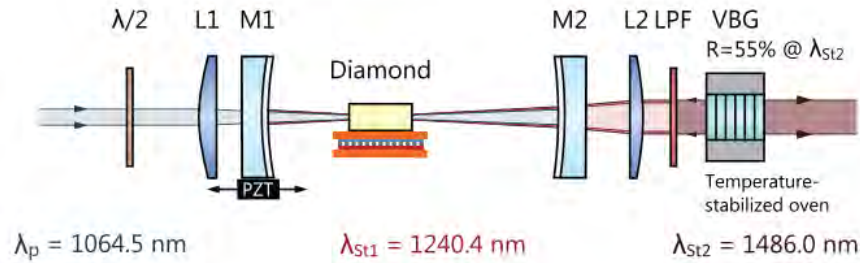


Figure 1-8 Laser setup of Oliver's Raman laser with stable SLM second Stokes output [86].

In Soumya's work [96], a Raman laser was built using a 1064 nm pump source with linewidth of 5 MHz (see Figure 1-9 ) and achieved 4.5 W SLM Stokes output with frequency fluctuations about 125 MHz, and 7.2 W maximum SLM Stokes output but just stable for a few seconds. In this work, the cavity was still not designed to significantly resonate the pump, but the small resonant effect due to the 1% reflectivity of the input mirror for the pump was used to stabilize the cavity length. This piezo control was active locking. This work used a version of Hänsch-Couillaud (HC) locking [97] to lock the cavity length to the weak resonance with the pump laser.

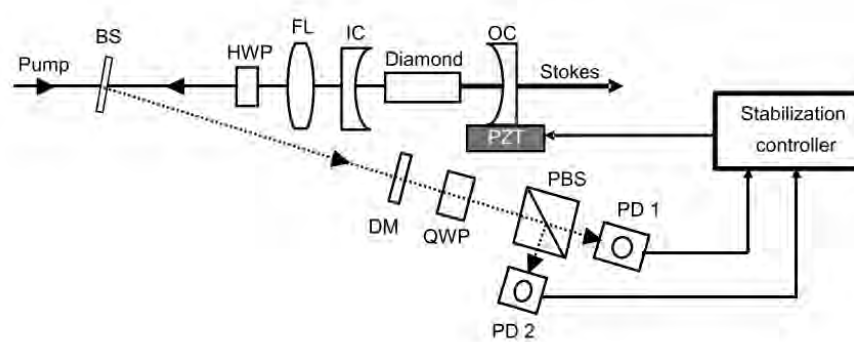


Figure 1-9 Experimental arrangement of a cavity-locked DRL; BS - beam sampler, HWP - half-wave plate, FL - focusing lens, IC - input coupler, OC - output coupler, PZT - piezoelectric translation stage, DM - dichroic mirror, QWP - quarter-wave plate, PBS - polarizing beam splitter, PD1 and PD2- photodetectors [96].

It's clear that cavity length stabilization is key to SLM performance. Given this need, it is appropriate to also design the laser for substantial pump resonance, taking the laser design from the external cavity Raman laser to a pump enhanced Raman laser. A pump resonant diamond laser was reported by Ondrej Kitzler in 2015 [98], pumped by a 5 W pump input at 790 nm with linewidth of less than 50 kHz. He achieved about 1 W SLM Stokes output at 883 nm. The layout is shown in Figure 1-10. The piezo here was used for cavity locking to cavity-enhanced the pump and generate stable Stokes output, using HC locking. It was found that the Stokes field in the ring cavity naturally operated in both directions, which is expected since the forward and backward SRS process in the crystal have the same gain. These competing two directions makes their output fluctuate on timescales of seconds. Even without spatial hole burning effect, this competition seems to prevent the SLM operation. To achieve SLM output, he broke the symmetry of the forward and backward oscillating modes inside the cavity: By retro-reflecting the Stokes output from one direction back into the Stokes field counter-propagating the pump, the counter-propagation of pump and Stokes fields inside the cavity was built up. This allowed up to 96% of the Stokes power to be in the backward field and stable SLM operation was achieved. The mechanism of the counter-propagating laser fields to achieve SLM output still needs further investigation. By building on Kitzler's work, we built a ring cavity and achieved SLM operation of a second Stokes laser, which is described in chapter 3.

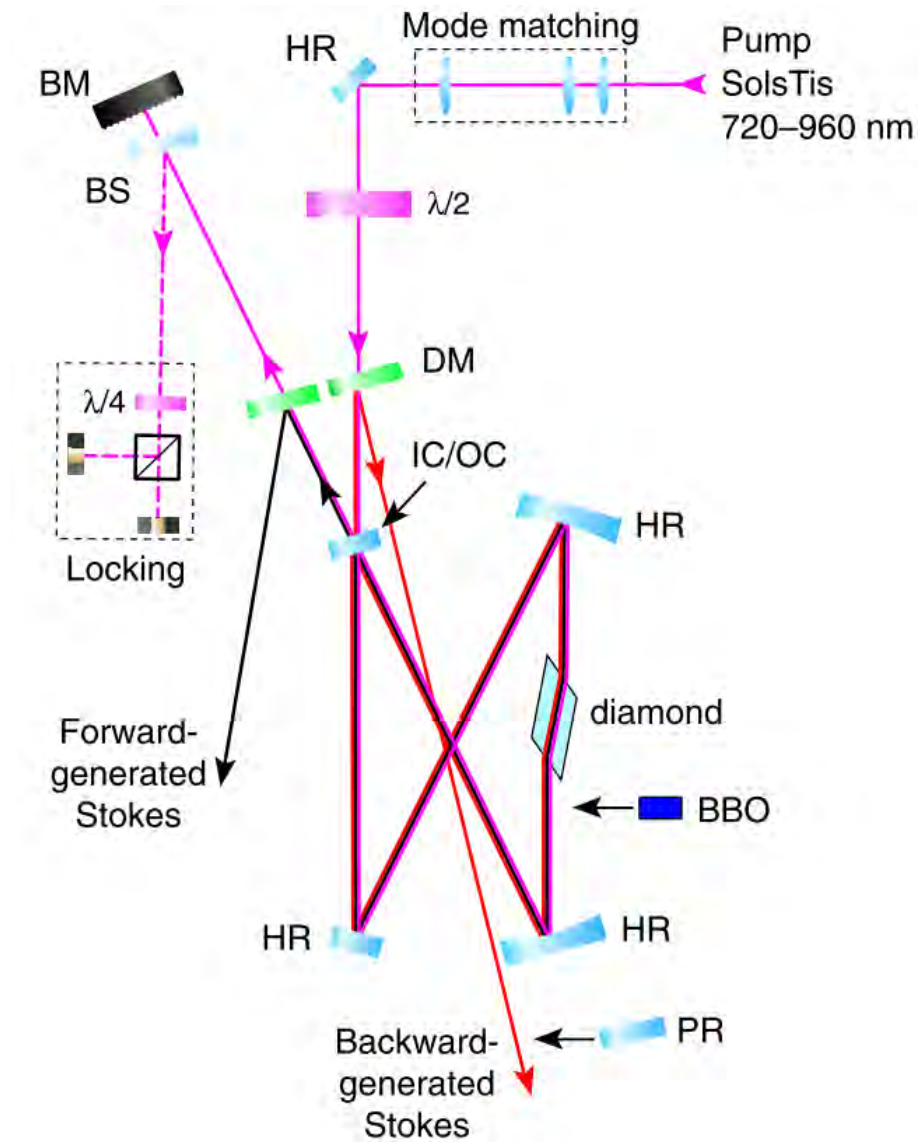


Figure 1-10 Schematic layout of the experimental setup. HR, high reflector; PR, partial reflector; IC/OC, input/output coupler, 1% transmission at 720 – 960 nm; DM, dichroic mirror, HR at Stokes, HT at pump; BS, uncoated beam sampler; BM, beam dump;  $\lambda/2$ , half-wave plate;  $\lambda/4$ , quarter-wave plate [98].

A final SLM Raman laser to review is Xuezhong Yang's work [99]. He used a multi longitudinal mode 1064 nm Nd:YAG pump laser with the power of 321 W and linewidth 3.3 GHz, to generates SLM power of 38 W at 620 nm and 11.8 W at 1240 nm. The setup is shown in Figure 1-11.

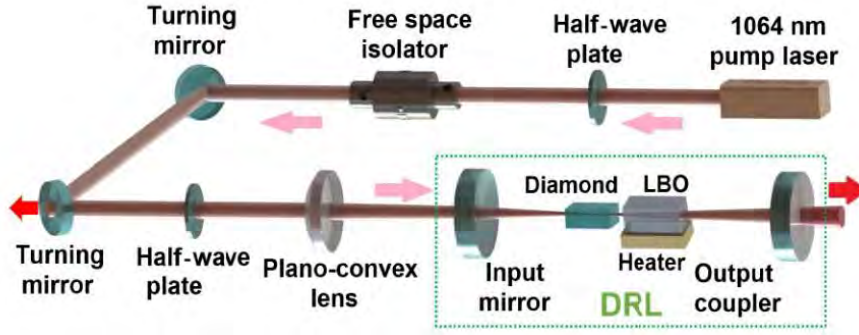


Figure 1-11 Diagram of SLM 620nm laser system [99].

This laser was designed to output the SHG of the Stokes shifted radiation. Interestingly he did not apply any passive locking or active cavity stabilization locking, even with a pump laser that is multi-longitudinal mode, however, he still achieved SLM output at high power output. The frequency stabilization mechanism here was the mode suppression effect of SHG, which was first presented by K. I. Martin et al. in 1997 [100]. More specifically, consider the situation with two modes oscillating: mode 1 is the main mode with intensity  $I(\omega_1)$  and frequency  $\omega_1$ , while mode 2 is the secondary mode. With sum-frequency mixing occurring in the cavity, the two modes see different nonlinear losses  $L$  as follows.

$$\frac{L_1}{L_2} = \frac{kI_1 + 2kI_2}{kI_2 + 2kI_1}, \quad (1-33)$$

where  $k$  is a constant related to the strength of the nonlinearity. As the intensity  $I_2 \ll I_1$ , the equation above is close to  $1/2$ , which means the brighter mode will see just half the nonlinear loss as the secondary mode. Based on this model, we can suppress secondary modes and stabilise single longitudinal mode lasing in cavities when we insert a SFM or SHG crystal.

## 1.5 Thesis outline

In this chapter, we reviewed continuous wave Raman laser theory and experiments, and the recent progress towards SLM operation. SLM operation is quite essential in many fields, and while steady progress has been made towards high-powers and increased wavelength access, SLM operation of Raman laser is still poorly understood. This is particularly true for pump

resonant Raman lasers: a practical analytical model is still missing, and there is only one report of SLM lasing. In this thesis, we aim to contribute towards filling this gap.

In Chapter 2 we derive a new analytic Raman model to describe the behavior of the pump resonant Raman lasers. The model is suitable for cascaded Raman lasers generating an arbitrary Stokes order. We quantitatively analyze the effects of various parameters in the model and develop optimization equations to maximize Stokes output.

In Chapter 3 we present a detailed description of the process to design, install, and align a ring resonator. We characterize the power curve and the spectrum data of the ring resonator Raman laser under the first Stokes and the second Stokes operation, and use the data to verify and improve our model. We explore the conditions for SLM operation in ring cavity systems, and also investigate the wavelength tunable performance of the laser.

In Chapter 4 we use a 1064 nm pump laser to build another second Stokes laser using diamond. We measure the reflected pump off the cavity and quantitatively analyze the mode matching coefficient of the analytic model to successfully explain the behavior of the reflected pump. We also design and build a ring cavity Raman laser using vanadate as the Raman gain medium. As vanadate has a very significant thermal lensing effect, we find the limits of this laser design.

In Chapter 5 we design and build a linear external cavity with double-passed pump, in order to explore the axial mode suppression effect of SHG as a method to stabilize the infrared spectrum. With the temperature adjustment of LBO to control the power of SHG, we show we can control the Stokes spectrum and achieve stable SLM Stokes lasing.

## 2

## Chapter 2. Modelling of continuous wave resonantly pumped Raman lasers

### 2.1 Introduction

Modelling of Raman lasers is well developed, including for: intracavity Raman lasers where the Raman and inversion gain share a laser cavity [101]; external-cavity Raman lasers, where only the Raman field is resonated, pumped by a non-resonated pump laser [18]; and cavity-enhanced Raman lasers, where the pump is resonantly coupled to a resonator containing the Raman crystal [102].

In this chapter, we report the modelling results of cavity-enhanced Raman lasers generating first Stokes or second-Stokes output. We developed an analytical model of cascaded Stokes conversion for this laser type, building on the work of Min et al [102] and Feigel et al [103]. Our model is more general, and we explore the approximations that were made in these papers.

We use the model to investigate the behavior of cavity enhanced Raman lasers and the dependence on the various design parameters. We have previously reported a first-stokes diamond laser generating 1 W at 883 nm using a continuous-wave (CW) Ti:sapphire laser at 890 nm [98]. We discuss these results in the context of our model. We use the model to design new laser cavities for the first and second Stokes operation, and build and characterize these lasers experimentally.

## 2.2 First Stokes model

### 2.2.1 Model derivation

We first derive a model for the first Stokes field of Raman laser, considering the effect of resonantly enhancing the pump. For a ring cavity, for optimum coupling to the cavity the incident pump power is resonantly enhanced inside the cavity by a factor [104]

$$\alpha = \frac{P_{Pintra}}{P_{Pinci}} = \left\{ \frac{(1-R_P)^{0.5}}{1-R_P^{0.5}G^{0.5}} \right\}^2, \quad (2-1)$$

where  $P_{Pintra}$  and  $P_{Pinci}$  are the intra-cavity pump power and incident pump power, respectively,  $R_P$  is the reflectivity of input mirror for the pump field. (Note that we will use the subscript P, S and SS to represent the parameters for the pump, first Stokes and second Stokes field, respectively.) The factor  $G$  is the round trip change in the pump power due to gain and loss; there is no gain for the pump in our case so this will be less than one due to both passive losses and depletion by conversion to Stokes power. The fraction of the incident pump power reflected from the input mirror is [104]

$$\beta = \frac{P_{Prefl}}{P_{Pinci}} = \left\{ \frac{R_P^{0.5} - G^{0.5}}{1 - R_P^{0.5}G^{0.5}} \right\}^2, \quad (2-2)$$

When the cavity losses equal input mirror transmission, we have  $R_P = G$ , and so  $\beta = 0$ , which means the pump field can fully couple into the cavity. We call this condition “impedance matched”.

This analysis assumes perfect mode matching of the incident beam parameters with the cavity mode (note that mode matching is distinct from impedance matching). In practice, it is difficult to keep perfect matching due to imperfections in the spatial mode, polarization error and error in the waist position. The unmatched fraction will always be reflected from the input mirror when the cavity is locked for coupling of the TEM<sub>00</sub> mode. We account for this by defining a mode matching factor  $\gamma$ :

$$P_{Pinci} = \gamma P_{Pincio} \quad (2-3)$$



where  $P_{Pinci0}$  is the full pump power incident on the cavity, and  $P_{Pinci}$  is the pump power that can be correctly coupled into the cavity. Now, the total power not coupled into the cavity  $P_{Prefl0}$  includes two parts: the mismatched fraction, and the fraction of the matched power rejected because of imperfect impedance matching  $P_{Prefl}$ :

$$P_{Prefl0} = (1 - \gamma)P_{Pinci0} + P_{Prefl} = (1 - \gamma)P_{Pinci0} + \beta\gamma P_{Pinci0}. \quad (2-4)$$

We will see that monitoring this reflected power will be an important way to evaluate the laser performance, and the signal source of the locking system.

The equations above describe the resonant enhancement of the pump laser. We can now model the Raman process inside the cavity, based on the approach in reference [105]. We assume that the laser fields are all in steady state, which makes sense for a cw laser. Consider the intracavity Stokes field. For a single round trip, Stokes loss and gain must cancel in steady state, allowing us to write an equation constraining the intracavity pump power:

$$R_S(1 - L_S)e^{\frac{g_S l P_{intra}}{A_1}} = R_S(1 - L_S)e^{\frac{g_S l \gamma \alpha P_{Pinci0}}{A_1}} = 1, \quad (2-5)$$

where  $R_S$  is the reflectivity of the output mirror for the first Stokes,  $L_S$  is Stokes passive loss,  $g_S$  is the gain coefficient for Stokes,  $l$  is the crystal length, and  $A_1$  is the overlap area of pump and Stokes fields. If the confocal parameter  $b$  satisfies  $b \gg l$  and the spots of Stokes and Pump are matched,  $A_1$  can be approximated as  $A_1 = \pi\omega^2$ , where  $\omega$  is the common radius of the beams [105]. If the crystal is Brewster cut, the beam in the crystal will become elliptical with the ratio between the long axis and short axis equal to the refraction index of the crystal. In a general case the effective area is the overlap integral  $A_{eff}$ , which can be derived from the Raman basic equations to be

$$\frac{1}{A_{eff}} = \frac{1}{l} \iint \overline{I_p(r, z)} \overline{I_s(r, z)} dA dz, \quad (2-6)$$

where  $\bar{I}$  is a normalized intensity profile

$$\overline{I_{p,s}(r, z)} = \frac{2}{\pi} \frac{1}{\omega_{p,s}^2(z)} \exp[-2(\frac{r}{\omega_{p,s}(z)})^2]. \quad (2-7)$$

in which the subscripts P, S refer to pump or Stokes fields. For details see appendix A

“General effective area derivation” .

Finally we must link the Stokes power to the loss for the pump field. First, the relationship between the Stokes output power and its intra-cavity power is:

$$P_{Sout} = (1 - R_S)P_{Sintra}. \quad (2-8)$$

Based on the Ref [105] we can then write the round-trip fraction  $G$  for the pump as

$$G = (1 - L_P)e^{-\frac{g_P P_{Sintra} l}{A_1}} = (1 - L_P)e^{-\frac{g_S P_{Sout} l}{A_1 \eta_S (1 - R_S)}}, \quad (2-9)$$

where  $g_S = \eta_S g_P$  and  $\eta_S = \frac{\lambda_p}{\lambda_s}$  is quantum defect of the process.

When Eqs. (2-1), (2-5) and (2-9) are combined to eliminate  $\alpha$  and  $G$ , we find the first Stokes output power is expressed as

$$P_{Sout} = \frac{\eta_S A_1 (1 - R_S)}{g_S l} \left\{ \ln[R_P (1 - L_P)] - 2 \ln \left[ 1 - \sqrt{\frac{P_{incio}}{P_{Sth}}} \left( 1 - \sqrt{R_P (1 - L_P)} \right) \right] \right\}. \quad (2-10)$$

where  $P_{Sth}$  is

$$P_{Sth} = - \frac{A_1 \ln [R_S (1 - L_S)] [1 - \sqrt{R_P (1 - L_P)}]^2}{g_S l \gamma (1 - R_P)}. \quad (2-11)$$

$P_{Sth}$  is the pump power for reaching Stokes threshold  $P_{Sout} = 0$ . Note that during the derivation of eq (2-10), the absolute value  $|1 - \sqrt{R_P G}|$  can be simplified to  $1 - \sqrt{R_P G}$  because  $R_P < 1$  and  $G < 1$ . Equation (2-10) is the most general form for the first Stokes laser output power.

The pump power reflected from the cavity reaches a minimum at the impedance matching condition  $R_P = G$ , achieved for a pump power of

$$P'_{Pincio} = \frac{A_1 (1 - R_P)}{g_S l \gamma} \ln \left( \frac{1}{R_S (1 - L_S)} \right). \quad (2-12)$$

At this impedance matching point, the Stokes output power is

$$P'_{Sout} = \frac{A_1 \eta_S (1 - R_S)}{g_S l} \ln \left( \frac{1 - L_P}{R_P} \right). \quad (2-13)$$

In the ring cavity, the Stokes field can operate in both directions (forward and backward) with identical gain, both depleting the pump in the same way. The  $P_{Sintra}$  and  $P_{Sout}$  mentioned above are the sum of the fields in both directions. With nothing breaking the forward-backward symmetry, for a given Stokes output power, the model is stable for any

ratio in the forwards and backwards directions and so makes no predictions about what this ratio would be. This agrees with the result from Kitzler [98] that showed a forward:backward ratio that drifted with time. He also demonstrated that breaking the symmetry with a retroreflecting mirror could make the Stokes oscillate predominantly unidirectionally. We will use the same method in our experiments.

### Exponential approximation

While the equations above are the most general, simplifications can be useful and can better illustrate the physics. Firstly Eq. (2-5) can be rearranged and simplified by approximating  $\ln(1/x) \approx 1 - x$ , valid when  $x \rightarrow 1$ , to

$$\alpha = \frac{(1-R_S+L_S)A_1}{g_s l \gamma P_{Pincio}}. \quad (2-14)$$

This approximation is valid for a setup with low loss and high reflectivity, i.e.,  $R_P, R_S \approx 1$  and  $L_P, L_S \ll 1$ . Next, using approximation  $e^x \approx 1 + x$ , valid when  $x \ll 1$  we can simplify Eq.(2-9) as

$$G = (1 - L)e^{-\frac{g_p P_{Sintra} l}{A_1}} = (1 - L) \left( 1 - \frac{g_p P_{Sintra} l}{A_1} \right) \approx 1 - L - \frac{g_p P_{Sintra} l}{A_1}, \quad (2-15)$$

This is justified when  $\frac{g_p P_{Sintra} l}{A_1} \ll 1$ , corresponding to weak depletion of the pump by the Stokes field on each round trip. Using these assumptions, the Stokes output  $P_{Sout}$  and Stokes threshold  $P_{th}$  become

$$P_{Sout} = \frac{A_1 \eta_s}{g_s l R_P} (1 - R_S) \left\{ R_P - R_P L_P - \left[ 1 - \sqrt{\frac{g_s l \gamma P_{Pincio} (1 - R_P)}{(1 - R_S + L_S) A_1}} \right]^2 \right\}, \quad (2-16)$$

$$P_{Sth} = \frac{(1 - R_S + L_S) A_1 (1 - \sqrt{R_P - R_P L_P})^2}{g_s l \gamma (1 - R_P)}. \quad (2-17)$$

### Root approximation

Alternatively, if we set  $f(x) = R_P^{0.5} G^{0.5}$  with  $x = R_P G$ , under the assumption  $R_P G \rightarrow 1$  we can Taylor-expand the function and take the first two components as follows:

$$f(x) = R_P^{0.5} G^{0.5} = 1 + \frac{R_P G}{2} - \frac{1}{2} + o(R_P G - 1) \approx \frac{1}{2} + \frac{R_P G}{2}. \quad (2-18)$$

Now eq. (2-1) is simplified as

$$\alpha = \frac{4(1-R_P)}{(1-R_P G)^2}, \quad (2-19)$$

The 1<sup>st</sup> Stokes output and its threshold now becomes

$$P_{Sout} = \frac{A_1 \eta_S (1-R_S)}{g_S l} \ln \left\{ \frac{R_P (1-L_P)}{1 - \sqrt{\frac{4(1-R_P)g_S l \gamma P_{Pinci}}{\ln\left(\frac{1}{R_S(1-L_S)}\right)A_1}}} \right\}, \quad (2-20)$$

$$P_{Sth} = \frac{(1-R_P(1-L_P))^2 \ln\left(\frac{1}{R_S(1-L_S)}\right)A_1}{4(1-R_P)g_S l \gamma}. \quad (2-21)$$

This form is the same as the form derived in Min *et al.* [102].

If we combine both the exponential approximation and root approximation, then we get the simplest form of first Stokes output as

$$P_{Sout} = \sigma_S \left( \frac{\sqrt{P_{Pinci0}}}{\sqrt{P_{Sth}}} - 1 \right), \quad (2-22)$$

with threshold pump power

$$P_{Sth} = \frac{(1-R_S+L_S)A_1}{4g_S l \gamma (1-R_P)} (1 - R_P + L_P R_P)^2 \quad (2-23)$$

and slope efficiency

$$\sigma_S = \frac{A_1 \eta_S (1-R_S) \left( \frac{1}{R_P} - 1 + L_P \right)}{g_S l}. \quad (2-24)$$

## 2.2.2 Model analysis

Let us now investigate the model predictions using parameters for diamond. We set the Raman gain  $g_S = 15.4 \times 10^{-11}$  GW/cm<sup>-1</sup> (@1087 nm) [106], the crystal length  $l = 5$  mm,  $\lambda_P = 950$  nm. From the Raman shift of diamond of 1332 cm<sup>-1</sup> we can deduce the  $\lambda_s =$

1087 nm and  $\lambda_{ss} = 1271$  nm. The refractive index of diamond is  $n = 2.4$  for all fields. For now, we assume the mode matching coefficient  $\gamma$  is 1, and the  $M^2$  of the fields is 1. All fields have the same confocal parameter. Note that in this part, “radius” means the waist radius of the beams in the cavity.

### The Stokes output power and conversion efficiency

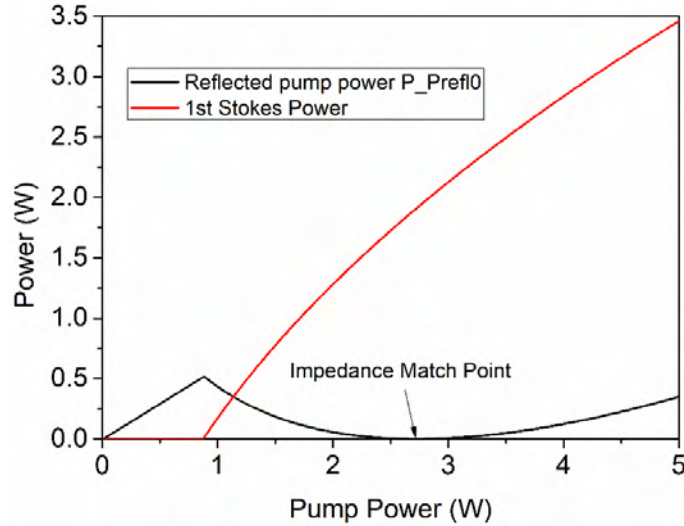


Figure 2-1 The first Stokes output power and residual pump power as a function of pump power ( $R_p=97\%$ ,  $R_s=97\%$  Loss=0.25%, radius=20  $\mu\text{m}$ ).

Figure 2-1 is the modelled output behavior of the first Stokes field for typical parameters of resonantly pumped DRLs. The red line is the first Stokes output power, while the black line is the pump power reflected from the cavity. We see that the reflected pump power declines above the 1<sup>st</sup> Stokes threshold; the Stokes presents additional loss to the intracavity pump field on top of the passive losses, and when that total loss equals the pump transmission of the input mirror, we meet the impedance matching condition and the pump reflection goes to zero. For stronger pump and thus even larger Stokes field, the loss increases and the reflected pump increases again as the cavity moves away from the impedance matching point. Note that based on the impedance matching condition  $R_p = G$ , when we substitute the Eq. (2-9), we can deduce that the passive loss must be lower than the input mirror transmission to achieve the impedance match for some Stokes power; otherwise, the rejected pump

continues to go up above the Stokes threshold. This rule is also true in the second Stokes model.

To investigate the effect of different passive loss and beam size, we compare the Stokes output power and conversion efficiency as a function of the pump power against these parameters. First consider a change of the beam radii, shown in Figure 2-2.

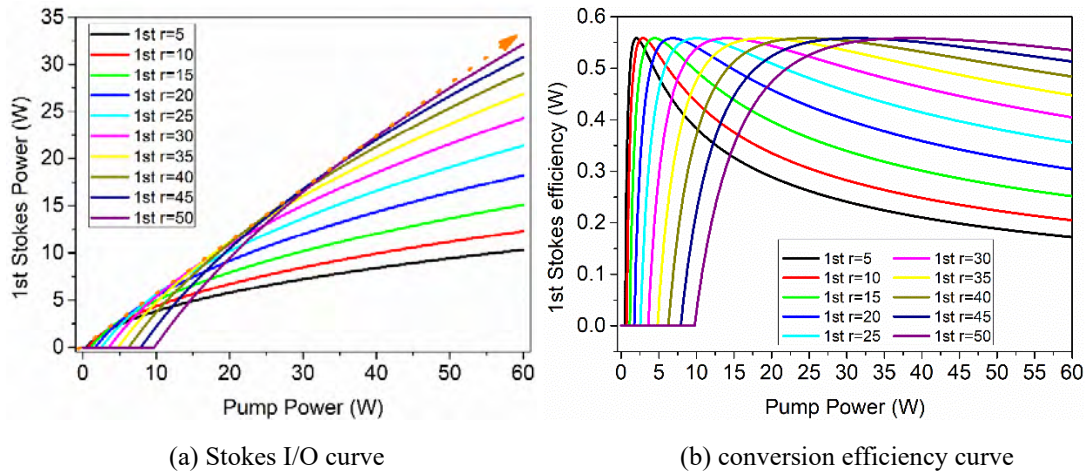


Figure 2-2 The first Stokes output power (a) and conversion efficiency (b) as a function of the pump power with the change of radius ( $R_P=97\%$   $R_S=97\%$ , Loss=0.75%).

We can see in the 1<sup>st</sup> Stokes output graph, as the radius increases, the threshold also increases. All the curves at some point touch the same maximum output efficiency, marked as the orange arrow. This is perhaps easier to see in the conversion efficiency graph in Figure 2-2b, which shows the 1<sup>st</sup> Stokes can only hit the maximum conversion efficiency at one pump input point.

The change in the conversion efficiency can be explained by the impedance condition. If the impedance condition is met, the pump power can be 100% coupled into the resonator; if the impedance condition is not met, the reflected pump cannot contribute. As we saw in Figure 1, there is only one pump power that is impedance matched for each laser design, and this matched power increases with beam radius. The maximum efficiency at the impedance matched point is set by the passive losses. Any loss is counterproductive in the Raman laser, decreasing the Stokes output, the conversion efficiency, and increasing the threshold. Therefore, we should strive to minimize the loss in the DRL design.

### The Stokes output power as the function of mirror reflectivity

Designing the right input/output mirror reflectivities is vital. To understand the role of mirror reflectivity, we use contour maps to show the relationship between  $R_P$ ,  $R_S$ , and Stokes Power.

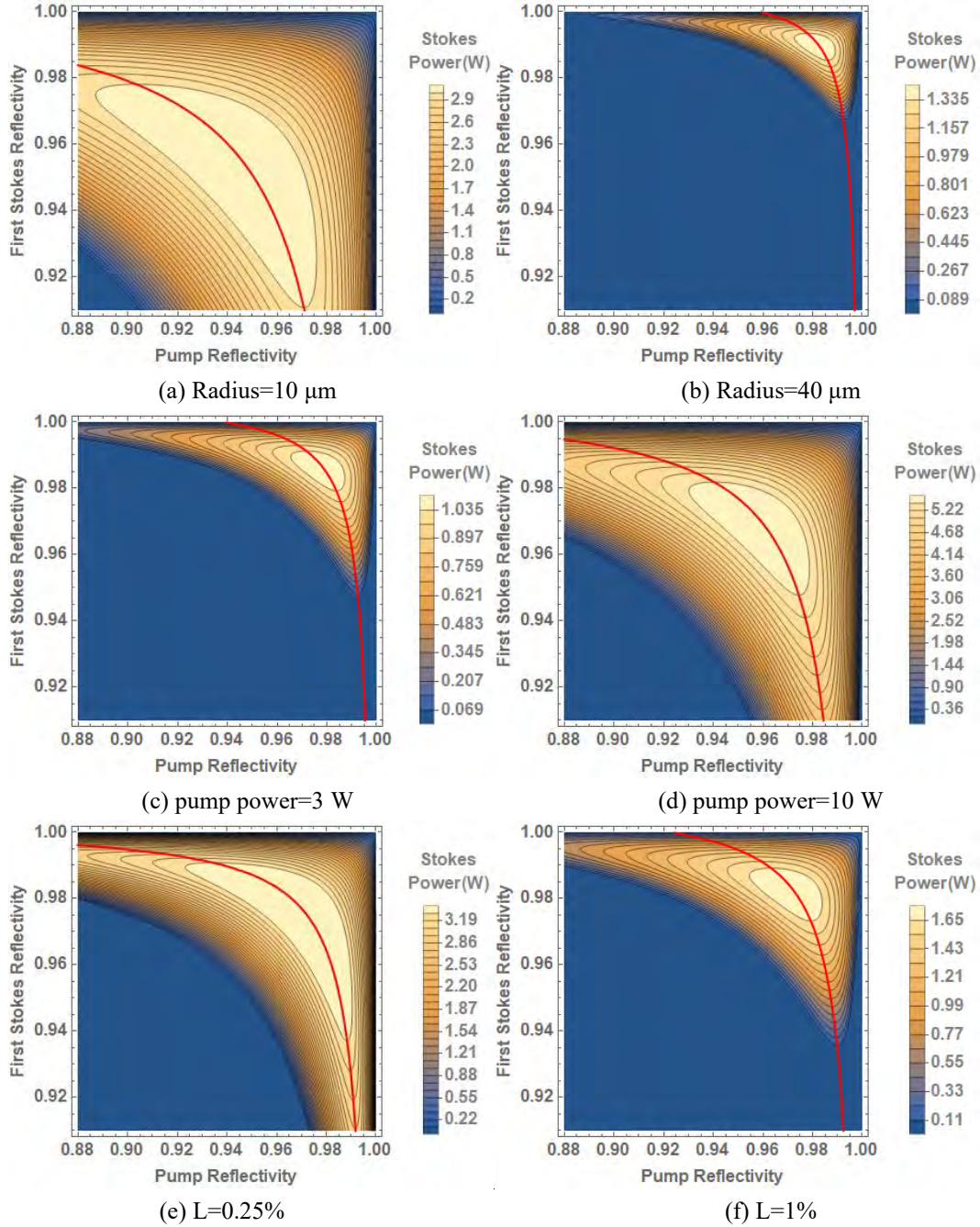


Figure 2-3 The relationship between  $R_P$ ,  $R_S$ , and Stokes Power for pairs of different radius, pump power, and passive loss. The Stokes power is shown as the contours with different colors shown in the legend. Each plot has one changed parameter value, which otherwise take default values of Pump power=5 W Loss=0.75%, and radius=25  $\mu\text{m}$ . The red line shows reflectivity combinations that fit the impedance matching condition.

Figure 2-3 shows contour maps of the Stokes power as the function of  $R_P$ ,  $R_S$ , with three pairs showing the effects of different radius, different pump power, and different passive loss. The x-axis is the mirror reflectivity for the pump while the y-axis is its reflectivity of the first Stokes. The lasing region expands to include lower reflectivity values for decreasing beam radius, decreasing passive loss increasing pump power. This follows since these changes all reduce the Stokes threshold.

The red line, showing mirror configurations that meet the impedance matching condition, as expected always passes through the highest point of the contour map. The contour shape and the impedance matched line have a strong element of symmetry across the  $R_P = R_S$  line, which means a larger transmission for one field must be counteracted by a smaller transmission for the other.

The red line implies the  $R_P$  is inversely correlated with  $R_S$  for fixed pump power. For example, when  $R_S$  goes down, the Stokes field is not so strongly resonated as before: the decreased intracavity Stokes power makes the  $G$  value closer to 1, and based on the impedance match condition,  $R_P$  needs to increase to achieve impedance matching again.

Impedance matching is only one element of overall efficiency along with the efficiency of converting the in-coupled pump photons to Stokes, and the efficiency of outputting Stokes photons which is  $(1 - R_S)/(1 - R_S + L_S)$ . Passive loss can affect each conversion stage. As a result of these other efficiency elements, the optimum  $R_S$  for a given  $R_P$  may not be impedance matched. The figures above show that for a given  $R_P$ , the  $R_S$  that meets the impedance match is close to the optimum but not always exactly at the optimum, particularly for the low  $R_P$  part, where the very high matched  $R_S$  would result in very low output coupling efficiency. For some  $R_P$  values, there is no possibility of impedance matching as the passive loss for the pump  $L_P > (1 - R_P)$ , and so  $R_P > G$  even for no Stokes field and the impedance condition cannot be met.

From Figure 2-3 we can see for diamond, pump lasers of 5 W output power are clearly enough to build an effective laser, since losses of the scale 1% are easily achievable with Brewster diamond or even with AR coatings.



## 2.3 Second Stokes model

### 2.3.1 Model derivation

We now move on to model a second Stokes laser with cavity-enhanced pumping. In the second Stokes model derivation, the accumulated first Stokes field serves as a pump for the second Stokes field. The base equations describing pump enhancement (2-1)~(2-4) and the Gaussian nature of interacting beams (2-6), (2-7) remain valid. The eq. (2-5) which asserts that the Stokes field is in steady state is modified to include loss due to the conversion to second Stokes as

$$R_S(1 - L_S)e^{-\frac{g_S l P_{SSintra}}{A_2}} e^{\frac{g_S l P_{Pintra}}{A_1}} = 1, \quad (2-25)$$

where  $A_1$  and  $A_2$  are the overlap areas of the pump and first Stokes field and first Stokes and second Stokes field, respectively, and  $P_{SSintra}$  is the second Stokes intracavity power. Expressing the second Stokes output power using second Stokes reflectivity  $R_{SS}$  of the IC/OC as  $P_{SSout} = (1 - R_{SS})P_{SSintra}$ , and using  $P_{Pintra} = \alpha \gamma P_{Pincio}$  (from Eqs. (2-1) and (2-3)) we find

$$P_{SSout} = (1 - R_{SS}) \left( \frac{A_2 \alpha \gamma P_{Pincio}}{A_1} - \frac{A_2 \ln \left( \frac{1}{R_S(1 - L_S)} \right)}{g_S l} \right). \quad (2-26)$$

This equation still contains  $\alpha$ , so there is more work to do. We can write a ‘gain=loss’ equation for the second Stokes field in steady state, which is

$$R_{SS}(1 - L_{SS})e^{\frac{g_{SS} l P_{SSintra}}{A_2}} = R_{SS}(1 - L_{SS})e^{\frac{\eta_{SS} g_S l P_{SSintra}}{A_2}} = 1, \quad (2-27)$$

where  $g_{SS} = \eta_{SS} g_S$  is the second Stokes gain coefficient and  $\eta_{SS} = \frac{\lambda_S}{\lambda_{SS}}$ . Combining eqs. (2-27) and (2-9) we find

$$G = (1 - L_P) [R_{SS}(1 - L_{SS})]^{\frac{A_2 \lambda_{SS}}{A_1 \lambda_P}}. \quad (2-28)$$

Substituting Eq. (2-28) into (2-1) gives us an expression for  $\alpha$ , which we then eliminate from Eq. (2-26). We finally retrieve a simple form for the second Stokes output power

$$P_{SSout} = \sigma_{SS}(P_{inci0} - P_{SSth}), \quad (2-29)$$

where

$$\sigma_{SS} = \gamma \frac{A_2}{A_1} \frac{(1-R_{SS})(1-R_P)}{\left(1 - \sqrt{R_P(1-L_P)(R_{SS}(1-L_{SS}))^{\frac{A_2}{A_1 \eta_S \eta_{SS}}}}\right)^2} \quad (2-30)$$

represents linear slope efficiency and  $P_{SSth}$  is the pump threshold for second Stokes

$$P_{SSth} = \frac{A_1}{g_s l \gamma (1-R_P)} \left( \sqrt{R_P(1-L_P)[R_{SS}(1-L_{SS})]^{\frac{A_2}{A_1 \eta_S \eta_{SS}}}} - 1 \right)^2 \ln[R_S(1-L_S)]. \quad (2-31)$$

Above the second Stokes threshold, we see that  $G$ , and thus the first Stokes power as well, is constant according to eqs. (2-28)(2-29). Therefore,  $\alpha$  is also constant and since  $\alpha P_{Pinci} = P_{Pintra}$  the intracavity pump power starts to grow above the second Stokes threshold. It means however, that  $\beta$  is also constant and, using eq.(2-28),  $R_{SS}$  can be used to place second Stokes threshold at the impedance matched pump power. From eq. (2-1),  $\beta = 0$  for  $R_P = G$  and using eq. (2-28) the required second stokes reflectivity is

$$R_{SS} = \frac{1}{(1-L_{SS})} \left( \frac{R_P}{1-L_P} \right)^{\frac{A_1 \eta_S \eta_{SS}}{A_2}}. \quad (2-32)$$

The impedance matching condition does not contain pump, Stokes or second Stokes power; hence a second Stokes laser can be impedance matched for all output powers.

### Exponential approximation

Use the same exponential approximation mentioned in the first Stokes part, we can rewrite the eq. (2-25) as

$$L_S + (1 - R_S) + \frac{g_s P_{SSintra} l}{A_2} = \frac{g_s l P_{Pintra}}{A_1}. \quad (2-33)$$

And eq. (2-27) is simplified as

$$(1 - R_{SS}) + L_{SS} = \frac{g_{ss} P_{Sintra} l}{A_2} = \frac{\eta_{ss} g_s P_{Sintra} l}{A_2}. \quad (2-34)$$

At last, the second Stokes output slope efficiency is

$$\sigma_{SS} = \gamma \frac{A_2}{A_1} \frac{(1-R_{SS})(1-R_P)}{\left(1 - \sqrt{R_P \left[1 - L_P - \frac{A_2(1-R_{SS}+L_{SS})}{A_1 \eta_S \eta_{SS}}\right]}\right)^2} \quad (2-35)$$

and the corresponding threshold is

$$P_{SSth} = \frac{A_1(L+1-R_S)}{g_s l \gamma \left\{ \frac{(1-R_P)^{0.5}}{1-R_P^{0.5} \left(1-L_P - \frac{A_2(1-R_{SS}+L_{SS})}{A_1 \eta_S \eta_{SS}}\right)^{0.5}} \right\}^2}. \quad (2-36)$$

### Root approximation

Use the root approximation eq.(2-18) the output and its threshold of the second Stokes slope efficiency and threshold can be rewritten as

$$\sigma_{SS} = \gamma \frac{A_2}{A_1} \frac{4(1-R_{SS})(1-R_P)}{1-R_P(1-L_P)(R_{SS}(1-L_{SS}))^{\frac{A_2}{A_1 \eta_S \eta_{SS}}}}, \quad (2-37)$$

$$P_{SSth} = \frac{A_1 \ln \left( \frac{1}{R_S(1-L_S)} \right) \left( 1-R_P(1-L_P) [R_{SS}(1-L_{SS})]^{\frac{A_2}{A_1 \eta_S \eta_{SS}}} \right)^2}{4(1-R_P)g_s l \gamma}. \quad (2-38)$$

After the root approximation, our 2<sup>nd</sup> Stokes model agrees with the results from Min et al. [102], although here we have a more explicit connection to cavity parameters.

If we combine exponential approximation and root approximations, the slope efficiency and threshold can be simplified as

$$\sigma_{SS} = \frac{4\gamma A_2(1-R_P)(1-R_{SS})}{A_1 \left\{ 1-R_P \left[ (1-L_P) - \frac{A_2 \lambda_{SS}(1-R_{SS}+L_{SS})}{A_1 \lambda_p} \right] \right\}^2}, \quad (2-39)$$

$$P_{SSth} = \frac{A_1(L_S+1-R_S) \left\{ 1-R_P \left[ (1-L_P) - \frac{A_2 \lambda_{SS}(1-R_{SS}+L_{SS})}{A_1 \lambda_p} \right] \right\}^2}{4(1-R_P)g_s l \gamma}. \quad (2-40)$$

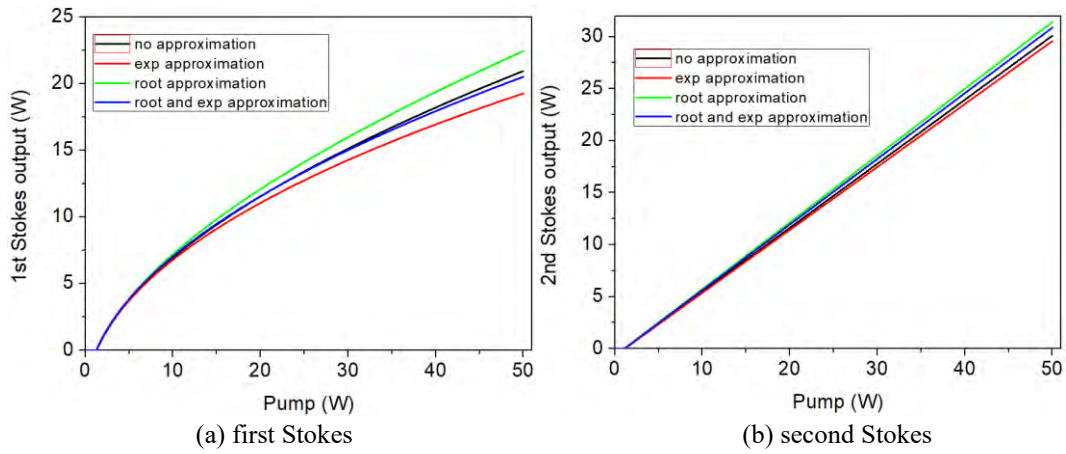


Figure 2-4 A comparison of different approximations using the power input/output graph ( $R_p=97\%$ ,  $R_S=97\%$ @fig4-a  $R_S=99.8\%$ @fig4-b,  $R_{SS}=97\%$  Loss=0.25%, radius=20  $\mu\text{m}$ ,  $\lambda_p=950\text{ nm}$ ).

It is worth noting that the approximation we discussed above is valid for the low pump power region and small output coupling transmissions. Figure 2-4 compares the approximations to the exact solution for both first and second Stokes results. For the cavity parameters we have been using, the difference is small when pump power is below 10 W, and remain accurate for substantially higher second Stokes pump powers. As the root approximation overestimates and the exponential approximation underestimate the output, their combination is closer to non-approximated equations than either alone.

### 2.3.2 Model analysis

We now investigate the behavior of the second Stokes laser model. The parameters we used in the model is the same as we mentioned in the 1st Stokes model: Raman gain  $g_S = 15.4 \times 10^{-11} \text{ GW/cm}^{-1}$  (@1087 nm) [106], crystal length  $l = 5 \text{ mm}$ ,  $\lambda_p = 950 \text{ nm}$ .  $\lambda_s = 1087 \text{ nm}$  and  $\lambda_{ss} = 1271 \text{ nm}$ .  $n = 2.4$   $\gamma=1$ , and the  $M^2=1$ . Note that the 1st Stokes reflectivity  $R_S$  is set to 99.8% in the 2nd Stokes model.

### The Stokes output power and the conversion efficiency

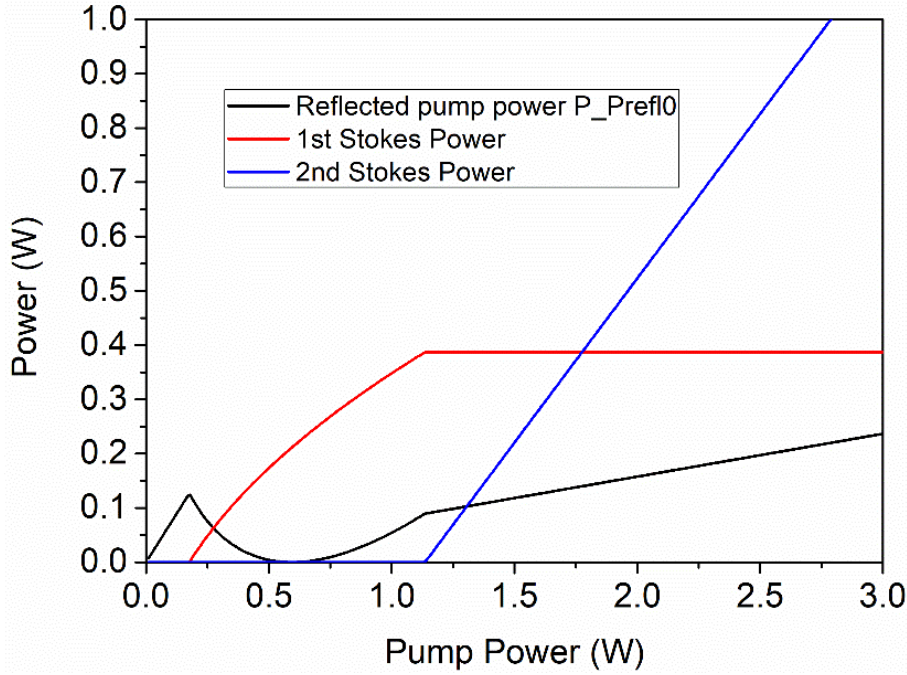


Figure 2-5 The second Stokes output power and residual pump power as a function of pump power ( $R_P=97\%$ ,  $R_S=99.8\%$ ,  $R_{SS}=97\%$  Loss=0.25%, radius=20  $\mu\text{m}$ ).

Figure 2-5 shows the behavior of a second Stokes laser. The blue line is the 2<sup>nd</sup> Stokes output. When pump power reaches the second Stokes threshold, it is interesting that the 1<sup>st</sup> Stokes keeps steady while the reflected pump field and the second Stokes field start to grow linearly. The form of the second Stokes output (eq. (2-29)) shows the linear relationship between pump power and the second Stokes output power, with the slope efficiency independent to the pump power. Equation (2-27) implies the first Stokes field will keep steady at a fixed value for all output powers above second Stokes threshold. The clamped Stokes field can resist pump noise, which brings potential for applications that require stable power output.

Looking at eq (2-32), we see that the impedance match condition does not include the pump power. This means that by optimizing the parameters, we can achieve impedance matching for all output powers. This is in contrast to the first Stokes laser, for which impedance matching only occurs for one pump power. Figure 2-6 shows a second Stokes laser for which the resonator meets the second Stokes impedance match condition.

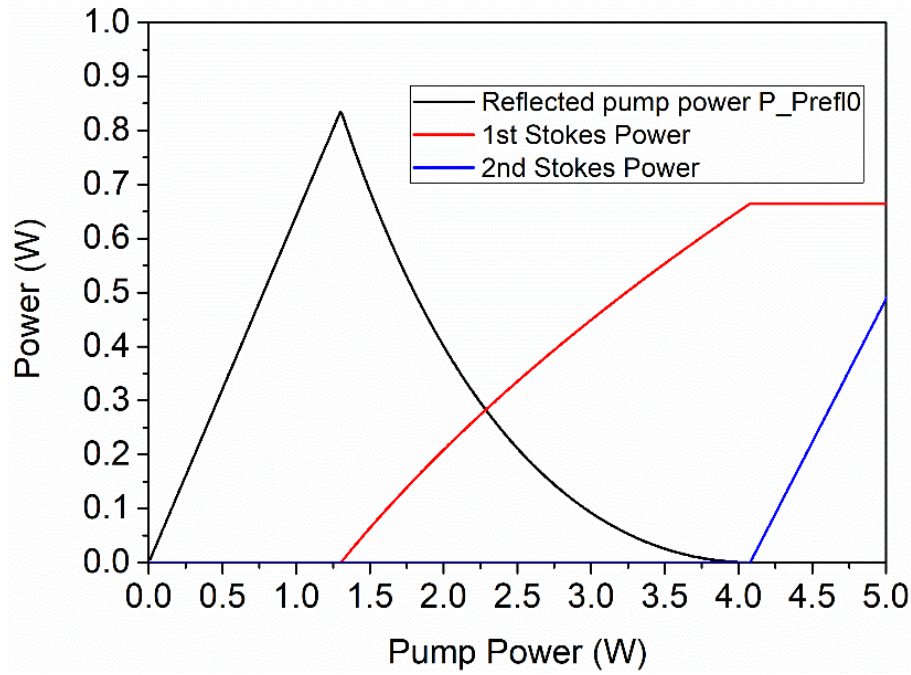


Figure 2-6 The Stokes output power as a function of pump power ( $R_p=93.4\%$ ,  $R_S=99.8\%$ ,  $R_{SS}=97\%$  Loss=0.75%, radius=25  $\mu\text{m}$ ).

The reflected pump power goes to zero when the pump power reaches the 2<sup>nd</sup> Stokes threshold. Because  $G$  in 2<sup>nd</sup> Stokes model is only related to  $R_{SS}$  and  $L$ , the impedance match condition can be always fulfilled above the 2<sup>nd</sup> Stokes threshold. For the pump field, the first Stokes field is a loss source, and so as the first Stokes field is clamped, the total loss is steady. That means we can arrange for the clamped first Stokes power to control the total pump loss to its impedance matched value.

Figure 2-7 shows the effect of the loss and beam size on the second Stokes power output. We see that the radius does not affect the slope efficiency but rather just the threshold of the laser. We can see this in eq. (2-30). The overall conversion efficiency approaches the same value (the slope efficiency) in each case. In practice, using a very small radius makes the laser less stable and harder to build, and we found that a radius around 20  $\mu\text{m}$  is feasible to achieve a stable setup.

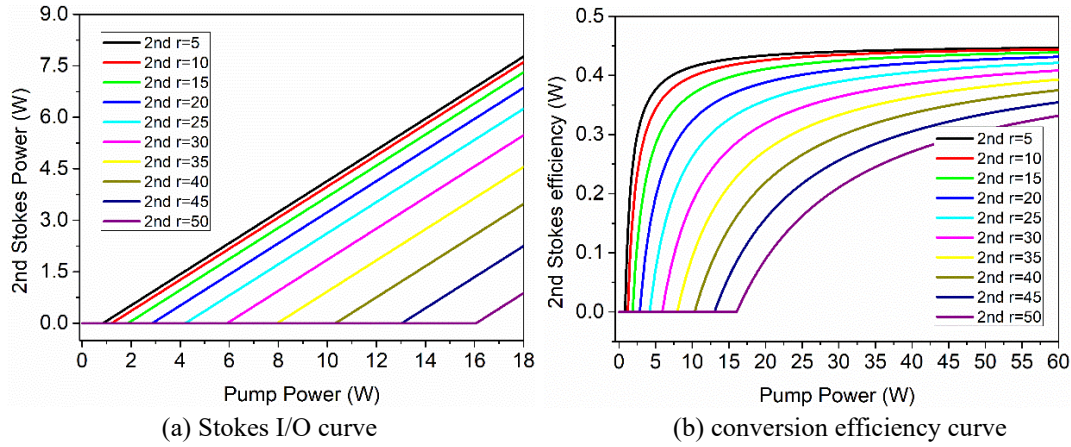
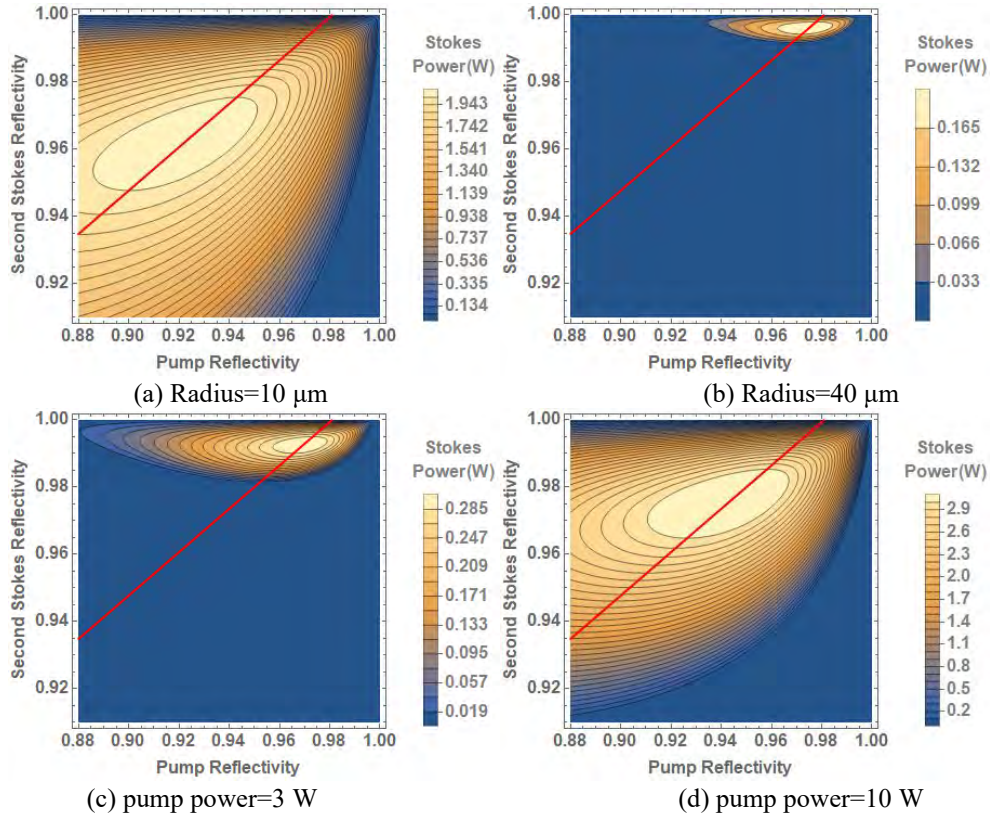


Figure 2-7 The second Stokes output power (a) and conversion efficiency (b) as a function of the pump power with the change of radius ( $R_{SS}=97\%$   $R_P=97\%$   $R_S=99.8\%$ , Loss=0.75%).

### The second Stokes output power as the function of mirror reflectivity

Similarly to Figure 2-3, we can generate the contour maps of second Stokes power as a function of the IC/OC pump reflectivity and the second Stokes reflectivity as Figure 2-8 shows below. The first Stokes reflectivity is HR in the ideal case, but set to a practical value of 99.8% here.





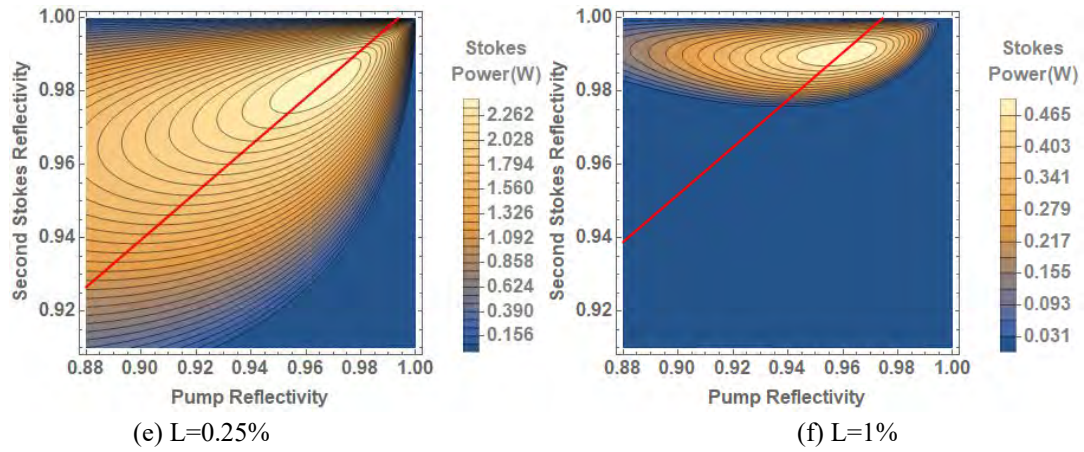


Figure 2-8 The relationship between  $R_P$ ,  $R_{SS}$ , and Stokes Power in different radius, pump power, and passive loss, where the second Stokes power is shown as the contours with different colors. The legend bar shows the Stokes power change with the color. Default parameter values (unless labelled) are pump power=5 W Loss=0.75%, radius=25  $\mu\text{m}$   $R_S=99.8\%$ . The red line is the positions that fit the impedance matching condition.

Compared to the first Stokes model results, again a decrease of radius, increase of pump power and decrease of loss all cause the optimums to move towards lower reflectivities. The contour shapes are elliptical, asymmetric to the  $R_P = R_S$  line, with the second Stokes power more sensitive to  $R_{SS}$  than  $R_P$ . When designing these lasers, we will need to pay more attention to  $R_{SS}$  tolerance.

Mirror values that meet the impedance matching condition fall on the red line. Due to the stability feature of the 2<sup>nd</sup> Stokes impedance match condition, the red line is independent of the radius and pump power. The optimum second Stokes output point moves along the red line as we change radius and pump power. While the optimal point is on the impedance match line, in general, and different to the first Stokes laser, the optimum  $R_{SS}$  for a given  $R_P$  does not closely follow the impedance match line. Compare to the first Stokes model, the second Stokes model has an additional efficiency component - the efficiency of conversion from the first Stokes to the second Stokes field - which seems to make the weighting of impedance matching efficiency element smaller. As a result, impedance matching is not a good guide to mirror choice away from the global optimum.



## 2.4 The mode mismatch factor

The modelling result we discussed until now was based on the situation of perfect mode matching of the pump to the cavity, i.e.,  $\gamma=1$ . In practice, however, the mode cannot be 100% matched. So, we need to explore the behavior for  $\gamma<1$ . We will only discuss the second Stokes model as it includes the first Stokes behavior below the second Stokes threshold.

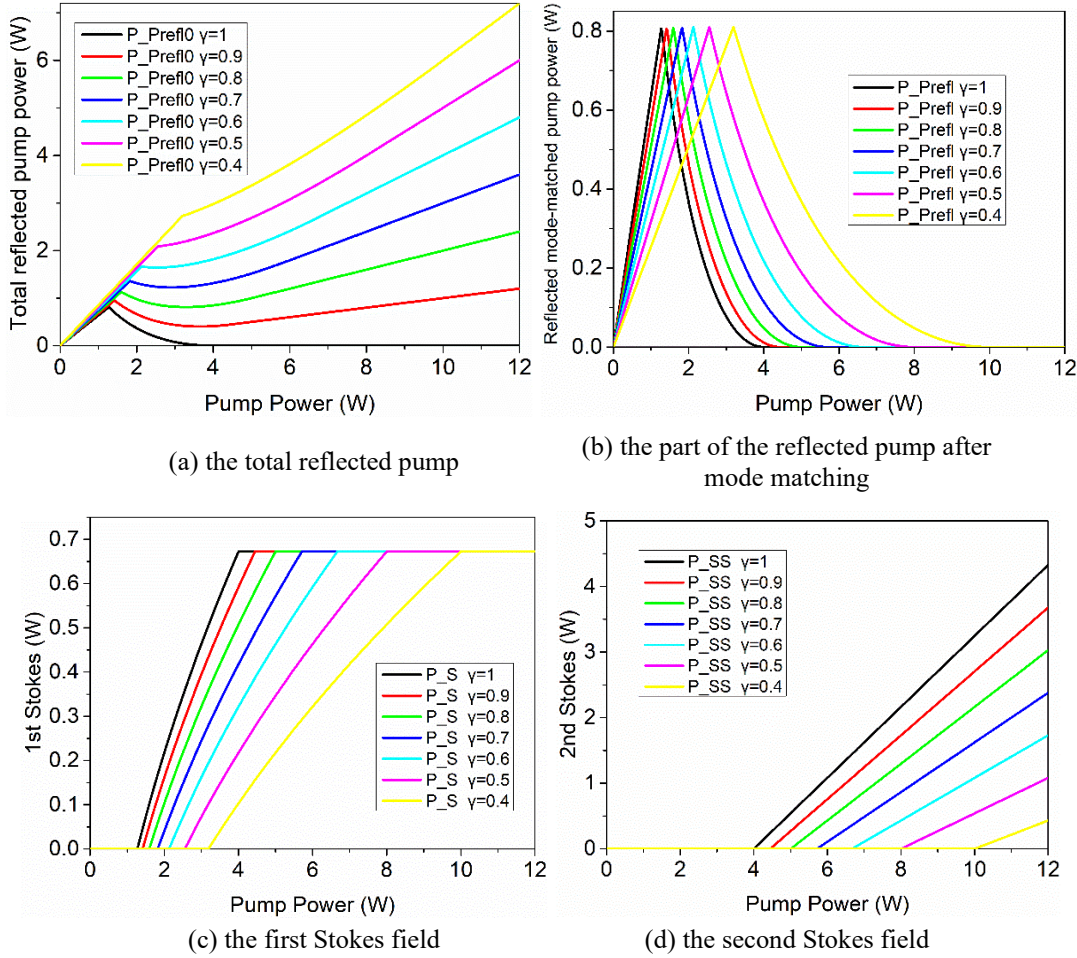


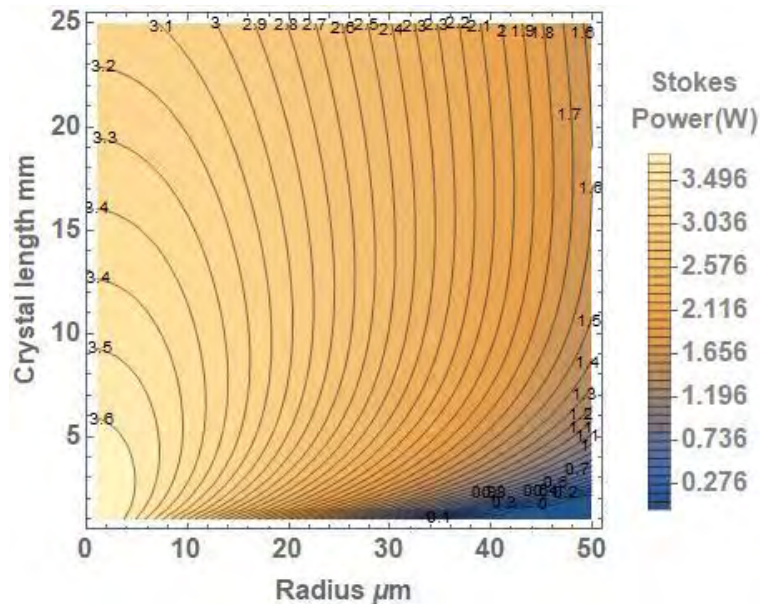
Figure 2-9 The power input/output curve for; (a) the reflected pump, (b) the part of the reflected pump after mode matching, (c) the first Stokes field, and (d) the second Stokes field for different  $\gamma$  values.

The Figure 2-9 shows the behavior of a second Stokes laser as a function of pump power, for a range of different mode matching factors  $\gamma$ . As  $\gamma$  decreases, plots (c) and (d) show that the thresholds of the first and second Stokes are increased, while the second Stokes output slope is also degraded; this happens because the fraction of the pump power able to couple

to the cavity is less. Plot (a) shows the total power reflected from the cavity; this includes both terms in Eq. (2-4): the amount  $(1 - \gamma)P_{P_{inc}0}$  of the pump that is not mode matched and can't be coupled in, and the part  $\beta\gamma P_{P_{inc}0}$  which is the part of the matched pump power that is rejected because of imperfect impedance matching. This second part is shown separately in plot (b) where we can see that the second Stokes laser is impedance matched above second Stokes threshold. In the Figure 2-9a, we see that even for  $\gamma$  close to 1, the reflected pump power behavior is significantly changed.

## 2.5 Crystal length selection

In order to investigate the effect of crystal length on a first Stokes laser, we plot the contour graph to demonstrate the relationship of beam radius, crystal length, and Stokes output. For easy comparison, the IC/OC reflectivity for pump and Stokes field is optimum, and mode matching  $\gamma=1$ . As some part of passive loss  $L$  is related to crystal length, we redefine the loss as  $L = \alpha l + L_p$ , where  $\alpha$  is the absorption coefficient of diamond and  $L_p$  is the passive loss excluding that due to diamond absorption. In this case we set,  $\alpha=0.0025 \text{ cm}^{-1}$  [107] and  $L_p=0.5\%$ . Simulations are shown in Figure 2-10 and Figure 2-11.



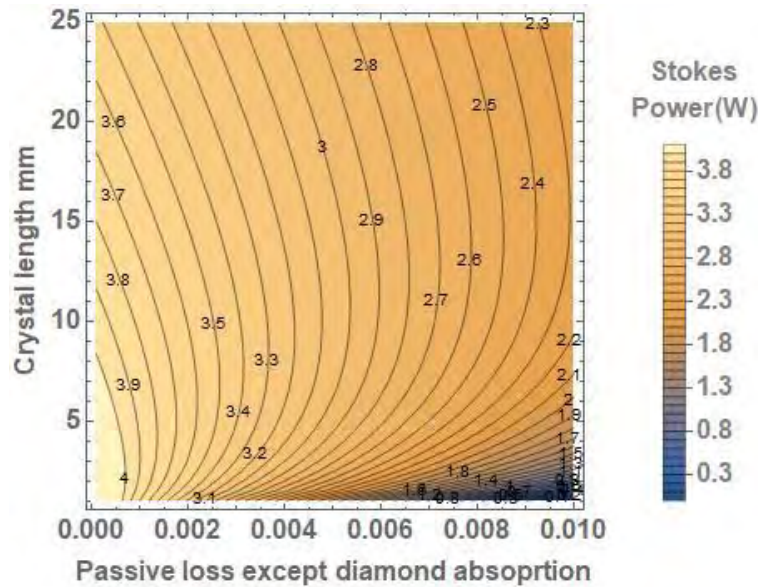


Figure 2-11 The relationship between loss, crystal length and Stokes output for optimum mirrors (radius=20  $\mu\text{m}$  Pump power=5 W)

The results show the crystal length has an optimum value, not simply longer the crystal the better. For example, if the radius is fixed at 20  $\mu\text{m}$ , and loss is 0.2% the optimum diamond is 5 mm long. We can use this crystal optimum graph to obtain the best balance between gain and total loss in the system. As we focus tighter, the optimum diamond is shorter since the tighter focus gives more gain; for lower passive losses, the optimum diamond is shorter, since the diamond loss becomes more important. Threshold contour graphs (not shown here) show identical trends but with different values. That means the parameters generating maximum output power may not lead to the minimizing of threshold at the same time. The crystal optimization analysis can guide us to choose the length of the crystal. Usually, the minimum radius is not below 20  $\mu\text{m}$ , so the optimum crystal length is about 10 mm if the loss is about 0.5%. Our crystals are 7 mm long, so may be slightly longer than optimal. The second Stokes model shows the same trend as the first Stokes model.

## 2.6 Laser performance for optimum mirrors

To optimize a first or second Stokes laser, the main free parameters are the reflectivities of the input/output mirror. Using the equations for the power output of first Stokes and second

Stokes lasers, we can calculate what the optimum reflectivities are, and then see how the power output of optimized lasers responds to changes in other parameters.

Consider a first Stokes laser first, whose power output is given by Eq. (2-10). The partial derivative of  $P_{Sout}$  with respect to  $R_P$  and  $R_S$  are

$$\frac{\partial P_{Sout}}{\partial R_P} = \frac{\eta_S l P_{Pinci}(R_S-1) \left( -2 + R_P + \frac{1-R_P}{\sqrt{\frac{g l \gamma P_{Pinci}(R_P-1)}{(1+L_S-R_S)A_1}}} + \sqrt{\frac{g l \gamma P_{Pinci}(R_P-1)}{(1+L_S-R_S)A_1}} \right)}{R_P^2 (R_S-1-L_S) \sqrt{\frac{g l \gamma P_{Pinci}(R_P-1)}{(R_S-1-L_S)A_1}}}, \quad (2-41)$$

$$\frac{\partial P_{Sout}}{\partial S} = \frac{\eta_S}{R_P} \left( - \frac{P_{Pinci}(R_P-1)(R_S-1) \left( \sqrt{\frac{g l \gamma P_{Pinci}(R_P-1)}{(R_S-1-L_S)A_1}} - 1 \right)}{(1+L_S-R_S)^2 \sqrt{\frac{g l \gamma P_{Pinci}(R_P-1)}{(R_S-1-L_S)A_1}}} - \frac{\left( R_P - L_P R_P - \left( \sqrt{\frac{g l \gamma P_{Pinci}(R_P-1)}{(R_S-1-L_S)A_1}} - 1 \right)^2 \right) A_1}{g l \gamma} \right). \quad (2-42)$$

Setting  $\frac{\partial P_{Sout}}{\partial R_P} = \frac{\partial P_{Sout}}{\partial R_S} = 0$  to find the maximum power point, we obtain the optimum  $R_P$  and  $R_S$  as

$$R_{S-optimum} = 1 + L_S - \sqrt{\frac{L_S g l \gamma P_{Pinci0}}{L_P A_1}}, \quad (2-43)$$

$$R_{P-optimum} = 1 - \frac{L_P}{L_S} \sqrt{\frac{L_S g l \gamma P_{Pinci0}}{L_P A_1}}. \quad (2-44)$$

Note that here we use the approximation  $\ln(1/x) \approx 1 - x$  and so the optimum equations are valid in low pump power range.

For the second Stokes laser, we can in the same way use the power equation Eq. (2-29), and set  $\frac{\partial P_{SSout}}{\partial R_P} = \frac{\partial P_{SSout}}{\partial R_S} = 0$  to find the optimal reflectivities as

$$R_{SS-optimum} = 1 + L_{SS} + \frac{A_1 L_P}{A_2 \lambda} - \frac{g l (A_1 L_P + A_2 \lambda L_{SS}) \gamma P_{Pinci0}}{\sqrt{A_2^2 g l \lambda^2 (A_1 L_P + A_2 \lambda L_{SS}) \gamma P_{Pinci0} (1 + L_S - R_S)}}, \quad (2-45)$$

$$R_{P-optimum} = 1 - \frac{A_2 g l \lambda (A_1 L_P + A_2 \lambda L_{SS}) \gamma P_{Pinci0}}{A_1 \sqrt{A_2^2 g l \lambda^2 (A_1 L_P + A_2 \lambda L_{SS}) \gamma P_{Pinci0} (1 + L_S - R_S)}}, \quad (2-46)$$

where  $\lambda = \frac{\lambda_{SS}}{\lambda_P}$ .

For the further analysis of the optimum equation, we study a sequence of lasers with waist radii from 10  $\mu\text{m}$  to 50  $\mu\text{m}$  and plot their optimum reflectivities ( $R_P$ - $R_S$  graph) as a function of loss and pump power.

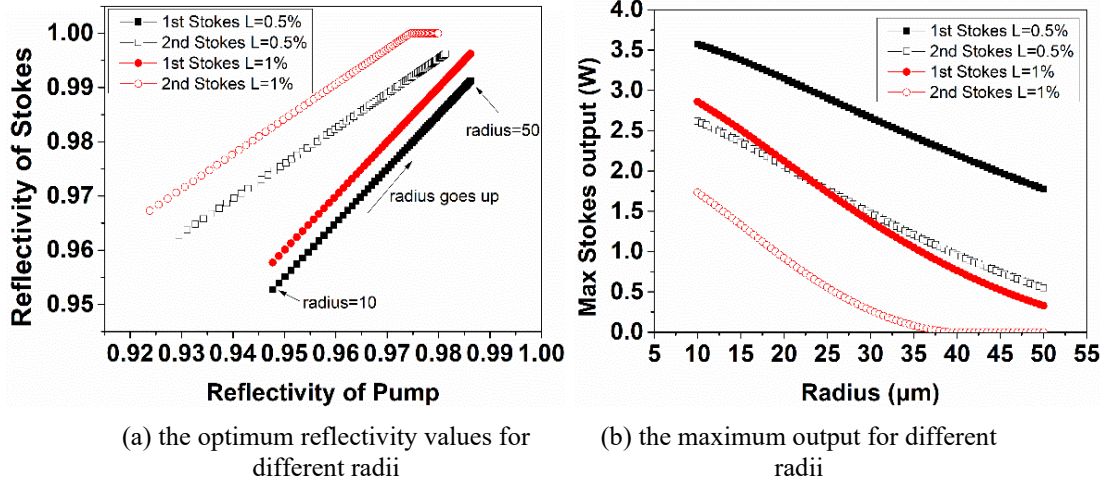


Figure 2-12 Reflectivities for maximum power (a) and the maximum Stokes/second-Stokes power (b) for pump power=5 W. The hollow symbol is for the second Stokes while the solid symbol is for the first Stokes. From left bottom ( $r=10 \mu\text{m}$ ) to right up ( $r=50 \mu\text{m}$ ) with the step of  $0.5 \mu\text{m}$

Figure 2-12 shows the optimum reflectivities (a) and corresponding maximum output power for lasers with different waist radii and different losses. Note that there are several spots  $R_{SS} = 1$  and zero second-Stokes output power as the loss and radius are too big and the laser cannot reach threshold. When the radius goes up, the span of the reflectivity becomes narrower. For the 1<sup>st</sup> Stokes lasers, the  $R_P : R_S$  slope is close to 1 meaning they change together, while for 2<sup>nd</sup> Stokes lasers the  $R_P : R_{SS}$  slope is higher, meaning that  $R_P$  changes more rapidly than  $R_{SS}$ . Decreasing loss appears to affect mainly the optimum  $R_S/R_{SS}$  reflectivity, and does not affect the slope.



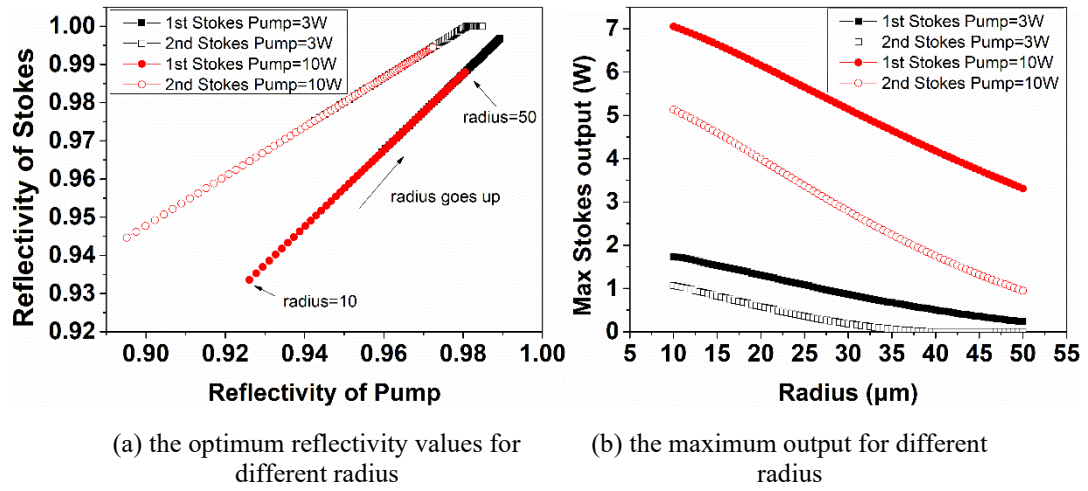


Figure 2-13 Reflectivities for maximum output power (a) and the maximum Stokes/second-Stokes power (b) for loss=0.75%. The hollow symbols are for second-Stokes lasers while the solid symbols are for first Stokes lasers. From left bottom ( $r=10 \mu\text{m}$ ) to right up ( $r=50 \mu\text{m}$ ) with the span of  $0.5 \mu\text{m}$ .

Figure 2-13 show the reflectivities for maximum output power (a) and the maximum power output (b) for different waist radii and different pump powers.

To give an overview of the power scaling for first Stokes and second Stokes lasers, we plot in Figure 2-14 the optimum reflectivities and their optimum Stokes/second Stokes output powers for different maximum pump powers from 1 W to 10 W. Note that Figure 2-14b is the maximum output power for different optimized lasers as a function of maximum available pump power (not a power-in vs power out graph). As Figure 2-14 shows, for smaller pump lasers, the cavity needs more resonance to get best performance, and as the available pump input increase, the optimum output coupler and input coupler decrease. Figure 2-14b shows the maximum Stokes output. We can see when the available pump power is 10 W, we can get 69.88% and 51.82% conversion efficiency for the 1<sup>st</sup> Stokes and 2<sup>nd</sup> Stokes lasers respectively. The difference is caused by the passive loss: if the passive loss is zero, the cavity reaches to the ideal conversion efficiency of the ratio of input to output wavelengths.

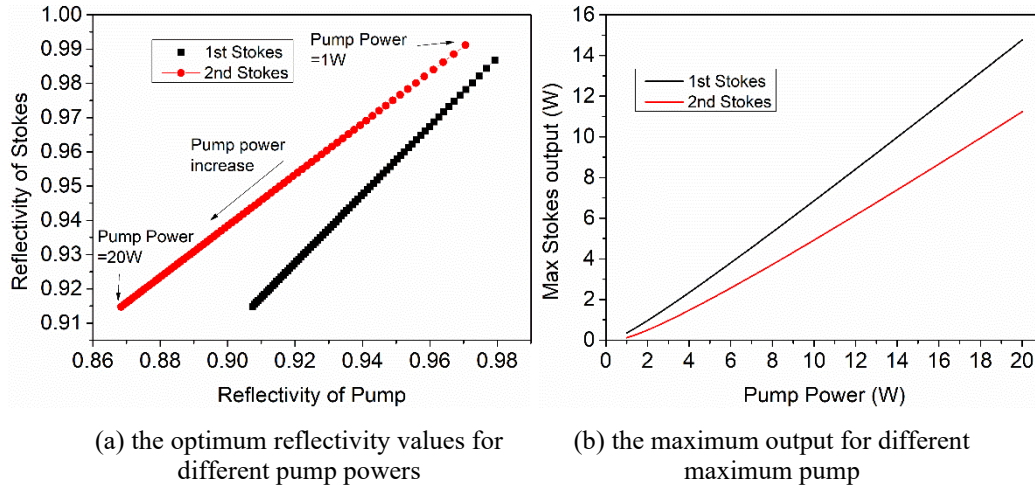


Figure 2-14 Reflectivities for optimised power output (a) and that optimised Stokes/second Stokes output power (b) for different maximum pump power for loss=0.75%, radius=25  $\mu\text{m}$ . Note that in (a) and (b) each point is a different laser, optimised for a specific pump power. From upper right side (Pump=1 W) to bottom left side (Pump=10 W) with the span of 0.25 W.

Finally, we compare predicted output powers from our cavity-enhanced models with models for external cavity Raman lasers (ECRL) in which the pump is not resonated.

Figure 2-15 shows the required pump powers as a function of the designed output power, for optimized first and second Stokes lasers, for both pump-enhanced designs and ECRL designs [18]. We use the same focusing conditions, same crystal parameters, and same losses for both models, and each point on the graphs represents the performance of a laser optimized for that output power. Note that we set  $\gamma = 0.9$  in the pump resonant model to try to make a fair comparison to ECRL, which do not have this mode matching condition. This comparison may be too kind to the ECRL though, since experimental ECRL lasers do not tend to deplete their pump beam fully as the ECRL modelling predicts [77].

As expected, the pump resonant Raman lasers gain significant advantages for low output powers where their reduced threshold due to pump enhancement is a big factor. However, the pump resonant Raman lasers perform much better than ECRLs even for 40 W output powers.

Figure 2-15b shows the optimum reflectivity for the output Stokes in each laser. As the ECRL needs a brighter Stokes field to deplete the pump field in just a double pass through

the crystal, the optimum  $R_S$  is much higher than for the pump resonant laser. Therefore, the fraction of Stokes power lost to passive losses is far more for the ECRL, which means that the pump resonant lasers, even with  $\gamma$  set to 0.9, still outperform the ECRLs. For 2<sup>nd</sup> Stokes ECRL, the first Stokes field must still be resonated strongly to deplete the pump; the gain for the second Stokes is high in these conditions which means the second Stokes has a low  $R_{SS}$ . The ECRL model provides more details [80].

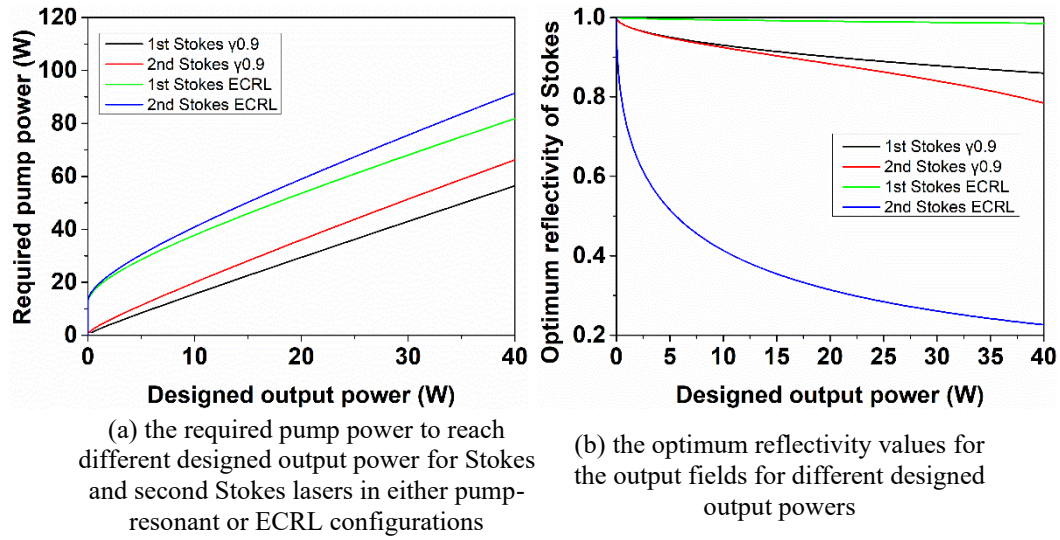


Figure 2-15 The required pump power (a) and optimum reflectivity (b) of the output fields as a function of the designed output power for the pump resonant model and external cavity Raman laser (ECRL) model.

It is concluded that resonating the pump has advantages beyond simply reducing the laser threshold, and the resonant design may be worthwhile even for pump powers at which ECRLs designs would be far above threshold. Also, for SLM operation, active cavity stabilization is likely required, and so we may as well also enhance the pump. However, pump resonant lasers are more complex, so ECRLs may be the best design where wavelength stability and efficiency are not the most important specifications.

## 2.7 The arbitrary order Stokes model

In principle, we can cascade the Raman conversion in the cavity to third or higher orders, keeping the cavity high  $Q$  for intermediate Stokes orders, and outputting the desired  $k$ 'th Stokes order. Using the same basic derivation method, we can develop equations describing



the behavior of arbitrary Stokes order. We use subscript 0 to represent the pump field, 1 for first Stokes, 2 for second Stokes, and so forth.

One finds that the behavior of lasers designed to output odd order Stokes is different to those designed for even order Stokes. The derived the equation for odd order stokes Eq. (2-47) is:

$$P_{kout} = \frac{(1-R_k)}{l} \left( \frac{1}{g_0} \ln \left( \frac{R_0}{e^{L_0} \left( 1 - \sqrt{\frac{(R_0-1)g_1 l P_{0inci}}{A_1 \ln \left( \prod_{j=1}^{(k+1)/2} \left( (R_{2j-1}(1-L_{2j-1}))^{\frac{g_1}{g_{2j-1} A_1} \prod_{i=1}^j \frac{A_{2i-1}}{A_{2i-2}}} \right)} \right)}} \right)} \right) + \right. \\ \left. \sum_{j=0}^{(k-1)/2} \left( \frac{B_j \ln(R_{2j}(1-L_{2j}))}{g_{2j}} \prod_{i=1}^j \frac{A_{2i}}{A_{2i-1}} \right) \prod_{i=1}^{(k+1)/2} \frac{A_{2i-1}}{A_{2i-2}} \right) \quad (2-47)$$

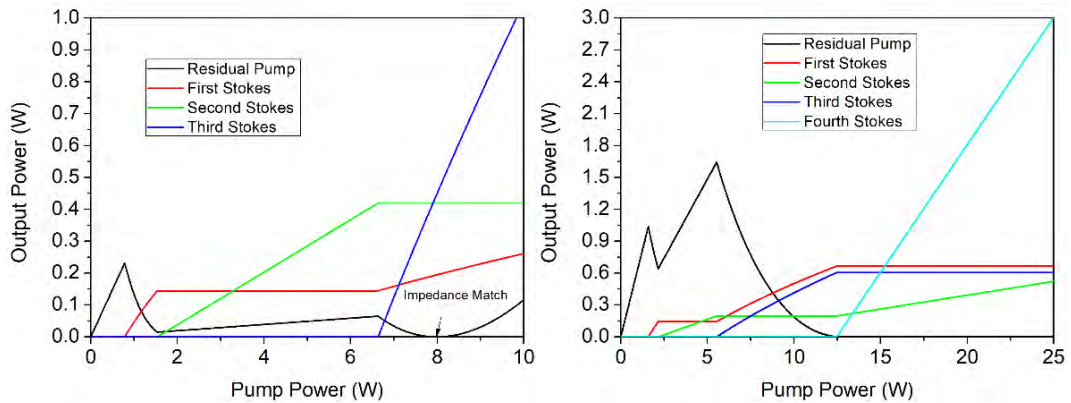
The derived equation for even order Stokes Eq. (5-2) is:

$$P_{kout} = \left( \frac{(1-R_p) l P_{0inci}}{\left( 1 - \sqrt{R_p (e^{-L_0} \prod_{j=1}^{k/2} \left( (R_{2j}(1-L_{2j}))^{\frac{g_0}{g_{2j} A_1} \prod_{i=1}^j \frac{A_{2i}}{A_{2i-1}}} \right)} \right)} \right)^2 + \right. \\ \left. \sum_{j=1}^{k/2} \left( \frac{\ln(R_{2j-1}(1-L_{2j-1}))}{g_{2j-1}} \prod_{i=1}^{j/2} \frac{A_{2i-1}}{A_{2i-2}} \right) \frac{(1-R_k)}{l} \prod_{i=1}^{k/2} \frac{A_{2i}}{A_{2i-1}} \right) \quad (2-48)$$

Figure 2-16 shows the behavior of a third Stokes laser (Figure 2-16a) and a fourth Stokes laser (Figure 2-16b) using realistic numbers for mirror reflectivity and losses. Note that here we assume the mode matching coefficient  $\gamma$  equal to 100%.

First, we consider the model results for the third Stokes laser. The equation for power output (Eq. (2-47)) is reminiscent of that for the first Stokes, with a nonlinear dependence on pump power. Therefore, for odd Stokes output, the even fields are clamped and the odd fields increase with pump power. That means that first Stokes increases with pump power and so  $G$  changes. Similarly to the first Stokes laser then, in odd-order Stokes lasers, there is pump power for which the laser can meet the impedance matching condition for a given mirror set.

Second, we describe the model output for the fourth Stokes laser. Eq. (2-48) for even-order Stokes output looks like that for the second Stokes with output linear with pump power. That means the first Stokes is clamped and so  $G$  is fixed. Thus, for all even-order Stokes lasers, as in the second Stokes case, the laser can be impedance matched for all pump powers above this even-order Stokes threshold. For this even-order output, the odd Stokes fields are clamped and the even fields increase with pump and the laser remains impedance matched for all pump powers above the final threshold.



(a) Third Stokes power output curve

(b) Fourth Stokes power output curve

Figure 2-16 The Stokes output as a function of pump power. The model parameters are:  $L = 1\%$ , pump waist radius =  $20 \mu\text{m}$ ,  $\lambda_p = 851 \text{ nm}$ ,  $\gamma=1$ ,  $R_p=96.67\%$ ,  $R_1 = R_2 = 99.8\%$ , and  $R_3=98.45\%$  in (a) and  $R_3=99.8\%$ ,  $R_4=98.45\%$  in (b).

For higher cascading, the threshold goes up and the total efficiency goes down. In practice, we need to consider the thermal loading as higher order Stokes will lead to higher thermal effects.

## 2.8 Conclusion

In this chapter, we presented modelling for a pump enhanced Raman laser. We present the behaviours of lasers outputting first, second, third, or fourth Stokes output. The model takes into account all experimental parameters, including the quality of mode matching of the pump to the cavity mode.

We explored the effects of parameters in the model, which provides understanding of the ring cavity Raman laser mechanism and guidance for optimization of the lasers. We analyzed the impedance matching condition and showed how impedance matching is different in odd and even Stokes lasers. The optimization analysis shows that the maximum Stokes power occurs at the impedance matched point, and guides our understanding of the regimes that these lasers will be useful in. The pump resonant design has obvious advantages for low power pump lasers. Theoretically, we can make 1 W Stokes and second Stokes lasers with pump powers of just 2 W and 3.2 W respectively. The comparison between the resonant pump Raman laser and ECRL shows however, that the advantages of resonant pump Raman lasers are not limited in the low power regime, but maintain a significant efficiency superiority. In the next chapters, we will use this model to design and optimize experimental lasers to get the best results, and use it to analyze real experimental data.

## 3

## Chapter 3. Continuous wave resonantly pumped diamond Raman laser

In chapter 2, we developed a model to describe the behavior of cavity-enhanced 1<sup>st</sup> and 2<sup>nd</sup> Stokes lasers. This model offers guidance for designing the cavity for optimum Stokes output. In this chapter, we design ring cavities by referring to the theoretical model. We build a ring cavity Raman laser to get 1<sup>st</sup> and 2<sup>nd</sup> Stokes output, characterize the Stokes behavior and verify the model based on the measured data. In addition, we discuss the conditions for single longitudinal mode output.

### 3.1 The experimental design

#### 3.1.1 Cavity design overview

The design of the cavity-enhanced Raman laser was done using our theoretical model (implemented in Mathematica), cavity design software (here we use reZonator), and other software (Solidworks) for physical design.

The high-level design of the SLM Raman laser is shown in Figure 3-1. Identical layout was used first for a laser designed for first Stokes output, and then for a new laser designed for second Stokes output; all that changes is one mirror. The reflectivity spectrum shows the spectrum of the IC/OC mirror for the second Stokes setup.

The pump source was the “SolsTiS” Ti:sapphire laser from M Squared Ltd. The pump beam was mode matched into a ring resonator by a telescope system and a lens. A half-wave plate was included here to control the polarization of the pump field. The ring resonator was designed as a bow-tie cavity with curved input/output coupler (IC/OC) mirror (M1) and three HR mirrors (M2, M3, and M4). The details of these resonator mirrors are given in Table 3-1. The resonator length was controlled by a piezo mounted to M2, and pump enhancement was achieved using the Hänsch-Couillaud (‘HC’) locking scheme [97]. Dichroic mirror DM1 reflected the Stokes beams returning to the pump laser into a power meter, and DM2 passed only the pump light into the locking system. To promote unidirectional oscillation of the first and second Stokes fields, HR mirrors were used to reinject one of the two output beams back into the cavity as in [98]; this is discussed below.

The Raman gain medium was a  $5 \times 2 \times 1 \text{ mm}^3$  CVD grown diamond (Element Six Ltd.), installed on a copper holder and placed in the cavity waist (radius of  $\omega_0 = 20 \text{ }\mu\text{m}$ ) between M1 and M2. The diamond was Brewster cut, for propagation along the [110] direction; the Brewster faces were oriented so that p-polarized incident light was aligned with the [111] direction to access the highest Raman gain [108].

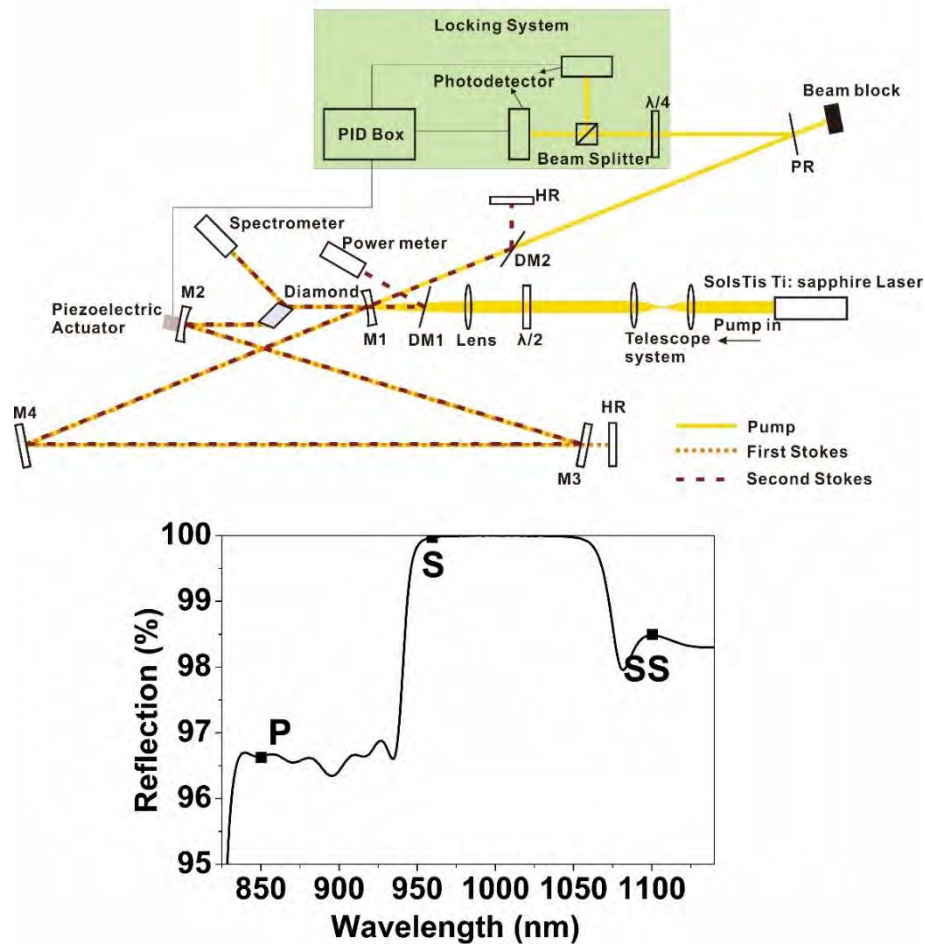


Figure 3-1 Schematic layout of the experimental setup, which could be configured for either first Stokes output, or second Stokes output. For first Stokes operation the IC/OC was 98% reflecting at the pump and Stokes wavelength. The curve below is the spectrum of the IC/OC for the second Stokes setup; the labels P, S, and SS mark the wavelengths of the pump, Stokes and second Stokes fields.

Table 3-1 The details of resonator mirrors. Mirror M1 is different depending on whether we are set up for first Stokes or second Stokes operation

Mirror	Coating	Curvature
M1 (first Stokes)	PR 98±1% at 680-1100 nm PR 96±1% at 840-930 nm	50 mm
M1 (second Stokes)	HR at 945-1060 nm PR 98±1% at 1080-1240 nm	50 mm
M2	HR at 840-1240 nm R = 99.9% at 930-1080 nm	50 mm
M3	HR at 840-930 nm & 1080-1240 nm	Plane
M4	HR at 840-1240 nm	Plane
DM1	Shortpass, edge at 1000 nm	Plane
DM2	Shortpass, edge at 920 nm	Plane

### 3.1.2 Mirror design

The SolsTiS pump laser is a SLM cw Ti:sapphire laser (M Squared Lasers Ltd)., broadly tunable (730-1050 nm) with a linewidth under 50 kHz,  $M^2$  factor less than 1.1, and with 4.5 W maximum output power. Since this power is not sufficient for an external cavity Raman laser to work efficiently, the resonant cavity design is essential to enhance the pump field to achieve enough intensity to drive the SRS process. Considering the flexibility of the cavity and the principle of simplicity - the simpler setup, the more convenient adjustment and more robust performance - we chose the 4-mirror ring cavity. Since we need the rejected pump beam for cavity locking, the 4-mirror system is more convenient than a linear cavity. The bow-tie cavity structure also compensates the astigmatism due to the Brewster crystal. The ring cavity allows us to control the oscillation direction using retro-mirrors as in previous work [98] describing SLM running by controlling the uni-directional operation of the Stokes field inside the cavity.

Mirrors, especially the input/output coupler (IC/OC), are vital for efficient operation. For first Stokes operation, we used a mirror we already had available, which was 98% reflecting across the pump and Stokes wavelength range. The other mirrors were broad-band HR coated to across the pump and Stokes wavelength range, and were off-the-shelf commercial mirrors. For the second-Stokes laser, we designed a new IC/OC mirror (we use the same mirror for pump input and second Stokes output to save paying for two coating runs). The IC/OC mirror coating design was chosen using the modelling in Chapter 2; the core equations are the optimum value equations from Eq. (2-41) to Eq. (2-44). Note that the power curve of the pump laser, the passive loss in the cavity, and the coating precision should be considered into the mirror coating design. The coating design result and the predicted performance of two different purchased mirrors is shown below.

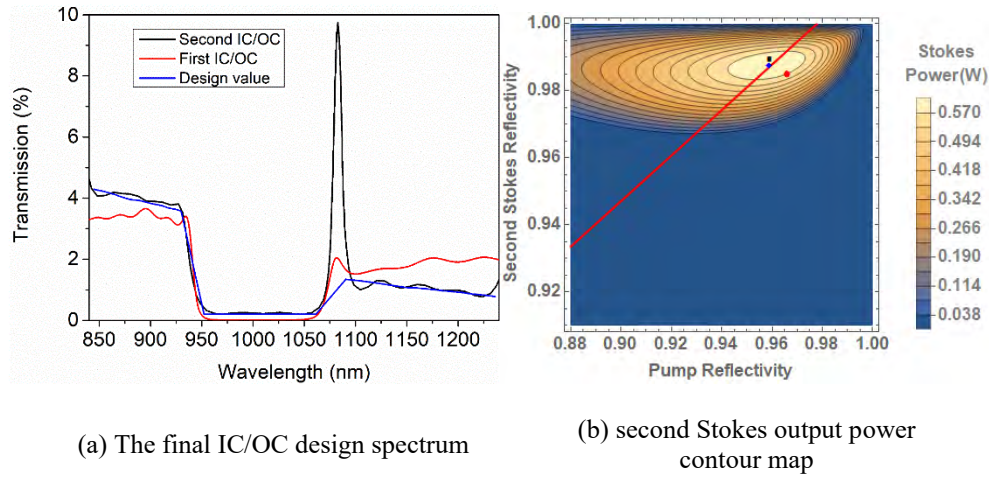


Figure 3-2 (a) The final IC/OC design curve for second Stokes operation, and the measured reflectivities of two purchased mirrors and (b) the modelled second Stokes output power contour map. The blue, red, and black dots mark the design value, and the performance of the first and second purchased mirrors.

As the Figure 3-2a depicts, the blue line is the mirror design value based on a loss value estimated as 0.9%, pump input of 5 W, and radius of 20  $\mu\text{m}$  based on our previous work [98]. We intended to use the tunable pump source to access the pump wavelength from 851 nm to 922 nm, then we could get the first Stokes lasing from 959.8 nm to 1051.1 nm with cavity high Q at these wavelengths, and the second Stokes lasing from 1100.5 nm to 1222.2nm.

The first IC/OC we ordered from Eksma had significant difference to the design values. The reflectivity of the Eksma mirror for the first-Stokes field was HR; however, we do need some transmission at first Stokes to be able to reinject one direction to make the Stokes unidirectional. As a result, we had to set the retro mirror after M3, which was an imperfect HR mirror with 0.1% broadband transmission.

The second IC/OC from Laseroptik was very close to the final design value. We added a small transmission in the Stokes band to allow for strong reinjection using this mirror. We also added a slope to the pump and second Stokes bands to allow for the decrease in output power of the SolsTiS as it is tuned to longer wavelengths. Unfortunately, we did not build the ring cavity using this IC/OC since the SolsTiS pump laser was no longer operating at that time this mirror was available.



The contour figure (Figure 3-2b) shows the predicted second Stokes output as a function of the pump reflectivity and the second Stokes reflectivity, based on our experimentally-available pump power of 4.04 W at 851 nm. The blue dot is the design value, which is the optimum second Stokes output of 612.8 mW; the red dot is the Eksma IC/OC, (used in experiments) and the black dot is the Laseroptik IC/OC (unfortunately not used in experiments). This predicts an output power at 851 nm of 609.8 mW.

The cavity was designed using the software ‘reZonator’, which use the ABCD ray matrices to calculate intracavity beam profiles. It is convenient to investigate the dependence of the cavity mode on different cavity parameters. As the cavity is symmetrical, we can model half the cavity as Figure 3-3a shows. Note that here M5 is a virtual mirror mid-way between M3 and M4 in Figure 3-1 and M7 is a virtual mirror at the midpoint of the crystal, M6 represents mirror M1 or M2; while L2 is the half of the distance between M1 and M2, and L1 is the half of the length of the rest loop (M2-M3-M4-M1). Figure 3-3b shows the beam size as the function location in the cavity (from L1 to L2 and to Cr1). The inset shows the beam shape at the center of the crystal. Due to the Brewster angle crystal, the beam inside the crystal has an ellipse shape with the ratio of the long axis and short axis equal to the refractive index of the crystal.

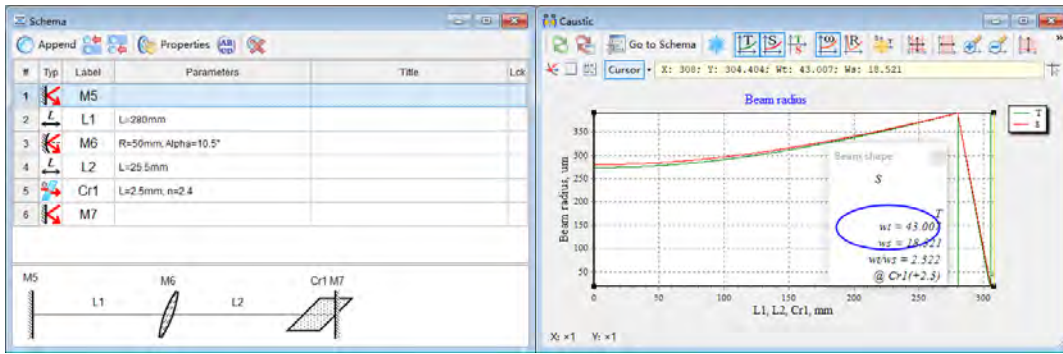
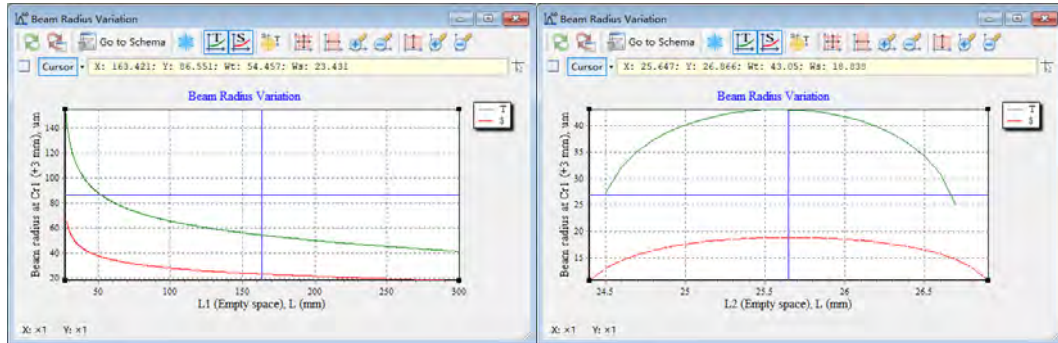
(a) Radius=10 $\mu$ m(b) Radius=40 $\mu$ m

Figure 3-3 the cavity setup (a) and the beam size simulation (b) in reZonator software. The inset of (b) is the beam shape at the center of crystal.

Tuning the cavity lengths L1 and L2 changes the waist size in the crystal. From the model in Chapter 2 we know the smaller waist size can get better performance. However, we need enough physical space between mirrors to fit the diamond and mounts, and therefore we

choose  $ROC=50$  mm curvature mirrors which gives a waist size of  $20\text{ }\mu\text{m}$  with L2 in the middle of the stability range, as Figure 3-4b shows. Comparing the two pictures in Figure 3-4, L1 is less sensitive than L2, which means L2 needs critical adjustment.



(a) L1 change

(b) L2 change

Figure 3-4 the waist size change as the function of L1 (a) and L2(b)

The angle of the curved folding mirrors is selected to compensate the astigmatism caused by the Brewster angled crystal: for the 5 mm diamond crystal, and mirrors with  $ROC=50$  mm, the required angle is  $10.5$  degree. Note that the stability diagram for sagittal and tangential planes is then symmetric as the Figure 3-4b shows.

The pump beam must be mode matched using a telescope, and injected through the IC/OC mirror to match the intracavity mode as closely as possible. In principle, the IC/OC mirror can be any of the four cavity mirrors, but which it affects the cavity alignment and operation. If the IC/OC is one of the flat mirrors, the input beam will be incident from the long arm L1 first, which can make the mode matching easier as the beam size in the L1 part is large and collimated; it is also sometimes possible to find flat mirrors with suitable coating from the supplier's stock. However, the pump beam's angle through the crystal and the precise location the beam enters the diamond will then be affected by cavity alignment, which makes cavity alignment more complex. We really want to separately optimize the crystal angle and beam location, and so it is better to have the pump beam couple into the cavity through the curved mirror to directly fix the pump beam angle and its entry point to the diamond.

### 3.1.3 Locking system design

The pump resonance scheme needs a locking system to control the cavity length to match the pump resonance condition. The locking system uses a piezo to drive one mirror to adjust the cavity length. The common locking strategies are Hänsch-Couillaud (HC) locking [97] and Pound-Drever-Hall (PDH) [109] locking.

#### HC locking

We will mainly use HC locking in our experiments. Figure 3-5 shows the scheme of HC locking to couple a beam to a cavity containing a rotated polarizer. In our case, the Brewster cut crystal in the cavity acts as the linear polarizer, while even with a straight crystal, stress induced birefringence in the crystal can split the resonances of the two cavity polarizations.

The laser incident into the cavity has the amplitude of  $E^{(i)}$ , which can be divided into the components parallel and perpendicular with the transmission axis of the polarizer oriented at angle  $\theta$

$$E_{\parallel}^{(i)} = E^{(i)} \cos \theta, E_{\perp}^{(i)} = E^{(i)} \sin \theta, \quad (3-1)$$

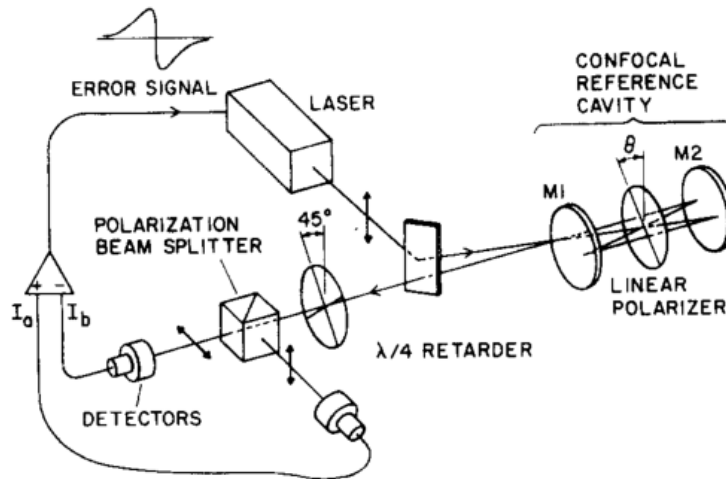


Figure 3-5 the HC locking scheme [97]

The parallel component sees a cavity of low loss. The immediate reflection off M1 interferes with the superposition of beams exiting M1 after undergoing different numbers of round trips, which causes a frequency-dependent phase shift of that resultant reflected beam. The reflected perpendicular component is simply just reflected by the M1 mirror since this component the cavity is blocked by the polarizer. The complex amplitude of the reflected wave of  $E_{\parallel}^{(r)}$  and  $E_{\perp}^{(r)}$  can be calculated as

$$E_{\parallel}^{(r)} = E_{\parallel}^{(i)} \left[ \sqrt{R_1} - \frac{T_1 R}{\sqrt{R_1}} \frac{\cos\delta - R + i \sin\delta}{(1-R)^2 + 4R \sin^2(0.5\delta)} \right], \quad (3-2)$$

and

$$E_{\perp}^{(r)} = E_{\perp}^{(i)} \sqrt{R_1}, \quad (3-3)$$

where  $R_1$  and  $T_1$  are the reflectivity and transmissivity of the mirror M1, and  $R < 1$  is the amplitude ratio between successive roundtrips.  $R$  can include any attenuation by the intracavity polarizer and other losses.  $\delta$  is the phase change per roundtrip, which depends on the exact cavity length. The cavity finesse  $\mathcal{F}$  is related to  $R$  as

$$\mathcal{F} = \pi \sqrt{R} (1 - R). \quad (3-4)$$

$E_{\parallel}^{(r)}$  combines with  $E_{\perp}^{(r)}$  (here we call it the combined beam), which in general has an elliptical polarization, which can be analyzed using a  $\lambda/4$  waveplate and polarising beam splitter, where the two separate beams with different intensity  $I_1$  and  $I_2$  will be detected by two photodetectors (PDs). If the cavity is resonant, which means  $\delta = 2m\pi$ , the  $E_{\parallel}^{(r)}$  experience the cavity as empty, and the combined beam remains linearly polarized as the phase shift is zero:  $I_1$  and  $I_2$  are equal and the error signal is zero. Equally, far from resonance  $E_{\parallel}^{(r)}$  performs the same as  $E_{\perp}^{(r)}$ , and the combined beam is again linearly polarized and the error signal is zero. Between these extremes, the beam is elliptical, with the sense of ellipticity dependent on which side of lock we are on. The ‘error’ intensity signal can be described as follows

$$I_1 - I_2 = I^{(i)} 2 \cos\theta \sin\theta \frac{T_1 R + \sin\delta}{(1-R)^2 + 4R \sin^2(0.5\delta)}, \quad (3-5)$$

where  $I^{(i)} = 0.5c\epsilon|E^{(i)}|^2$  is the intensity of the incident laser beam. The ideal differential signal is shown in Figure 3-6. We can use a PID controller to lock the cavity length at the zero point between two extrema, which is where the cavity can be exactly resonant.

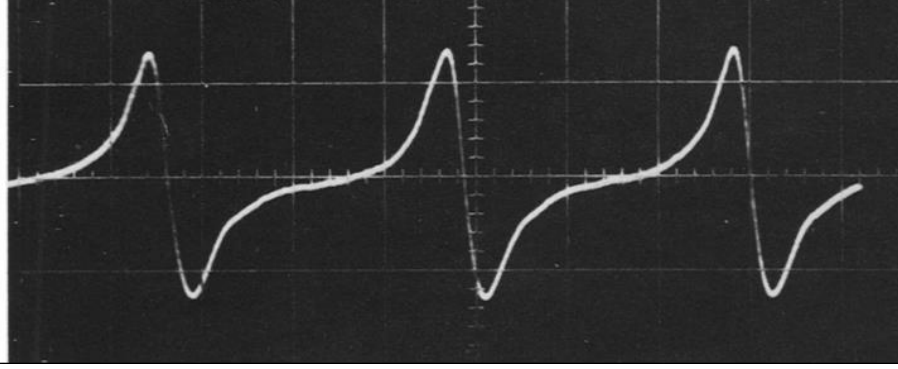


Figure 3-6 the ideal signal change as the function of cavity length [97].

### 3.1.4 Optical component selection

Here we outline the main design considerations for hardware selection. To improve the stability of the ring cavity system, we use short pedestal posts to fix the mirror mounts. The main factor for the mirror mount selection is the adjusters. The 2-adjuster mirror mount is better than the 3-adjuster one, because the extra XY adjuster is not particularly useful in the mirror alignment, but conversely adds extra instability in the system. Another factor is the TPI of the adjuster, which reflects the resolution of the mirror adjustment. The 130 TPI adjuster is suitable after consideration of resolution and cost. We add a translation stage under one of the curved mirrors to allow fine adjustment of cavity length  $L_2$ . After the post and mirror mounts are selected, the optical system height is fixed, and the rest of the components need to fit this height.

For the convenience and accuracy of the alignment, the crystal mount needs at least 5 degrees of freedom. If the beam path direction is named the x direction, the rotation around x axis is not necessary in the alignment, while rotation around the vertical z axis can align the Brewster faces, and rotation around y adjusts the pitch of the crystal. An X-Y-Z translation can move the crystal to find the best region for optimal laser output, and to

optimize the focal position. Here we can use an XYZ translation stage and a kinematic platform mount with 2 adjusters to move the diamond. The diamond holder was made in copper and aluminum.

For the telescope system, the lenses can be adjusted accurately and conveniently using a cage system. If we use the pedestal post to hold the cage system, and calibrate the height of the cage rod, we can use the cage rods to assist the height adjustment of pump laser. By adding two cage apertures at each side of the cage rods, the height and angle of the pump beam is restricted by these two apertures.

After selecting the optical components in the system, it is worth simulating the installation of all component using Solidworks, making use of component models downloaded from the supplier's website (for example, Thorlabs). The simulation helps to find potential problems in the installation like size interference, and can help optimise the layout quickly and conveniently. Figure 3-7 shows the optical layout of the ring cavity system using Solidworks.

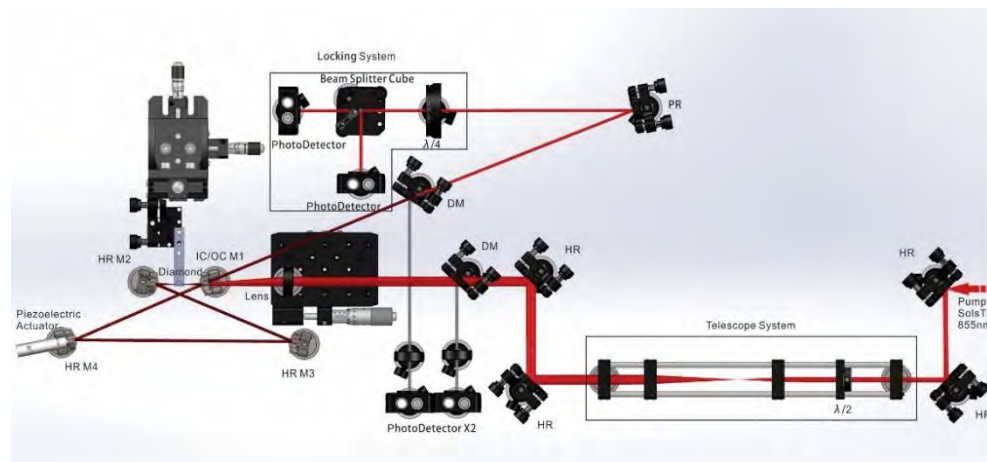


Figure 3-7 Solidworks view of the layout of the ring cavity

## 3.2 Setup installation

### 3.2.1 Note on the cavity installation

We provide here some comments on the cavity installation, and tricks that we found were important.

One perhaps unexpected issue was with the mirror mounts. The retention screw holding the optics in the mirror mount cannot be over tightened, as the resulting pressure induces extra stress in the mirror which we observed to mess up the polarization of the laser fields. As the ring cavity requires the beam polarization to be horizontal, such stress can increase significantly the Brewster loss and compromise the cavity locking stabilization.

The diamond was mounted using a thermal compound containing micronized silver to ensure good contact to conduct heat. The alignment of the Brewster diamond needed strict angle precision. The Fresnel prediction of the reflectivity vs angle (see Figure 3-8) shows the incidence angle from the crystal to air is stricter than the angle from air to the crystal.

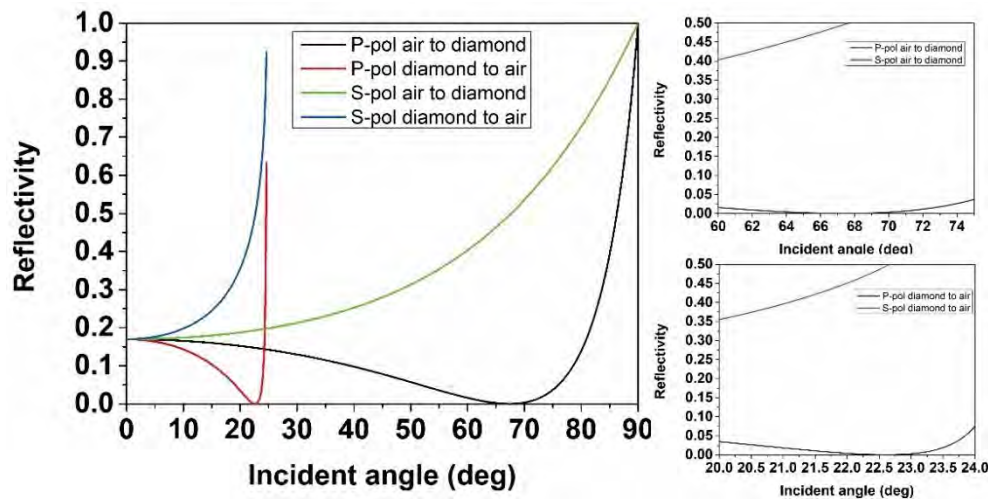


Figure 3-8 The reflectivity changes with the incidence angle from the air to diamond and from the diamond to air. Right two figures are the enlarged view

A triangle fixture with the correct installation angle made the installation more convenient and correct. The holder levelness can be ensured by monitoring the pump beam

position by a CCD camera while loading/unloading the diamond: The beam should be at the same place with/without diamond in.

The key aspect of the locking system installation is that only the pump beam can be incident into the locking system, so an absorption low pass filter should be used to block any Stokes beams. In addition, using a sampling partially reflecting mirror before the locking system to reflect only a portion of the beam power is a good idea as the photodiode detector (PD) only requires low input power. In order to optimize the cavity locking, the intensity of the two PDs needs to be similar when the quarter plate is set at 45 degrees. We used OD filters and diffusers before the sensor of the PDs to control the input intensity and decrease the alignment sensitivity. Note that the amplifier of the locking electronics had a 1 M $\Omega$  input resistance, and we used an additional 200-ohm termination in parallel to achieve a sub-microsecond response time. Note that the beam path of the locking system is related to the alignment of the IC/OC, and so if the IC/OC is moved it is necessary to align the locking system again by tuning the sampling mirror.

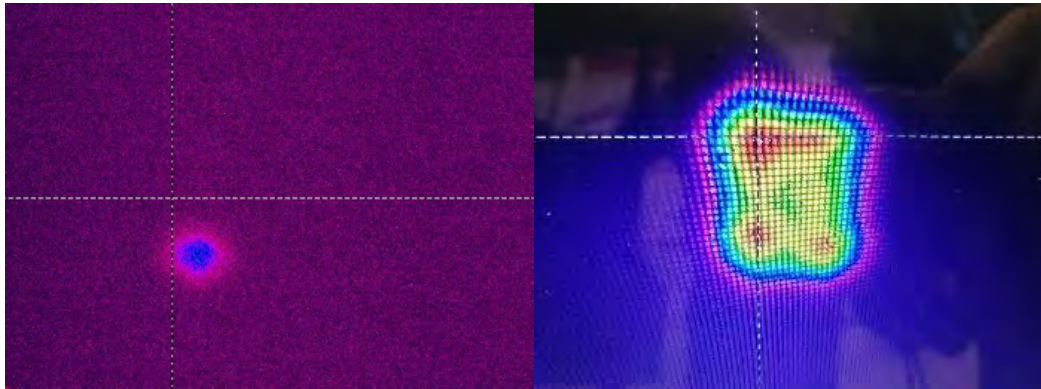
### 3.2.2 Cavity alignment

The pump wavelength for these experiments was at 851 nm, and the invisible wavelength results in some difficulties in the cavity alignment. Therefore, we need the assistance of the laser detector card. As we have a tunable-wavelength pump source, we can firstly tune the pump wavelength to 780 nm, where the mirrors are partially transmitting and we can readily check the leakage beam from each mirror to check the alignment. We align the cavity with the locking box scanning the piezo position, which avoids that flashing that happens in an unscanned unlocked cavity.

The alignment process for the bow-tie cavity is as follow. For description, we call the first beam circulating inside the cavity as the first bouncing beam, and the beam circulating inside the cavity many times as the accumulated beam. The mirrors are labeled as the Figure 3-1 shows.



Firstly, align the ‘transmitted beam’ through M1 around the cavity, and inspect the beam overlap after M1 using the detector card. Then move M1 to overlap the ‘recirculated beam’ with the transmitted beam on the M1 to M2 path. Repeat these two steps until the beams are overlapped completely. Restore the pump wavelength to 851 nm and inspect the leakage beam from the Brewster reflection of diamond, or from the M3 mirror. If two beam spots are found in the field of the camera view, move the two spots to be overlapped, as the Figure 3-9a shows. As alignment get closer, there are more and more spots (more and more roundtrips), which makes the accumulated beam look like a big square shape (Figure 3-9b), and then a single much brighter spot (Figure 3-9c). If the number of beam spots does not increase during the alignment and the intensity does not significantly increase, usually the issue is with the cavity length such that the cavity is not a stable resonator. Another reason for difficulty can be that the recirculating beams get out of the plane of the diamond and are clipped. Note that the pump focusing lens position is very crucial: an out-of-focus pump will make the accumulated beam look like a star shape (Figure 3-9d).



(a) Non-overlapped

(b) Close to overlapped

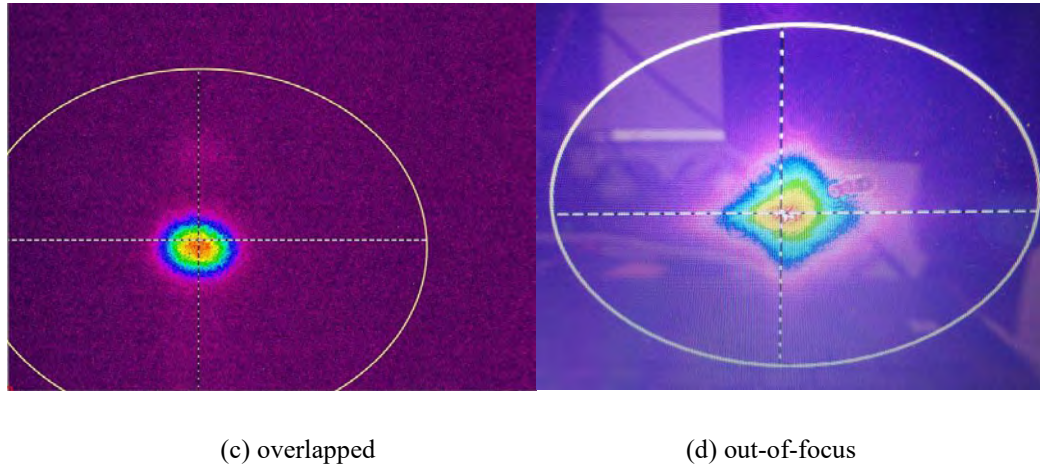


Figure 3-9 The not-overlapped beam spot (a), close to overlapped (b) and overlapped spot (c), spot with out-of-focus pump (d) after M3. Note that the (a) is gain compensated, (c) is exposure time reduced. (b) and (d) are taken separately.

When the cavity alignment is optimised, we use the CCD camera to observe the leakage beam after M3; we can determine the mode matching degree by blocking/unblocking the cavity, and comparing the beam sizes of the single pass pump and the accumulated cavity mode. In the case of ideal mode matching, these should be identical.

### 3.2.3 Stokes alignment

After the pump beam is aligned, the PDs in the locking system will show the signal as the picture shows below. The yellow channel is the reflected pump from the IC/OC, light blue channel is the error signal from the two PDs (the function is PD a minus PD b), and the purple channel is the pump leakage from a HR cavity mirror. The piezo is being scanned here, so the dip in the yellow trace is the cavity scanning through resonance, showing an error signal on the blue trace, and a peak in the intracavity intensity on the purple trace. If there are multiple valleys in the yellow signal in each scanned free-spectral range, that means pump power is coupling to higher transverse modes as well as  $TEM_{00}$ , and we need to optimize the mode matching and cavity alignment to minimize these superfluous valleys.

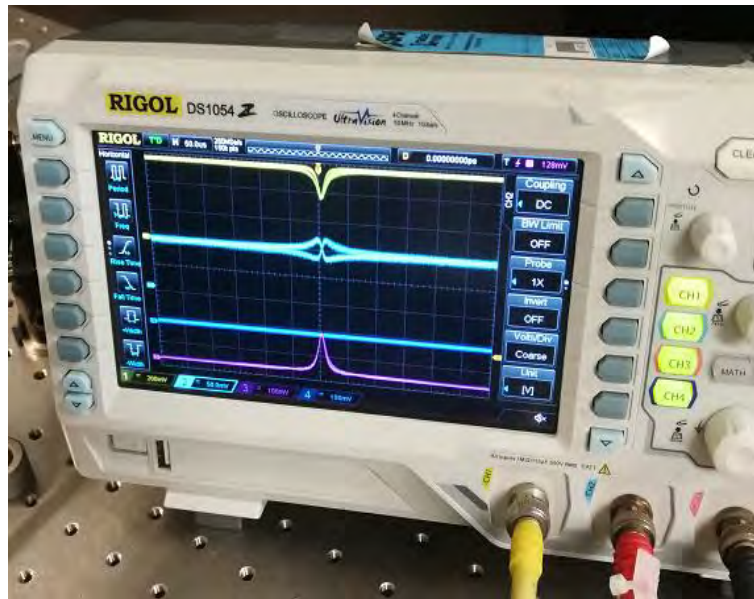


Figure 3-10 The signal from the locking box when in scanning mode. Yellow channel is the reflection pump signal from the IC/OC, light blue channel is the error signal from two PDs, the purple channel is the pump leakage from the cavity.

The next step is to do the fine tuning of the mirrors to get the valley part of the yellow channel as deep as possible; the deeper the drop in reflected signal, the more pump power is being coupled into the cavity. The way to do the fine tuning is walk the mirror adjustments using opposite pairs. Usually, M1 and M4, or M2 and M3. As the sagittal plane and the tangential plane are independent, we can align the X direction and Y direction separately. One of the effective alignment strategies is the scan-step method. More specifically, step an adjuster at first (e.g., X adjuster of M2), then scan its pair adjuster (X adjuster of M3) until the valley part of yellow channel is deepest. Then step the stepped adjuster in the same direction, and scan the paired adjuster again to find the extremum. Compare these two deepest levels: if the latter one is deeper, then repeat the step to explore the deeper value. Otherwise, the direction of the step adjuster is wrong, and we need to reverse the direction of the adjuster and do the step-scan again. Sometimes walking different pairs, M1-M2 or M3-M4 pairs can also work well. We also need to search different positions of pump focusing lens that also plays a key role in the pump beam coupling. Overall, any adjustment that deepens the valley is good!

Once the alignment is close, we can increase the power of the pump laser and look for Stokes lasing. Stokes lasing can be detected by a spectrometer looking at the weak reflection off the diamond Brewster face. If possible, set the pump power to at least double the expected threshold of the laser setup. If lasing is not observed, try to translate the diamond around; limited by the diamond growing conditions, the diamond crystal is not uniform, and the birefringence strength vary. Experimentally, we observe that some areas of the diamond perform significantly better lasing than others.

In Table 3-2 below we show a checklist of the possible reasons that might prevent Stokes lasing after careful alignment.

Table 3-2 checklist of the possible problems

cavity	cavity alignment	Pump source	wavelength
	mode match		power
	waist radius		beam shape
	lens position		stability
	focus position	others	the PD/spectrum is out of battery
	cavity length		the PD/spectrum is misaligned
mirror	mirror is installed in reversed		part of beam is clipping a mirror mount/holder
	mirror is fixed too tightly		the scanning channel has the multiple valleys
	the mirror is not clean		The beam is propagating incorrectly though the diamond Brewster faces
diamond	the position		
	the yaw angle		
	the pitch angle		
	damage or dirt		

When we have observed Stokes lasing, we put a PD at the output path to monitor the signal strength of the Stokes. The Stokes power is a good reference for optimization, repeating the steps above. With increasingly good alignment, and maximizing the pump power, we find the second Stokes lasing.

Experimentally, we find that the Stokes (and second Stokes) naturally lase in both direction around the ring. There are thus two Stokes output beams from the IC/OC, which

should be very closely overlapped with the incoming and rejected pump beams. We wish to reinject the forward Stokes into the cavity to make the Stokes field lase predominantly backwards. We installed a dichroic mirror in the Stokes output that is overlapped with the rejected pump beam to divide the Stokes and pump field, and use another HR broadband mirror to feed back the Stokes field. The reinjected Stokes fields should be roughly mode-matched back into the cavity to best ensure unidirectional operation. This can be achieved by using  $f$  system to collimate the output or  $4f$  system to re-image the waist back into diamond, as illustrated in Figure 3-11.

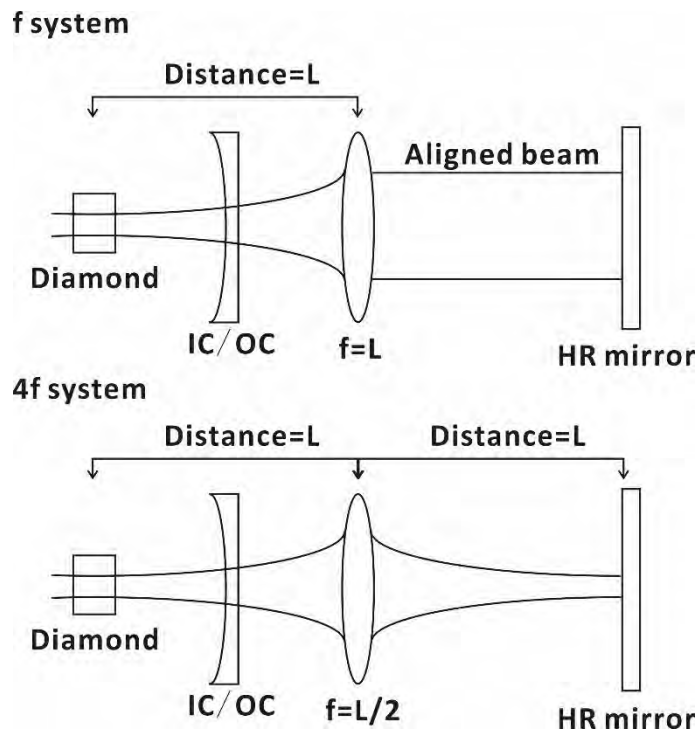


Figure 3-11  $f$  system and  $4f$  system to achieve the mode matched retroreflection of the Stokes fields.

### 3.2.4 Locking alignment

Before cavity locking, the scanning signal should meet the requirements as follows: the PD input signal needs to have low noise and no extra feathers to ensure the PID locking box can lock to the zero of the error signal (as Figure 3-10 depicts); the valley of the PD input signal needs to be as low as possible indicating that most of the pump light can be coupled into the resonator; the error signal needs to be symmetrical, which means the intensity on each PD

is similar. A larger error signal is best, which can be achieved by inducing more vertical polarization using the half plate before the cavity, at the cost of pump power available to couple into the cavity.

We share a tuning strategy that we use to optimize the parameters of the PID locking. We increase the Integral gain until the laser locks, and then increase the Proportional (P) gain to stabilize the laser power; too much P gain will make the PD signal show fast sine oscillation. The last step is to tune the set point (voltage level) up and down to lock the PD signal at the lowest valley level. We can also align the cavity finely to help to improve the locking condition. A good tuning result is shown as Figure 3-12. The PD signal is suppressed at the lowest valley level, while the error signal is controlled at the zero point. It is worth noting that the PID gain settings are not repeatable even in the same setup, likely due to the drift of the alignment of the locking system, and so the PID gain settings need to be readjusted daily.

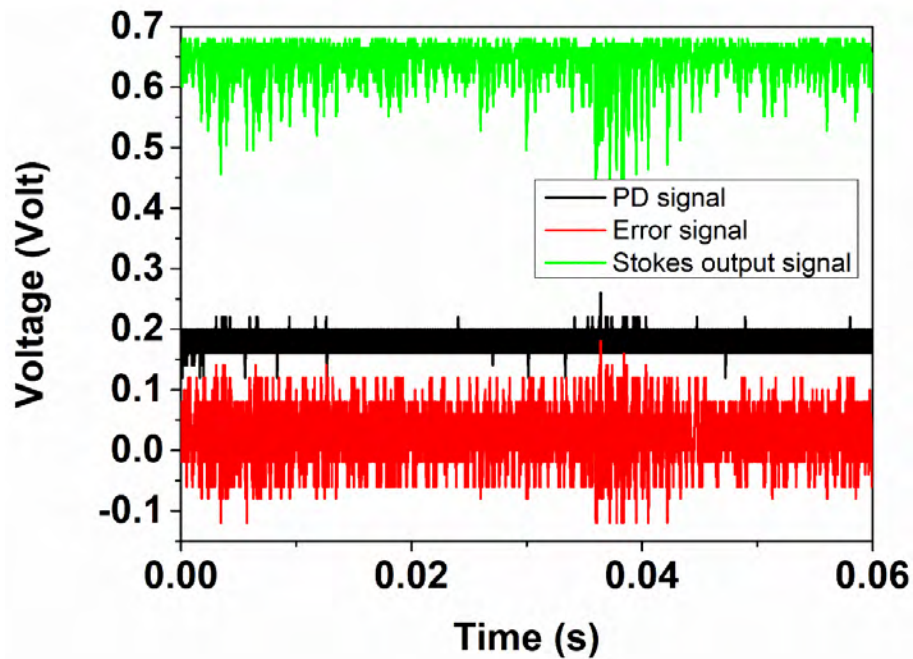


Figure 3-12 the PD signal, error signal and the Stokes output signal when the cavity is locked.

We initially found that the Stokes output was not cleanly locked with the Stokes power dipping sometimes to zero, as Figure 3-13 shows. When we inspected the input voltage to the piezo, as shown in Figure 3-13, discrete voltage steps can be seen, showing that the



digitization of the voltage output from the PID box to the piezo was not fine enough. We solved this by inserting a 1:10 voltage divider at the voltage output port of the locking box, making the box drive an output voltage 10 times larger and the digitization steps after the divider 10 times smaller; The Stokes output becomes more stable, as Figure 3-12 shows.

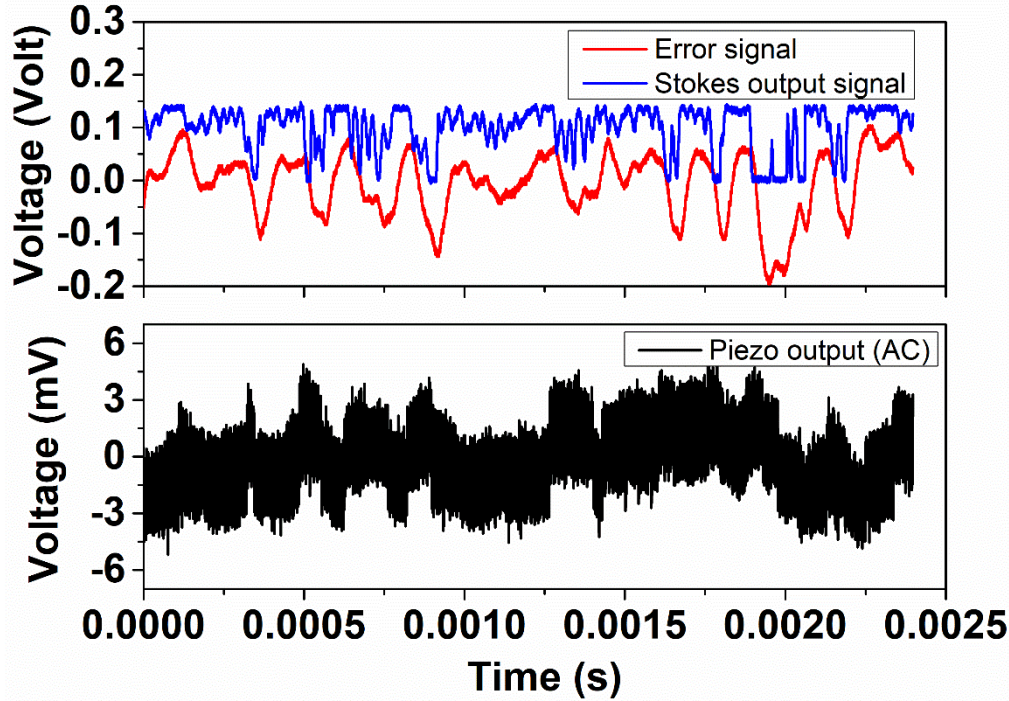


Figure 3-13 Monitor signals with the laser locked, showing the AC-coupled piezo output voltage, error signal and the second Stokes signal with the laser locked, before installation of a voltage divider for the piezo output.

## 3.3 Results and discussion

### 3.3.1 First Stokes generation

Here we present results of first and second-Stokes lasers. First, we configured the laser to generate first Stokes unidirectional output as in [98], but here we improve our understanding of that laser by measuring the rejected pump power. The layout is shown in Figure 3-14. We use mirror M3 as IC/OC mirror with a reflectivity of 98% for both pump and Stokes wavelengths. We reinject the forward-Stokes lasing utilizing a feedback HR mirror, and the Stokes output is then backwards towards the pump laser. Note that the Raman gain

bandwidth (22.5 GHz) is very much larger than the cavity mode spacing (0.5 GHz), and so there is no need to control the cavity free spectral range to ensure resonance of all lasing fields which is in contrast to Brillouin lasers that have very narrow gain bandwidth [110]. As the IC/OC is plane mirror, the cavity is long arm incident type.

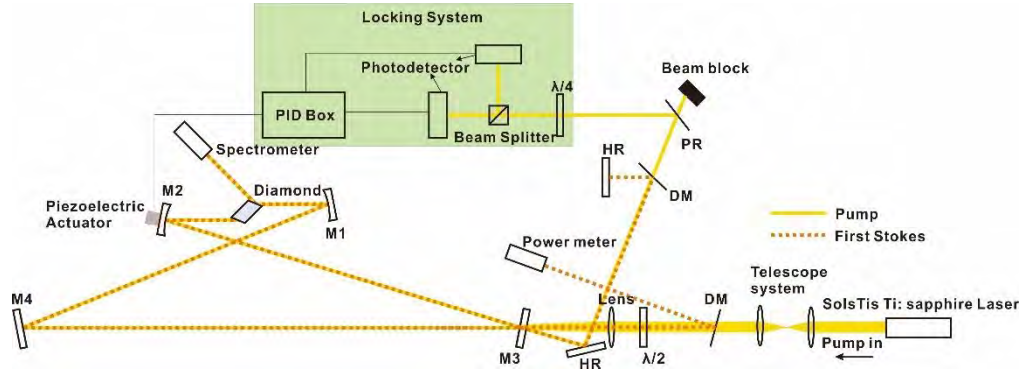


Figure 3-14 Schematic layout of the 1<sup>st</sup> Stokes experimental setup.

The output power curve is shown in Figure 3-15, and the inset shows the beam profile of the first Stokes output. The first Stokes beam is Gaussian and close to the diffraction limit. Compared to our previous result in [98] we use a different IC/OC with different reflectivity and a different diamond crystal; in the present laser the threshold increased from the previous 1.8 W to 2.9 W, however, the slope efficiency has also increased from 32% to 45%. Thus, the maximum first Stokes output power generated at 964.9 nm was 0.4 W for 3.8 W pump at 855 nm with the maximum conversion efficiency 10.4% (see the right axis). The first Stokes spectrum was a stable SLM at all output powers in accordance with our previous work [98] (measured by a scanning Fabry-Perot interferometer (FPI) with an FSR of 10 GHz and resolution 67 MHz).

These results are published in [111]. At the time of the publication, we were modelling the laser without accounting for mismatched pump power, and we were not measuring the rejected pump power. Thus in the modelling for that paper we were assuming  $\gamma$  equal to 1. We input all measured properties of the laser into the model: a gain coefficient of 14.4 cm/GW at 960 nm,  $M^2$  of the fields set to 1, and a pump waist radius of 20  $\mu\text{m}$  (in the sagittal plane, the model accounts for the Brewster angle of the crystal). We assumed that losses were equal for both fields, and that the pump and Stokes beams had identical confocal



parameter, which is valid in a doubly resonant cavity and determines the Stokes waist size to be  $21.3\ \mu\text{m}$  (in the sagittal plane as above). With these parameters, the passive loss value which best matches the data was 1.7%, which is quite high, and seemed like an over-estimate. This fit is shown in Figure 3-15

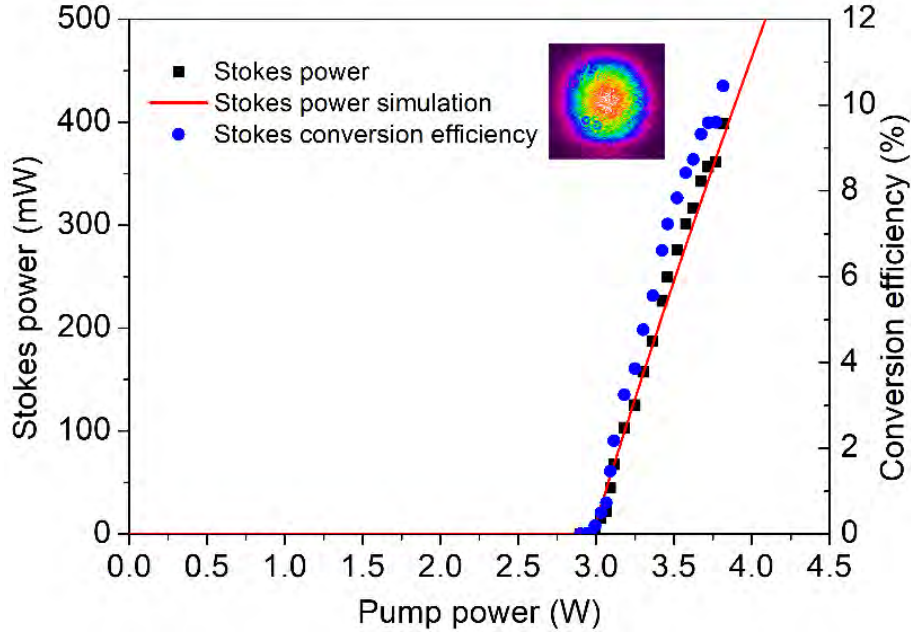


Figure 3-15 Measured (squares) and modeled (solid line) Stokes output power (left axis) and conversion efficiency (right axis) as a function of incident pump power. Inset is the beam profile of the first Stokes beam.

After this result was published, we realized the importance of modelling mismatched pump power correctly using  $\gamma$ . We remeasured the first-Stokes performance while also monitoring the rejected pump power (these results are yet to be published), shown in Figure 3-16. The Stokes starts lasing at 2.31 W and reaches the maximum power of 0.61 W for 3.42 W pump at 851 nm with the maximum conversion efficiency of 17.95% and slope efficiency 55%. Compared to the last measurement, we think that we better optimized the alignment and locking strategy, and minimized the environmental noise to get tighter locking. With the model, we also fit for  $\gamma$  and look for good agreement with the Stokes data as well as now with the data for rejected pump power. We find best agreement for passive loss of 1.2% for both fields and a pump mode-matching fraction  $\gamma = 0.81$ . The solid gray curve shows the reflection of the matched fraction of the pump power, indicating, that the cavity

becomes impedance matched for 3.75 W of pump power, which is close to the maximum pump power available. This lower loss value seems more correct, since in the previous laser the predicted loss was being overestimated to compensate for our incorrect  $\gamma$  of 1. The good agreement between the experimental and theoretical values gives us confidence now in the model's ability to predict performance of the laser.

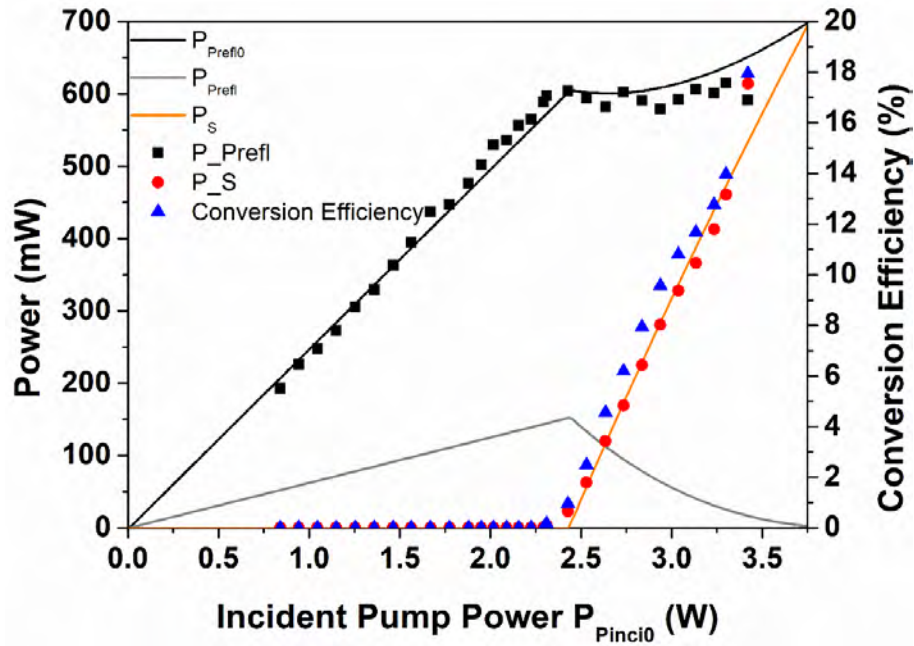


Figure 3-16 Remeasurement of our Stokes laser, showing the reflected pump, Stokes output power and conversion efficiency, along with modeled Stokes  $P_S$ , reflected pump power  $P_{Prefl0}$  (black line) as a function of incident pump power  $P_{Pinci0}$ . Note that the grey line shows the reflection of the mode-matched part  $P_{Prefl}$ .

### 3.3.2 Second Stokes generation

For second Stokes generation the laser was setup according to Figure 3-1. To force the laser to cascade to the second Stokes field, all mirrors were designed to be highly reflecting at the first Stokes wavelength, with the IC/OC mirror M1 (second Stokes) now HR at the first Stokes and designed to couple the pump wavelength in and the second Stokes wavelength out. The mirror design (Figure 3-1 inset) allows some degree of tunability while still having appropriate reflectivity values for each of the three fields. These mirror properties, combined with additional factors of reduced available pump power and slightly-decreasing Raman gain

at longer wavelengths, resulted in the highest second Stokes output power being measured at a wavelength of 1101.3 nm, with a corresponding pump wavelength of 851.5 nm. Second Stokes lasing could be observed between 1100 nm and 1115 nm. A broader tuning range should be possible with optimized mirror parameters.

We characterized the laser at this optimum second Stokes wavelength of 1101.3 nm. Shown in Figure 3-17a, the first and second Stokes reached threshold at 0.9 W and 2.8 W of pump power respectively. The second Stokes output power increased linearly up to 364 mW with a slope of 33.4%, and reached a conversion efficiency of 9.5% at the maximum pump power of 3.86 W. Inset is the beam profile of the second Stokes beam, which shows a Gaussian shape close to the diffraction limit. This laser is also published [111].

Again, we did not have reflected pump data for this laser at the time of publication. Using  $\gamma = 1$ , we fit the results to retrieve a loss parameter of 1.12%, getting reasonable agreement with the experimental results as shown in Figure 3-17(a).

We were not able to repeat the measurement of this second-Stokes laser: irreparable power degradation of the Ti:Sapphire pump laser brought an end to experiments using this pump laser. In the next chapter, we go on to explore another second-Stokes laser using a 1064 nm pump source, including characterizing the reflected pump power.

To try to understand this laser better despite not having the reflected pump data, we model the data using the  $\gamma = 0.81$  value that gave good fits to the first Stokes laser. This gives reasonable fits, with a lower value of the passive loss of 0.93%. Figure 3-18 shows the experimental results with this modelling output, including the predicted reflected pump curve, while the grey line is the reflected power of the matched fraction of the pump power. This modelling suggest that the laser does not operate at the impedance matched condition. Without experimental measurement of the reflected power, it is hard to have confidence in these modelling results.

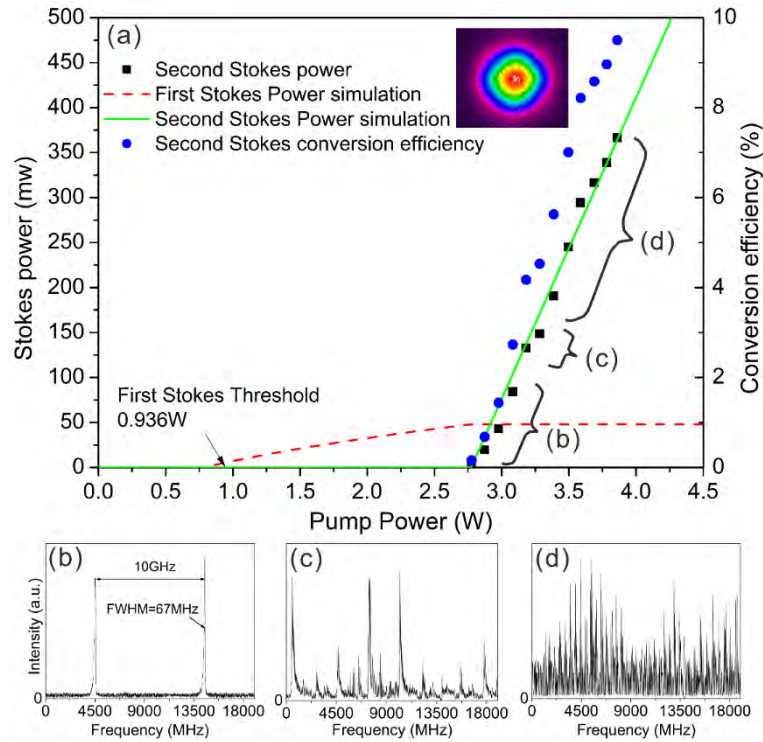


Figure 3-17 (a) Measured and modelled second Stokes output power and conversion efficiency as function of pump power assuming  $\gamma = 1$ . (b)-(d) Output of a scanning FPI monitoring the second Stokes spectra at output powers shown in (a). Inset in (a) is the beam profile of the second Stokes beam.

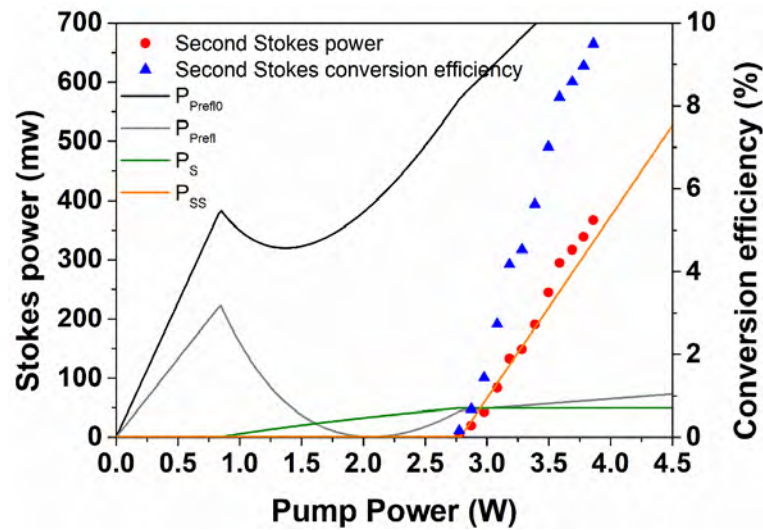


Figure 3-18 Measured and modelled second Stokes output power and conversion efficiency as function of pump power assuming  $\gamma = 0.81$ . Note that the black line is the simulated reflected pump power  $P_{Prefl0}$ , the grey line shows the reflection of the mode-matched part  $P_{Prefl}$ .

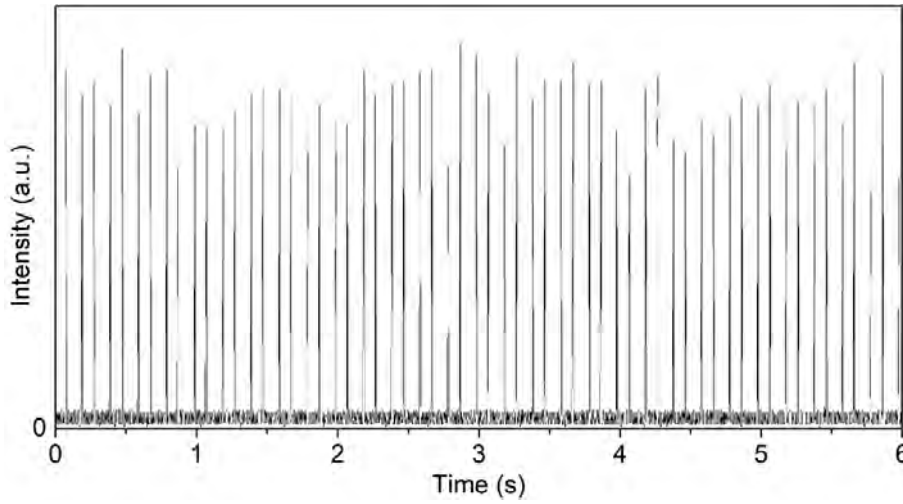


Figure 3-19 Output of a scanning FPI, showing the stability of the second Stokes SLM spectrum.

The second Stokes spectra at different output power levels, as monitored by the FPI, are shown in Figure 3-17 (b)-(d). The FPI frequency-axis was calibrated using the SLM pump source. The second Stokes output was stable SLM (see Figure 3-19) with a resolution limited FWHM of 67 MHz up to about 140 mW of output power. As the power increased above 140 mW, the second Stokes field started to mode-hop and/or oscillate at several modes; above 162 mW, the second Stokes was in a highly multi-mode regime with a range of wavelengths comparable to the free spectral range of the FPI. Interestingly, even at the maximum pump power with multimode second Stokes output, the first Stokes remained stable SLM with only an occasional mode-hop.

The directions of oscillation of the intracavity fields were important in determining the stability of single mode operation. While the cavity enhanced pump field can only travel right to left through the diamond in Figure 3-1, the equal forward and backward Raman gain in principle allows the first and second Stokes field to oscillate in either direction in the ring cavity. As in [98], for the first Stokes laser, reinjection of the left-to-right first Stokes field into the cavity lead to predominantly unidirectional operation, which was necessary to get stable SLM output. For the second Stokes laser, we reinjected the 0.1% first Stokes leakage through the mirror M3, and reinjected the right-to-left second stokes output beam. As a result, the pump and the first Stokes field propagated predominantly in the same direction while the second Stokes field propagated in the opposite direction. We found that choosing counter-

propagating directions for the first Stokes and the second Stokes field increased the maximum SLM output power of the second Stokes. Allowing bidirectional first Stokes operation by blocking its reinjection mirror caused the second Stokes output to be multimode for all output powers. We also investigated the behavior of co-propagating fields by changing the feedback direction of the first Stokes field, resulting in similar multimode operation. We speculate that counter-propagating the interacting fields suppresses the transfer of noise from one field to the next. This can be understood in the time domain as local intensity/phase variations do not stay aligned when fields are counter-propagating as they would for co-propagating fields; in the frequency domain, the same physics is understood by considering that four-wave mixing interactions are not phase matched for counter-propagating fields [112].

For the present design, the first Stokes reinjection was relatively weak due to low transmission of M3 (which was nevertheless the most transmissive mirror at that wavelength, with all mirrors designed to be HR); we measured the power ratio in the two directions to be approximately 3:1. We expect that second Stokes SLM operation will be stable at higher powers by improving the first Stokes unidirectionality - this could be achieved by deliberately designing a larger first Stokes transmission for one of the cavity mirrors. Indeed, this is the reason that we purchased the second custom mirror from LaserOptik described in Fig 2a. Unfortunately, due to failure of the Ti:Sapphire pump laser, we were not able to test these mirrors here.

A sample of the second Stokes power output for a 100 ms time window is shown in Figure 3-20, along with the piezo drive voltage and error signal. The piezo voltage shows a tendency to drift upwards, which we attribute to accumulation of heat in the diamond with an associated change in diamond optical length and so change in the cavity lock position. The fast jump in piezo voltage at the trace centre could be the piezo resetting to the other end of its range. The second Stokes output power shows noise on a 100  $\mu$ s timescale; this could be fast environmental noise, but it is too fast for the piezo to track. Full commercial-style monolithic engineering of the laser design would likely help to fully clamp the second Stokes power.

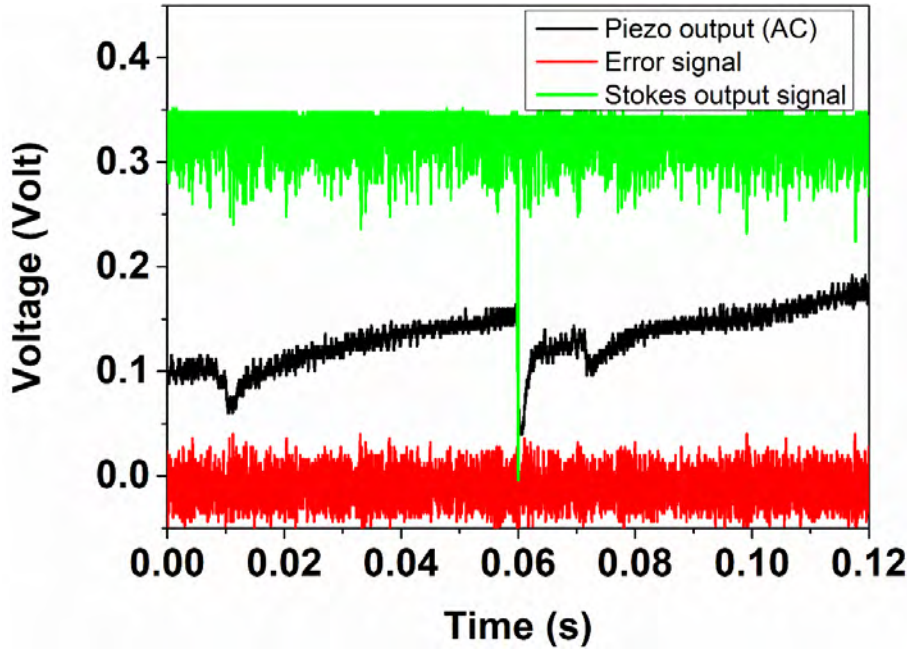


Figure 3-20 the output voltage of piezo, error signal, and the second Stokes signal while locked.

### 3.3.3 Mirror optimization

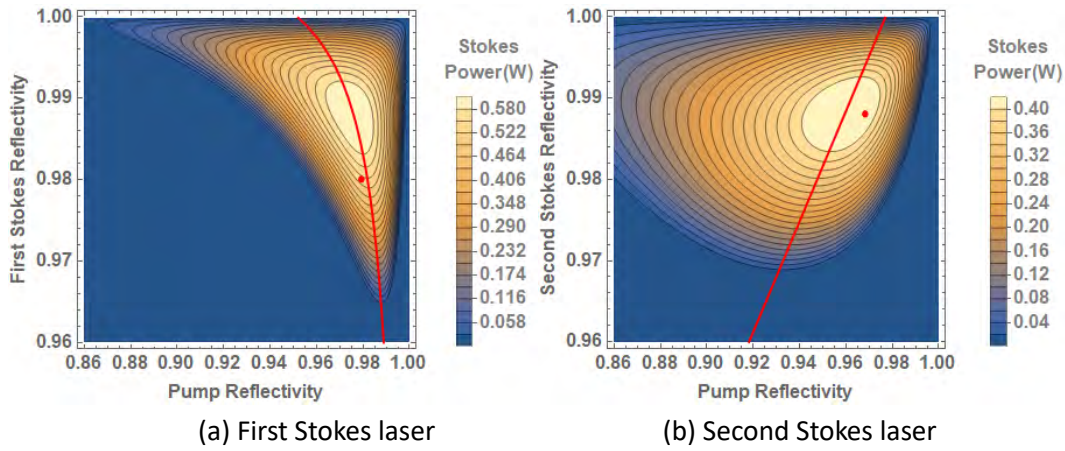


Figure 3-21 The Stokes Power as a function of  $R_P$  and  $R_S$  in (a) and  $R_P$  and  $R_{SS}$  in (b), The parameters are the same as in the experiments, the red line shows the impedance matching condition. The red spot means the position of the experiment setup.

Now when we have fitted losses and  $\gamma$  factors for the first- and second-Stokes lasers, we can consider how close to the optimum possible performance we were in terms of the mirror reflectivities. Figure 3-21 shows the predicted output power for each laser as a function of the input and output mirror reflectivities. The red line shows the parameters that meet the



impedance match condition, while the red dot is the mirror reflectivity in the experiment. For the first-Stokes lasers, as we did not design the cavity to achieve the maximum first Stokes output, the used reflectivity is not close to the optimum. For an optimum mirror we could have generated 624 mW rather than our measured 614 mW. Note that the maximum measured output power in Figure 3-16 is significantly above the value of the modelled line, which predicts 517 mW for that pump power, possibly due to thermal effects altering the cavity parameters.

For the second Stokes setup Figure 3-21b, we see the contours have a similar shape to Figure 3-2b (which assumed 0.93% loss instead of 0.9% loss here), but with lower output power predicted here because of the  $\gamma$  parameter set to 0.81. With an optimised mirror for the same conditions, we could have generated 440 mW of second Stokes rather than our measured 361 mW.

### 3.3.4 PDH locking and HC locking

We saw imperfect locking in our second Stokes laser. We briefly experimented with an alternative locking scheme, PDH locking [109]. The pump beam is modulated to generate two side bands when incident into the cavity. The reflected pump beam consists of a phase-shifted carrier component, and we use a local oscillator to mix it with the reflected pump and generate the error signal which depends on the phase of the response of the rejected beam. The error signal contains the information of how far the pump beam is off resonance with the cavity. In the scanning mode, the error signals are quite similar in both locking methods. However, the error signal of the HC locking (see Figure 3-22a) is much smoother than PDH locking. For the stability of the Stokes, PDH locking seems to achieve more stable Stokes output than HC locking, as the Figure 3-22b shows. However, with the PDH locking, it was more difficult to correctly adjust the PID settings, and seemed to periodically lose lock completely. We suspect that PDH locking is more susceptible to losing lock due to larger cavity perturbations. For these reasons, we continued with the original plan of using HC locking.



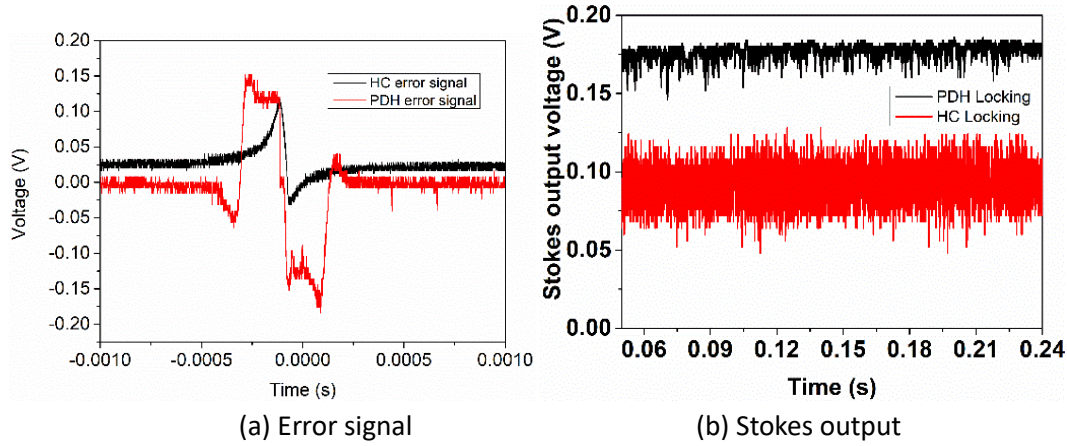


Figure 3-22 (a) The error signals of HC locking and PDH locking in the scanning mode. (b) the second Stokes output signal of HC locking and PDH locking in the locking mode.

### 3.3.5 Locking asymmetry

When the Stokes is lasing, especially the second Stokes lasing, the PD signal (yellow channel) and the second Stokes field (purple channel) in the locking system under the scanning mode is asymmetrical, as Figure 3-23 shows. This asymmetrical signal can be explained due to thermal expansion as the cavity scans through the lock point and lasing action heats the diamond. Oliver Lux investigated this phenomenon in the Ref. [95]. As shown in Figure 3-24, he did a simulation of the PD signal and the Stokes signal under the scanning mode, modelling the increase in optical length of the diamond crystal due to thermal expansion and change in refractive index as it was heated by the lasing action. Our laser shows a similar asymmetry. Figure 3-23 shows monitor signal for the case when we are scanning the cavity length using a triangle wave, longer first and then shorter in this figure. If the cavity is getting longer due to the piezo motion, as we pass through resonance and the laser turns on, the thermal expansion makes the optical cavity length increase faster, and thus pass through the lock point faster. If the cavity is getting shorter due to the piezo motion, the thermal expansion of the diamond makes the optical cavity length decrease more slowly, and thus pass through the lock point slower. This results in the lasing window being longer when scanning to shorter cavities than scanning to longer cavities.

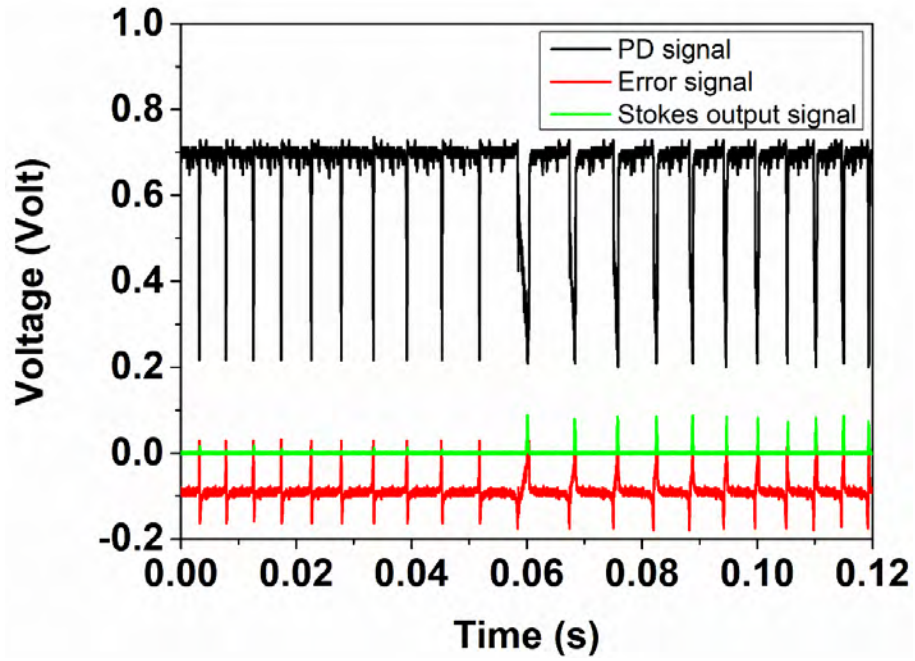
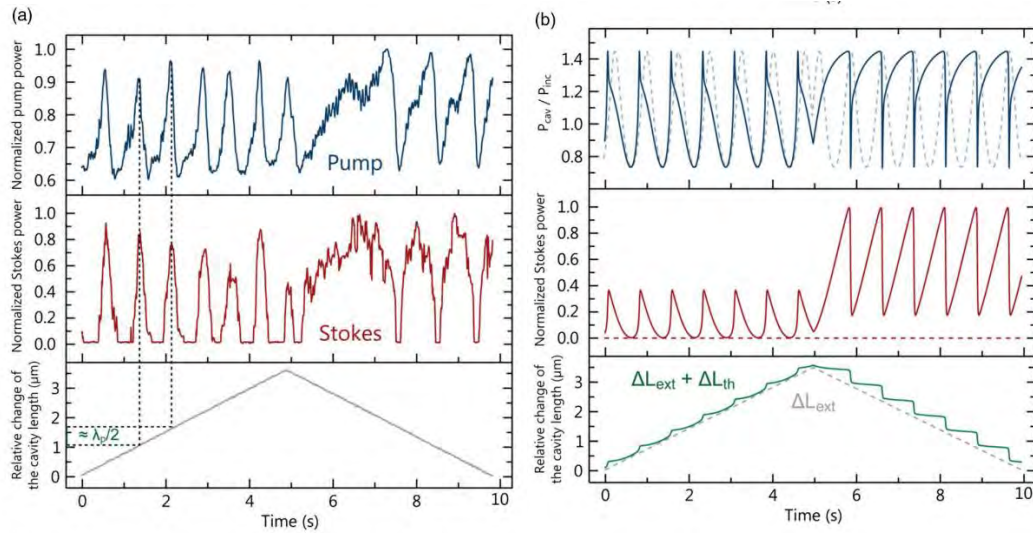


Figure 3-23 The asymmetrical of the PD signal when the Second Stokes fields generates.



(a) Measured power and PZT movement

(b) Simulated power and PZT movement

Figure 3-24 (a) Measured power of the intracavity pump (blue), Stokes power (red) and piezo change as a function of time. (b) a model simulation of the ratio of the intracavity Power and the input pump power (blue), Normalized Stokes power (red) under scanning mode. Where the dashed lines mean the behavior below the Stokes threshold [95].

## 3.4 Conclusion

In conclusion, we have discussed the design and installation process of first and second-Stokes Raman cavity-enhanced ring lasers. We first built a first-Stokes laser to verify the model and investigate the effects of imperfect mode matching. The maximum output of the first Stokes generated at 964.9 nm was 0.4 W for 3.8 W pump at 855 nm with the maximum conversion efficiency of 10.4%.

We then designed and built a second Stokes laser in a triply resonant ring cavity configuration. The maximum output power reached 364.4 mW with 33.4% slope efficiency. The highest stable SLM power achieved was 140 mW. The second Stokes SLM power should be increased by improving the unidirectional operation of the first Stokes. With our current mirrors, the input wavelength of 851.5 nm was converted to 1101.3 nm.

With properly designed mirrors the SLM second Stokes laser can in principle extend the wavelength coverage of the Ti:sapphire pump laser from pump wavelengths of 845-930 nm out to 1090-1236 nm.

## 4

## Chapter 4. Continuous wave resonantly pumped vanadate Raman laser

### 4.1 Introduction

As a well-developed commercial crystal, Yttrium orthovanadate (or vanadate, or  $\text{YVO}_4$ ) is widespread in the laser field. Vanadate has a strong Raman shift at  $890\text{ cm}^{-1}$  with a Raman gain coefficient of  $4.5\text{ cm GW}^{-1}$  [49]. Vanadate has good thermal performance; the thermal expansion coefficient is  $4.43 \times 10^{-6}\text{ K}^{-1}$ , thermal conductivity is  $0.052\text{ W cm}^{-1}\text{ K}^{-1}$ , and  $dn/dT$  is  $3 \times 10^{-6}\text{ K}^{-1}$ . This means vanadate can rank in the forefront of Raman crystals in its thermal performance. Production of vanadate is effective and economic, and we can readily get a customized vanadate with high homogeneity and reliability, making it well-suited to commercial lasers. Of course, diamond is still vastly superior in its thermal properties, has higher Raman gain and a larger Raman shift. However, the production of diamond is still difficult, and diamond processing and coating is still technically challenging. In the state of art, researchers are still working on the uniformity and purity control of diamond crystal, and repeatability between batches can be poor. For these reasons, using a vanadate crystal may be an advantageous and economic alternative to diamond especially for commercial production.

In Chapter 3 we built a ring resonator Raman laser with a Brewster cut diamond as the gain media. In this chapter, we report a ring cavity Raman laser based on vanadate, aiming for second Stokes output so that we get a substantial wavelength shift despite vanadate's

smaller Raman shift. Due to power issues with our SolsTiS Ti:sapphire laser, we use a different pump source now: a 1064 nm cw fiber laser to access up to 60 W pump power. In order to further verify the model, we also build a diamond ring cavity system with this new same pump laser.

## 4.2 Experimental Setup

### 4.2.1 Design overview

The system design is similar to the setup in the Chapter 3, as Figure 4-1 shows. The pump source is the Precilaser 1064 nm fiber laser from Precilaser Co. Ltd. As the pump power is much higher than the SolsTiS Ti:sapphire laser, we deploy an isolator to avoid the backward-propagating beams from the cavity damaging the pump laser.

The cavity is still a bow-tie with M1 as the IC/OC mirror, and M2, M3, and M4 as HR mirrors. The spectrum curve of the M1 is shown in Figure 4-2. Note that the M1 and M2 are curved mirror with 100 mm curvature. The reason to choose this curvature will be discussed later.

We built a vanadate laser and a diamond laser. The vanadate Raman gain medium was  $10 \times 2 \times 2 \text{ mm}^3$  (Castech INC), installed on a copper holder. The vanadate was a-cut, for the polarization direction aligned with the c-axis to access the highest Raman gain. For the diamond laser, the diamond crystal used was the same as the one mentioned in Chapter 3, and the Brewster-cut cavity setup nearly the same as in Figure 1 in Chapter 3. We use a plane-plane vanadate crystal with AR coating for this experiment. Compared to a Brewster cut crystal, this makes the beam alignment easier, and lowers threshold since the beam inside the crystal is not expanded in the Brewster plane and so intensity is higher. Compared to the Brewster diamond, this gives us a 2.4 times advantage in the focal area. However, this advantage cannot compensate the far lower gain of vanadate alone (4.5 cm/GW compared to diamond with 11 cm/GW). However, the longer length of the vanadate combined with the tighter focus does end up predicting the vanadate laser to have higher single pass Raman

gain. The vanadate AR coating can ensure the beam reflection from the crystal surface is relatively small, and tolerance to misalignment is larger than for a Brewster crystal. While HC locking often uses a polarizer in the cavity (which before was the Brewster crystal), the birefringence of the vanadate crystal can split the positions of resonances for horizontal and vertical polarizations. We can still generate an error signal based on the different responses of those polarizations. As a result, the HC locking scheme still works. Due to the absence of the Brewster reflection, we have to position the spectrometer after M2 to monitor the spectrum in the cavity and to get a reference to the cavity alignment. To achieve the unidirectional oscillation of the first Stokes and the second Stokes field, HR mirrors and two kinds of dichroic mirrors are applied. The dichroic mirror DM1 can select out the Stokes beams and DM2 can separate the first Stokes beam and the second Stokes beam. Lens2 is deployed to build an  $f$  imaging system to mode match the retroreflected beam.

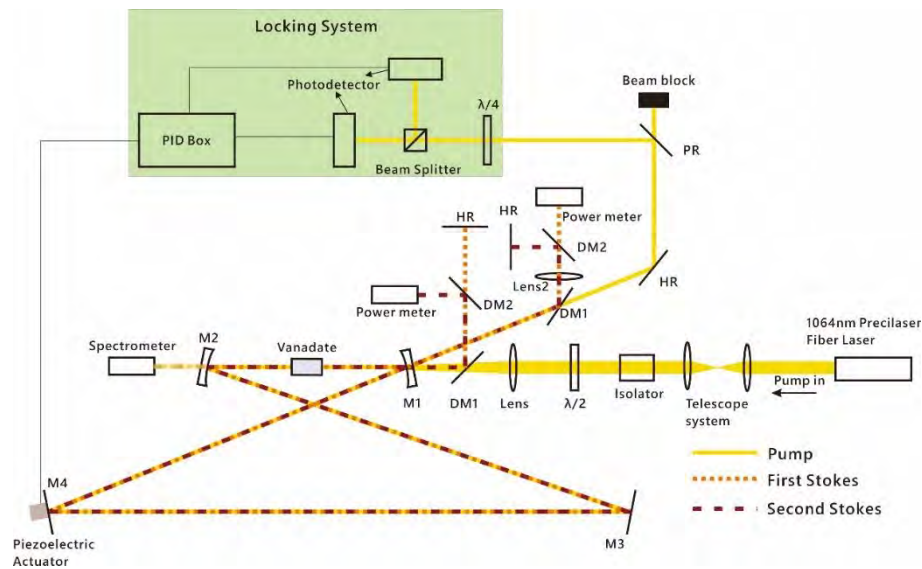


Figure 4-1 Schematic layout of the 1064 nm ring cavity experimental setup.

## 4.2.2 Mirror design

In contrast to designing mirrors for the SolsTis Ti:sapphire laser, in this case for the fixed pump and Stokes wavelengths coating design should be simpler. However, since we wished to use diamond and vanadate in different experiments, we needed to consider the reflectivity at wavelengths at 1064 nm (pump), 1175.3 nm (1<sup>st</sup> Stokes of vanadate), 1240 nm (1<sup>st</sup> Stokes

of diamond), 1312.6 nm (2<sup>nd</sup> Stokes of vanadate), and 1485 nm (2<sup>nd</sup> Stokes of diamond). We also set tighter error margins of the designed wavelength for the precision control of the manufacturer. We designed for a pump power of 5 W; even though we have much more pump power available, as the greatest advantage of the resonant design is at lower pump powers. To get the feedback of the 1<sup>st</sup> Stokes field and achieve unidirectional operation, we set the transmission of the 1<sup>st</sup> Stokes field as 0.2% based on the result of the Chapter 3. Too much transmission of the 1<sup>st</sup> Stokes will make the 2<sup>nd</sup> Stokes of vanadate inefficient, while too little transmission risks not achieving unidirectional operation. That was proven in the 851 nm ring system in Chapter 3. The optimum pump reflectivity would be different for vanadate and diamond: we mainly wanted to investigate the 2<sup>nd</sup> Stokes output of vanadate and so we designed the pump reflectivity for the vanadate laser. Therefore, only vanadate should reach its optimum output. Applying equation from Eq. (2-41) to Eq. (2-44) in Chapter 2, we can obtain an optimum design, assuming  $L=1.1\%$  and a waist radius= 20  $\mu\text{m}$ . The design result is shown below.

Note that here assumed that thermal lensing would be relatively small at a pump power of 5 W, but this turned out not to be the case, and we were not able to use a waist radius for the vanadate ring setup of 20  $\mu\text{m}$ .

Table 4-1 The details of IC/OC mirror (under AOI=11degree).

Center Wavelength	1064	1075.3	1240	1312.6	1485
Range	1040-1090	1150-1195	1220-1260	1290-1330	1460-1510
Reflection	96.75 $\pm$ 0.2%	99.8% $\pm$ 0.1%	99.5% $\pm$ 0.1%	99.53% $\pm$ 0.2%	98.9% $\pm$ 0.1%
Measured value	96.5691%	99.7117%	99.541%	99.5146%	98.9992%
differences	-0.1809%	-0.0883%	-0.041%	-0.0154%	0.0992%

The spectrum of the produced mirror is shown in the Figure 4-2. The measured values at the center wavelengths are also shown in the Table 4-1, showing excellent matching to the design parameters.

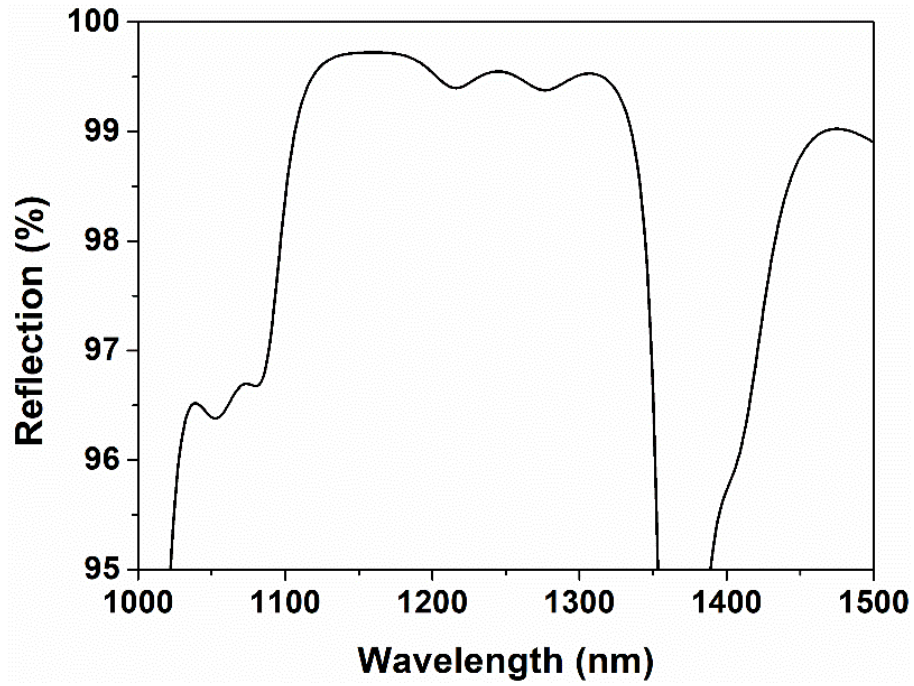


Figure 4-2 the spectrum of the IC/OC mirror for the 1064 nm ring system

### 4.2.3 Thermal lensing management

As the thermal performance of vanadate is good compared to other Raman crystals but still much worse than diamond, we need to consider the possible thermal effect. The most important thermal effect in our cavity is the thermal lens caused by residual absorption. Note that when Stokes is lasing, the SRS process also deposits significant additional heat corresponding to the phonon energy in the crystal. When the laser passes through the crystal, a thermal gradient with a parabolic profile is generated. The thermal gradient results in a refractive index gradient, due to the  $dn/dT$  temperature dependence. The refractive gradient performs as a lens. The thermal lens can distort the beam quality, and affect the stability and cavity mode matching. As a result, the thermally-induced optical cavity length change  $\Delta L_{th} = (\frac{dn}{dT} + n_0\alpha)d$  plays a key role in the cavity stability, with  $d$  the crystal length,  $\alpha$  the expansion coefficient, and  $n_0$  the refraction index of the crystal [95].

For the pump enhancement setup, when resonator length comes close to locking, the pump power inside the cavity will increase, which induces the thermal effects and  $\Delta L_{th}$



changes. That thermal cavity length change can make the locking dynamic. More specifically, the piezo moving in and out has an asymmetric effect to the cavity length when it moves from the locking point. If cavity moves to be longer, the cooling makes the cavity shorter and this to some degree self-corrects. However, if the cavity moves to be slightly shorter, the collapse of power will further shorten the effective cavity length, so push the cavity further out of lock; this effect can destabilize the locking process. We already saw this effect in diamond above, however, for vanadate the thermal feedback was too strong for the current locking setup to control. As the thermal lens effect change on a sub-ms scale, the piezo and locking cannot keep up. Figure 4-3 shows the PZT attempts to lock the cavity with the strong thermal lens effect in vanadate. A second thermal effect is that thermal lensing can distort the beam shape and beam size, which can cause the mode change and affect the  $\gamma$  value. This is less important than thermal induced cavity length change.

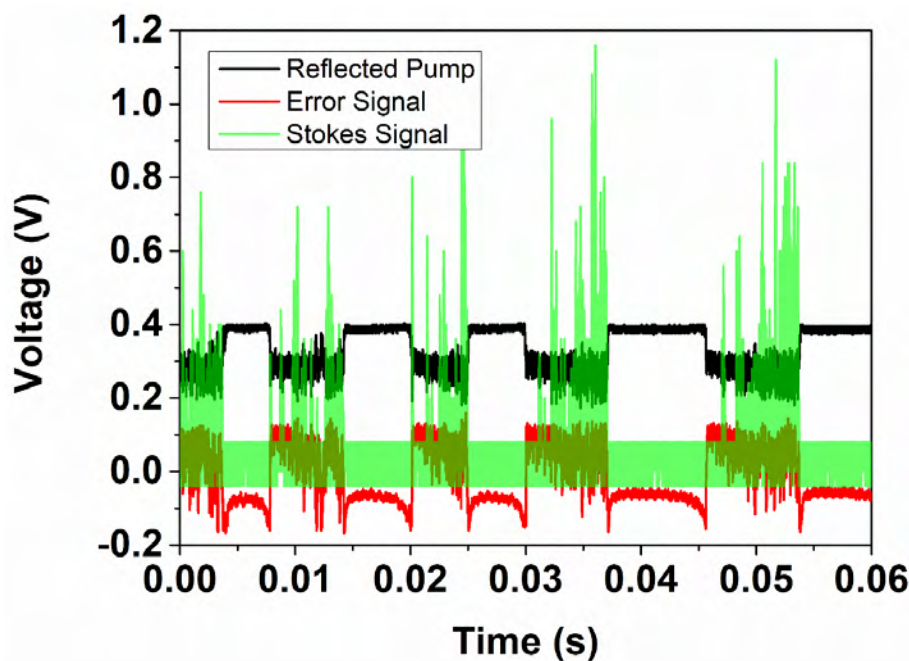
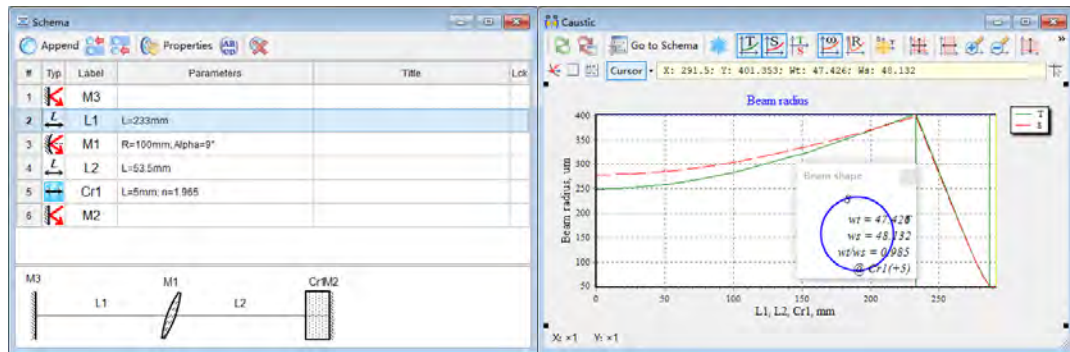


Figure 4-3 The reflected pump, error signal and Stokes signal when laser is locking under 4.2 W pump power

The thermal lens cannot be easily prevented; conventional cooling has no effect since it cannot compensate the thermal gradient. Clearly a crystal with higher thermal conductivity and smaller thermal optical coefficient does lessen the lensing effect, and this is why we see this locking issue with vanadate but not with diamond.

## 4.2.4 Cavity design

In order to attempt to handle the thermal lens in vanadate, we decided to try a larger beam waist size to lessen the thermal lens [113]. This sacrifices the threshold of Stokes but this is not necessarily a problem since we are using a high power pump laser and longer crystal. Use of higher pump power adds more heat but the total thermal lens can still be decreased by the substantially larger beam radius. We used the curved mirror with 100 mm curvature to get a beam waist of  $48\text{ }\mu\text{m}$  (see Figure 4-4). Compared to the diamond laser in the previous chapter with a waist of  $20\text{ }\mu\text{m}$ , we now have: 5.7 times larger beam area, a vanadate crystal twice as long, vanadate gain lower by a factor  $4.5/11$ , and a plane crystal rather than Brewster giving an advantage of 2.4. Overall, we have a single pass gain of about three times lower.



(a) cavity setup

(b) beam size simulation

Figure 4-4 The cavity setup (a) and the beam size simulation (b) in the reZonator, the inset of (b) is the beam shape at the center of crystal.

## 4.3 Result and discussion

### 4.3.1 Stokes Power I/O

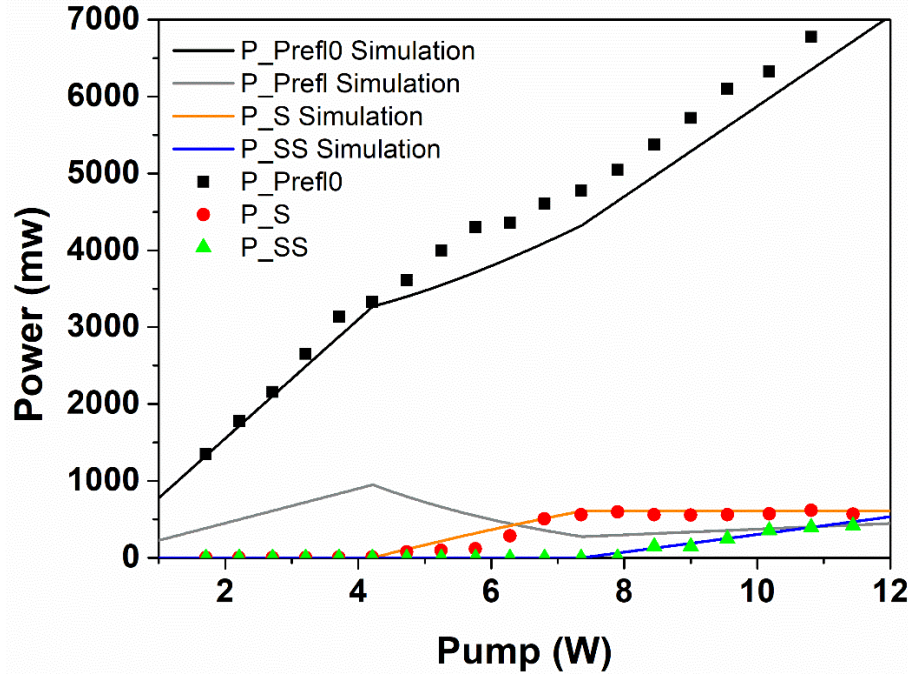


Figure 4-5 Measured power (markers) and simulated values (lines) for the reflected pump  $P_{refl0}$ , first and second Stokes output  $P_S$  and  $P_{SS}$ . Note that the grey line is  $P_{refl}$ , which is the reflected fraction of the matched pump power.

Figure 4-5 is the measured power output (markers) and simulated powers (lines) of reflected pump  $P_{refl0}$ , first Stokes  $P_S$ , and second Stokes fields  $P_{SS}$  with the AR coated vanadate as the Raman gain medium. We obtained first Stokes at above 4.2 W of pump power, and this field is clamped at about 600 mW above the second Stokes threshold of 7.4 W. The second Stokes field reaches its maximum value at 417.5 mW for 11.4 W of pump. The slope efficiency of the second Stokes field is 10.43%.

To fit the model to the measured Stokes output and reflected pump data, we use a gain coefficient of  $g_S = 4.5$  cm/GW, pump waist radius of  $48 \mu\text{m}$  from the ABCD cavity simulations from reZonator, and parameters of the IC/OC mirror are from Table 4-1. We get a good fit for  $L_P = L_S = 0.6\%$  and  $L_{SS} = 0.5\%$ , and with the mode matching parameter  $\gamma =$

0.45, which means the pump available for coupling is less than half. This is significantly worse than the results in Chapter 3 with  $\gamma = 0.81$ , and this was the focus of our optimization. Even so, the model here proves its worth in highlighting this issue and still fitting well the measurements even with the non-ideal mode matching.

We investigated the stability of the power output signal, shown in Figure 4-6. The reflected pump, first Stokes and second Stokes are in cw regime with a lot of noise. The issue of thermal effects causing periodic loss of lock is no longer seen with the larger cavity mode, but clearly the locking system is still not able to perform well. The first Stokes field does not have the fast noise of the pump and second Stokes field. As mentioned above, this relative stabilization of the first Stokes output is likely due to the first Stokes field being clamped when the higher order Stokes is generated. The slower drift of the first Stokes may be due to the evolving thermal lens and changes in intracavity Stokes beam quality. The fast stabilization phenomenon suggests that a small amount of second Stokes power could be useful even in a first Stokes laser for power stabilization.

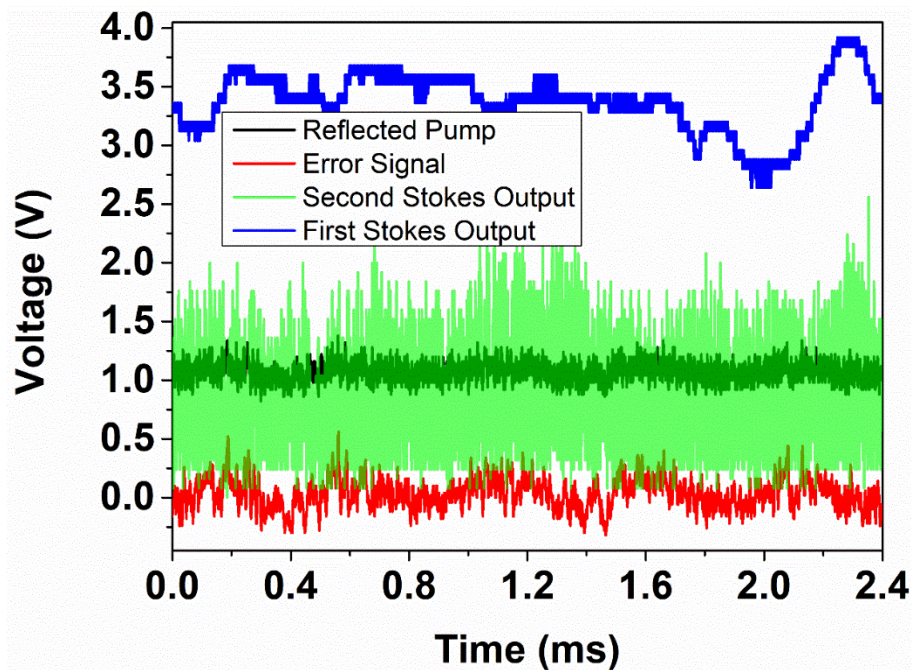


Figure 4-6 The power output signal of the reflected pump, first Stokes field, and second Stokes field as a function of time for a power level of 200 mW of second Stokes power.

### 4.3.2 Pump coupling issue

The modelling above suggested that the  $\gamma$  value was only 0.45 for this laser, which is abnormally low. When in the scanning mode, we also see only a small dip in the reflected pump when we scan through resonance, as seen in Figure 4-7.



Figure 4-7 the reflected pump signal (yellow and blue) in the scanning mode of the piezo

As the problem also appears in scanning mode, it suggests that the low  $\gamma$  is not just a problem of staying correctly in lock. Usually the small dip can be attributed to either bad mode matching, or bad impedance matching, if for example the cavity losses were too high. We firstly considered whether the mode matching was not good. We re-optimized the cavity length and mode matching, but it did not work even when the accumulated beam size was very close to the first input beam. Then we checked the impedance matching. We removed the crystal and inserted an uncoated glass plate with angle adjustable close to Brewster's angle. Based on the impedance match condition ( $R_p = G$ ), when the loss inside the cavity matches the input mirror transmission, the impedance should be perfectly matched. The glass plate allows loss adjustment inside the cavity and we should achieve perfect impedance matching by scanning the angle of the glass plate. However, the pump coupling reached a maximum of only 50%. Since we had already confirmed that the mode matching was as good as we could make it (and we achieved 90% matching with similar optimization in the previous chapter) we were still in need of a different cause for our coupling problem.



We consequently investigated the transmission of the input mirror, the crystal loss, and the polarization in and out of cavity and confirmed everything was normal. Eventually, started to suspect the pump laser itself. Figure 4-8 shows the reflected pump (yellow), error signal (blue), and pump leakage from the M3 (purple) in locking mode at low power (a), far below the threshold of Stokes. The low pump power can eliminate the influence of thermal effects. We see sub microsecond fluctuations on the intracavity pump field when the cavity is locking, however the pump beam stability itself is normal before it arrives at the cavity (c). It turned out to be an issue with the frequency bandwidth of the pump source. The pump exhibits fast fluctuations in the frequency inhibiting the coupling into the cavity. Figure 4-8b shows a zoomed view of the intracavity power in scanning mode as it scans through the cavity resonance, showing fast oscillations on the coupled power.

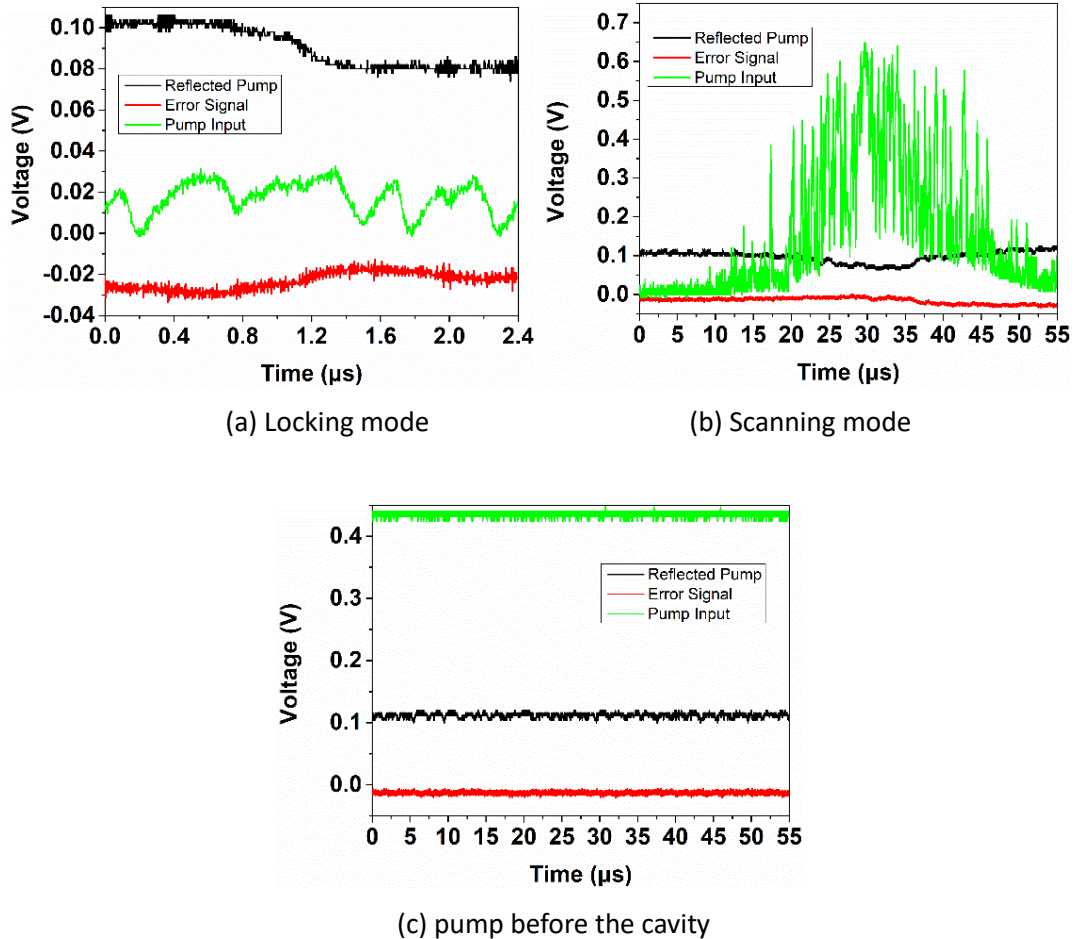


Figure 4-8 The reflected pump, error signal and intracavity pump power (measured by leakage through M3), with the cavity locked (a) and with the piezo scanning (b). In (c) we show laser power sampled before the cavity.

To explain the bandwidth instability, we need to know the linewidth of the cavity. At impedance matching, the cavity behaves like a symmetric etalon with mirror  $R_1$  from IC mirror and  $R_2 = 1 - L$ , where  $L$  is the total loss assumed as 1%. Standard results give the FSR of the cavity and finesse of the cavity as  $FSR = \frac{c}{p} \approx 505.85$  MHz and  $\mathcal{F} = \frac{2\pi}{-\ln(R_1 R_2)} \approx 145.74$ .  $\frac{FSR}{\mathcal{F}}$  gives us the linewidth of the cavity resonance as 3.47 MHz [104,114]. The Topica laser that seeds the pump laser has a nominal linewidth of 5 MHz. This is then consistent with our scanning measurement suggesting that the pump frequency is shifting on a 200 ns timescale over the 5 MHz linewidth, which is broader than the acceptance linewidth of the cavity. The sub-microsecond timescale is too fast to be tracked with a piezo, so we are going to on average only couple in a fraction of the pump. Modelling gives a ‘mode-matching’  $\gamma$  of 0.45, and this is in fact now describing this partial coupling due to the frequency instability, and thus also modelling the degree of average matching of the laser frequency to the cavity frequency.

We have very recently taken initial measurements using a different seed laser with narrower linewidth. However, even with this issue fixed, we found that we still cannot get stable locking, even under the second Stokes threshold. We think that with the better seed laser, the stability is improved, but then the thermal loading of the vanadate crystal and so thermal effects become more serious than before. This appears to prevent stable locking. Designing the IC/OC mirror for a 20  $\mu\text{m}$  waist was sub optimal. Future correct coating design for a larger beam radius may improve the thermal performance. We also consider using longer crystal to distribute the thermal load.

### 4.3.3 Spectrum

We unfortunately did not have a FP with sufficient resolution to resolve the spectrum, and so we observed the spectrum only using a rough measurement. Figure 4-9 is the spectrum measurement of the vanadate-based Stokes output using a spectrometer (Oceanoptics Ltd.) with a resolution of 4.2 nm FWHM. We see two spectral lines in the first Stokes and the second Stokes field. These wavelengths correspond to two Raman shifts of the vanadate

crystal at  $890.8\text{ cm}^{-1}$  and  $815.8\text{ cm}^{-1}$  from pump field ( $1065.7\text{ nm}$ ). The two spectral lines in the second Stokes field ( $1303.56\text{ nm}$  and  $1315.53\text{ nm}$ ) is the same two Raman shifts shifting the brighter the 1<sup>st</sup> Stokes spectral line at  $1178.75\text{ nm}$ . We expect in principle for this laser to only run on the stronger Raman shift ( $890\text{ cm}^{-1}$ ). We speculate the dual Raman shifts may be caused by locking instability so the laser is not reaching its full steady state. If the locking can be more stable, we expect the laser should run on a single wavelength.

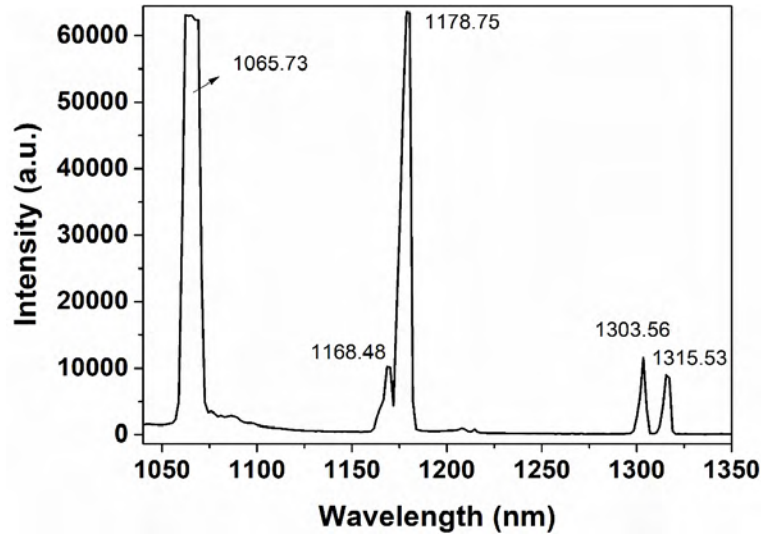


Figure 4-9 Spectrum measurement of the vanadate-based Stokes output by spectrometer.

To further investigate the spectrum of Stokes in vanadate, we used a wavemeter (Bristol Instrument Ltd.) with a resolution of  $2\text{ GHz}$ ,  $0.011\text{ nm}$ . Compared to the cavity FSR  $505\text{ MHz}$ , the Bristol wavemeter cannot distinguish the longitudinal modes in the cavity when Stokes is lasing. Figure 4-10 is the spectrum measurement result by the wavemeter with  $167\text{ mW}$  second Stokes output. We can see some sub-peaks around the main peak for both of the second Stokes lines, which means the vanadate laser is running on multiple longitudinal modes. This is not at all surprising given that the broad pump spectrum was preventing stable locking; fluctuation of all fields as well as the thermal fluctuations can easily destroy the SLM operation.



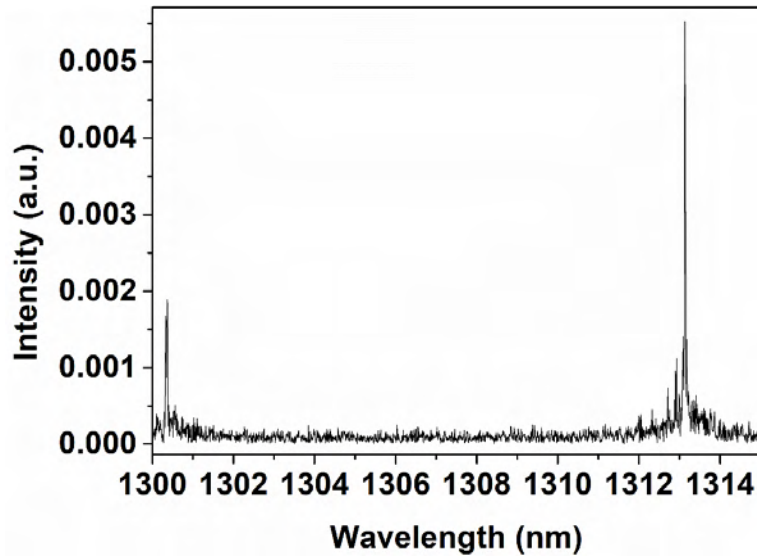


Figure 4-10 Spectrum measurement of the vanadate-based second Stokes output using a wavemeter

## 4.4 Diamond Raman laser using a 1064 nm pump

In order to further verify the model, we use diamond as the Raman gain medium to achieve the second Stokes output using the 1064 nm pump, at a much higher pump power than in the previous chapter. For these measurements we replaced the pump seed laser with one with a narrower linewidth, thus solving the locking problem that we saw with the vanadate laser above.

Figure 4-11 shows the power output data of the reflected pump power  $P_{Prefl0}$ , first Stokes  $P_S$ , and second Stokes  $P_{SS}$  data (markers) with the model simulation result (lines). The laser setup is the same as it is in chapter 3, just using a different pump mirror transmission as the pump source changed. The spot size was 20  $\mu\text{m}$ . Here a 1064 nm laser pumped the second Stokes system resulting in  $\lambda_S = 1240 \text{ nm}$  and  $\lambda_{SS} = 1485 \text{ nm}$ . The maximum second Stokes power was 1548 mW at 17.05 W pump power. As in the first Stokes system, retro mirrors (DM2, DM1 and corresponding HR mirror in Figure 4-1) were used to counter-propagate the first and second Stokes fields resulting in a single longitudinal mode operation of the first Stokes. Unfortunately, even when using stronger feedback

compared to our previous work [111], we were not able to confirm stable SLM second Stokes output.

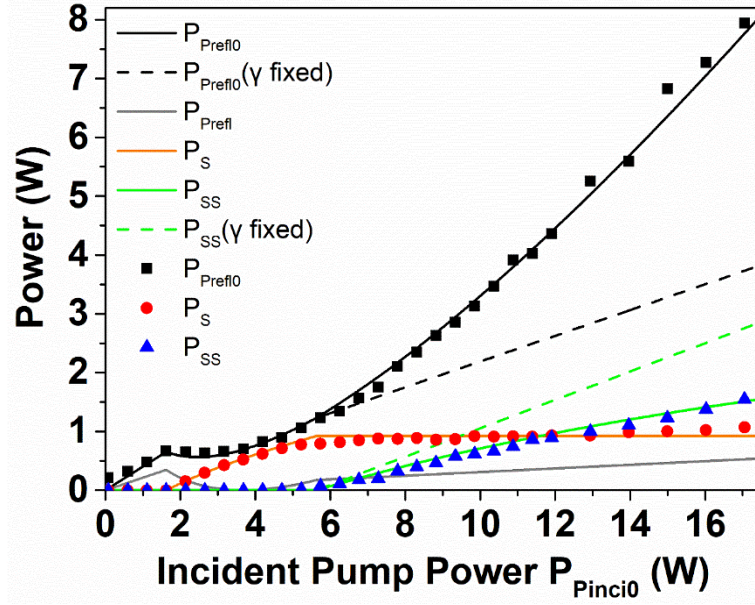


Figure 4-11 Power output and reflected pump power for the second Stokes laser. The black line is the reflected pump power  $P_{Prefl0}$ , while the grey line shows the mode-matched part  $P_{Prefl}$ . The dotted lines represent the fitting result with a fixed  $\gamma$  value

The first Stokes power remains at around 1070 mW after the second Stokes threshold, reflecting the fact that it must provide gain to balance the constant second Stokes loss. Using  $g_s = 11.21 \text{ cm/GW}$  [106], we use the model to fit the matching parameter  $\gamma = 0.81$ , and passive losses of  $L_P = L_S = L_{SS} = 1.02\%$  (in order to simplify the fitting parameter, we use the same passive loss for all fields). The dashed modelling curves in Figure 4-11 fit the measured data reasonably well below second Stokes threshold, but diverge significantly above second Stokes threshold where the predicted second Stokes slope efficiency is too high and the predicted reflected pump is too low. Using the model to investigate possible causes, it appears that changing the mode matching parameter  $\gamma$  is the only reasonable way to explain the discrepancy. Using a simple heuristic formula to explore this idea, we set  $\gamma$  above second Stokes threshold to be a function of pump power added above the second Stokes threshold as

$$\gamma' = \frac{\gamma}{1 + k(P_{Pinci0} - P_{SSth})}, \quad (4-1)$$

where  $k$  is a proportionality factor. As the solid line in Figure 4-11 shows, using  $k = 0.038$  simultaneously improves the fit of second Stokes slope and the growth of the reflected pump power, supporting this explanation. With this  $k$ , this model is a gradual change in  $\gamma$  from 0.81 at second Stokes threshold to 0.57 at full pump power. To confirm experimentally why the mode matching might change needs more investigation: one possibility is small changes to the cavity transverse mode due to onset of thermal lensing and/or distortion as above 2<sup>nd</sup> Stokes threshold the pump deposits twice as much heat into the crystal.

We also considered what influence other changes to cavity parameters might have. For example, we measured a change in reflectivity of the IC/OC mirror as a function of temperature: a change of about 80°C shifted  $R_P$  and  $R_{SS}$  by about -0.4% and -0.1%, respectively. However, such changes don't significantly affect the model output and are not able to explain the strong increase in the reflected pump power.

## 4.5 Optimization

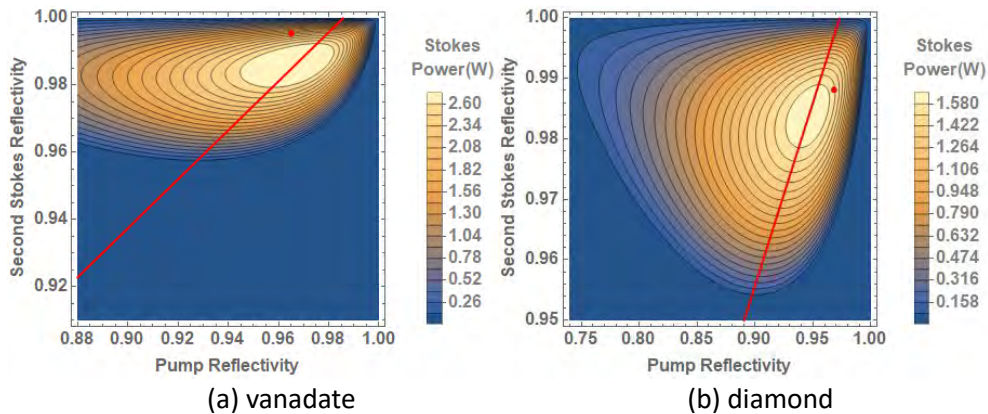


Figure 4-12 The second Stokes Power as a function of reflectivity of pump and second Stokes for the vanadate laser (a) and the diamond laser (b). The parameters are the same as in the experiments, the red line shows the impedance matching condition. The red spot are the output coupler reflectivities used in the experiment.

Figure 4-12 explores the optimization of the input/output mirror reflectivities for the pump and second Stokes fields (the reflectivity for the Stokes field should be as high as possible, with any transmission accounted in the Stokes passive loss). For the vanadate laser, we generate only 417.5 mW from maximum possible of 2600 mW; our mirror here is far

from optimum, reflecting the fact that is designed for quite different mode size and power level. For the diamond laser, the mirrors used in the experiment were close to optimal, generating 1548 mW out of a possible 1673 mW. Note that we use the lowered value of  $\gamma = 0.57$  that fitted the experiments at maximum power.

## 4.6 Conclusion

In this chapter we designed and built a ring cavity vanadate Raman laser at 1064 nm pump. Strong thermal lensing prevented locking for the design cavity waist of 20  $\mu\text{m}$ , requiring us to use a much larger waist of 48  $\mu\text{m}$ . We used the model to fit the measured data and obtained good fitting result in vanadate laser, but indicating a very low mode-matching coefficient of 0.48. We analyzed the reason for the bad coupling, which turned out to be due to the linewidth of the pump laser being too large to effectively couple to our resonant cavity. This part of our work was significantly affected by the university's COVID shutdown.

We changed to a narrower seed laser for the pump to allow efficient coupling, and built a cw diamond second Stokes laser. For the diamond Raman laser, in order to fit the data well above second Stokes threshold, we needed to model a mode-matching parameter that changed with pump power. This implies the heat deposited in the diamond significantly affects the mode-matching parameter when the second Stokes was generated. We used the model to generate second Stokes output contour maps as the function of the pump and second Stokes reflectivity show that for the diamond laser, we were close to the optimum performance. We should get far more output power if we are able to prevent the  $\gamma$  parameter from deteriorating as the pump power increase above the 2<sup>nd</sup> Stokes threshold.

## 5

# Chapter 5. Single longitudinal mode external cavity diamond Raman laser

## 5.1 Introduction

Continuous-wave (cw) single-longitudinal-mode (SLM) lasers play a key role in precision measurements and light-matter applications [86,87]. In Raman lasers, SLM or narrow linewidth operation is usually reached by using birefringent filters or etalons in the cavity [115], using frequency locking to stabilize the Raman cavity [96], or using cryogenic cooling to narrow the Raman gain linewidths [116]. As we have discussed, as Raman lasers do not have spatial hole-burning that leads to multimode operation in inversion lasers, a Raman laser can in principle lase on a single longitudinal mode even when pumped with a multimode laser [117]. Thus with good stabilization, Raman lasers tend to run SLM naturally due to one mode seeing the highest gain [95]. However, thermal and mechanical cavity instabilities or a noisy pump source (spectrally or temporally) seems to make the Raman intracavity field oscillate at multiple longitudinal modes, especially at higher output powers. Therefore, exploring these broadening effects and other possible ways to stabilize the Stokes SLM spectrum is important.

In a ring resonator, Kitzler et al. showed that using a retro reflecting mirror to force the Stokes field to oscillate unidirectionally, combined with a frequency locked and mechanically stable cavity, achieved SLM operation [98]. In this thesis we have further

observed cascaded 2<sup>nd</sup> Stokes SLM operation by controlling the 1<sup>st</sup> Stokes and 2<sup>nd</sup> Stokes to be counter-propagating, in Chapter 3 (published as [111]).

For a linear cavity without cavity enhancement, conventional SLM control methods like etalons and cavity locking are still being widely used. As discussed in the first chapter, O. Lux, S. Sarang, et al. demonstrated a tunable external cavity to achieve the SLM Raman operation manual control of the cavity length and filtered feedback using a volume Bragg grating [86]. Q. Sheng, R. Li, et al demonstrated a cw intracavity Raman laser with SLM operation by using etalons [115]. In contrast, X. Yang's cw Raman laser ran SLM generating doubled output at 620 nm with efficient SHG conversion [99] with no intracavity etalons nor filtered feedback. As discussed in chapter 1, with frequency doubling in the cavity, sum-frequency mixing can suppress additional axial modes so that only a single longitudinal mode oscillates. This method can potentially provide an effective method for stabilizing SLM Raman laser sources. In this chapter, we use the SHG mode suppression method to achieve SLM operation of an efficient first Stokes Raman laser. The difference to Yang's 620 nm laser is that our focus is on the Stokes output rather than the doubled output, so we are designing a laser to output the first Stokes, while adding the smallest amount of SHG conversion that is required to achieve SLM Stokes output.

## 5.2 Experimental setup

### 5.2.1 Setup design

To verify the self-suppression effect of axial modes by SHG, we need to design the cavity and LBO crystal to get the balance between highest Stokes SLM output and lowest SHG power.

#### LBO design

The intensity of the generated second harmonic with the small signal assumption can be expressed as follows [118]

$$I_2(L) = \frac{2\omega_1^2 d_{eff}^2}{\varepsilon_0 c^3 n_1^2 n_2} L^2 I_1^2(0) \text{sinc}^2\left(\frac{\Delta k L}{2}\right), \quad (5-1)$$

where subscript 2 means the second harmonic wavelength and 1 means the fundamental wavelength,  $I$  is the intensity,  $L$  is the crystal length,  $\omega$  is frequency,  $d_{eff}$  is the effective nonlinear optical coefficient,  $\varepsilon_0$  is the permittivity of free space,  $n$  is the refractive index of the crystal, and  $\Delta k$  means the phase mismatch (the process is phase-matched for  $\Delta k = 0$ ).

The phase matching in LBO can be either Type I, where the incident waves have the same polarization, or Type II, where they are orthogonal. In a diamond Raman laser for maximum gain, the Stokes field is linearly polarized aligned with the pump and thus Type I is appropriate. As non-critical phase matching would require temperatures over 100 °C we also decided on a critically phase matched, although we designed for 70 °C so we could maintain temperature control even where there was heating in the LBO.

To design the LBO size and cut we used the SNLO software[119], which solves the equations for most nonlinear effects. After inputting the crystal type, principal plane, working temperature and wavelength, we find the correct phase match type and phase matching angle of 32.9 degrees, which is shown in Figure 5-1.

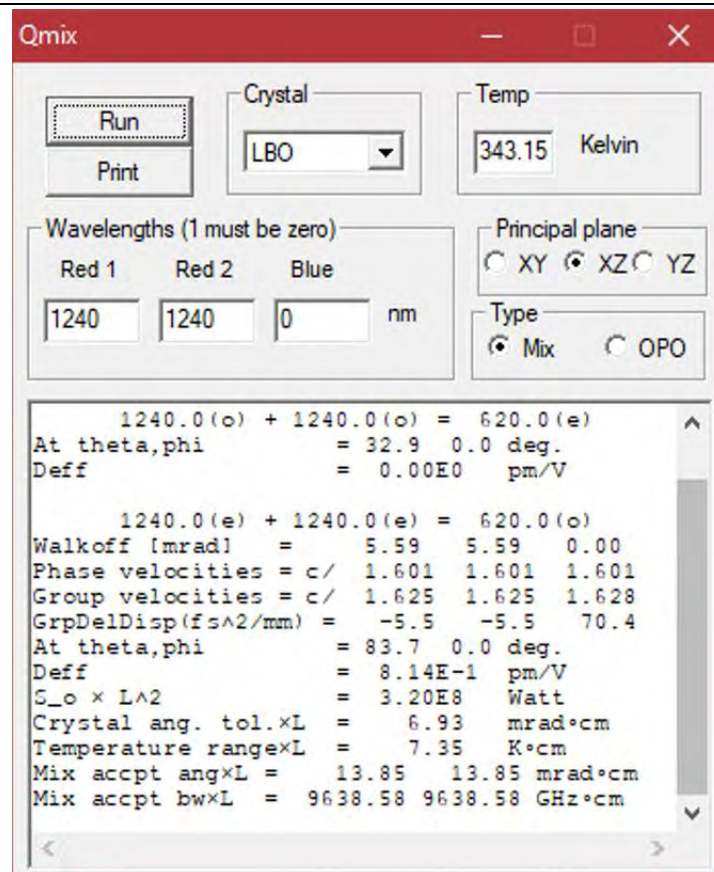


Figure 5-1 The design result of LBO by SNLO

The next important parameter is the length of crystal, which is quadratic in the function for SHG power. To convert about 0.1% of the Stokes intracavity power into SHG output (for comparison, the optimal output coupling for the Stokes field for tends to be of order about 0.5%), we designed a cube LBO with  $5 \times 5 \times 5 \text{ mm}^3$  size, and placed it near the diamond to access the smaller beam size. The converted SHG power will be loss for the Stokes power, and we want to be able to adjust its strength to see how little SHG could be used to still get a stabilizing effect; the SHG strength was adjusted by tuning LBO temperature, LBO angle, and beam size in the crystal by translating LBO along the Stokes beam.

### Raman Laser Cavity Design

Different from the Chapter 3, here we used a 1064 nm Precilaser fiber laser with 60 W of maximum power, thus it was unnecessary to use a pump enhancement cavity. Utilizing a double-pass cavity was sufficient for a moderate Stokes threshold [18]. A folded cavity can



effectively tighten the focus between the curved mirrors and provides extra space for positioning of other intracavity components. As a 3-mirror cavity is a bit simpler than a 4-mirror cavity, but still maintains the advantages, we firstly built a 3-mirror cavity and inserted an LBO crystal in the long arm as it provides a second focus point with a bigger waist size. By using a curved end mirror (M3 in Figure 5-2) the focus size and position can be adjusted by the choice of its curvature. However, alignment of the 3-mirror cavity was rather difficult. As the cavity was only double passing the pump, we could not use the pump resonance for alignment. The best way to align M3 was by using a visible alignment laser overlapped with the pump beam. Another difficulty was the astigmatism due to the cavity fold, which makes the beam shape in the long arm and misaligns that cavity stability properties in the two planes. Due to these complications we decided to further simplify the design and use a 2-mirror cavity, whose design has been well explored previously [18].

Without the folded long arm, there is no need to use a visible alignment laser and a simple alignment method using the back reflected beam and apertures works. The LBO is inserted near the diamond and can be moved along the expanding beam to control the efficiency of the SHG conversion. The smallest beam radius in the middle of the LBO was about  $60\text{ }\mu\text{m}$ . The waist size can be controlled by adjusting the distance between M1 and M2, although these cavities do run close to their stability limit in order to achieve a small waist.

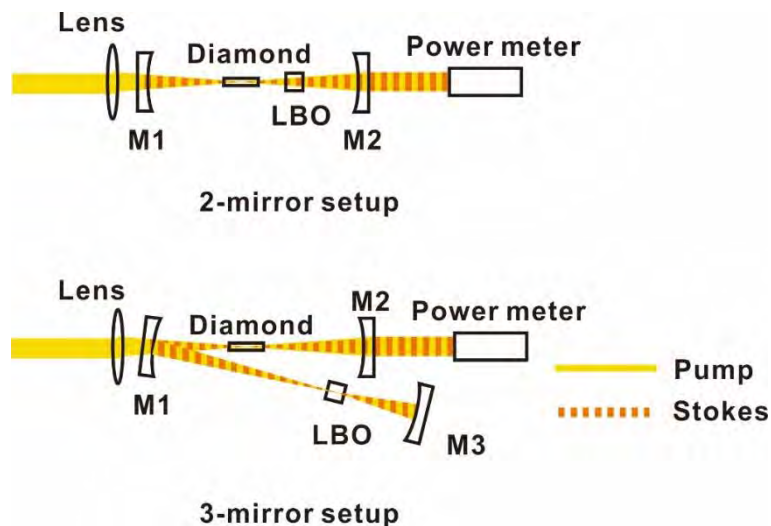
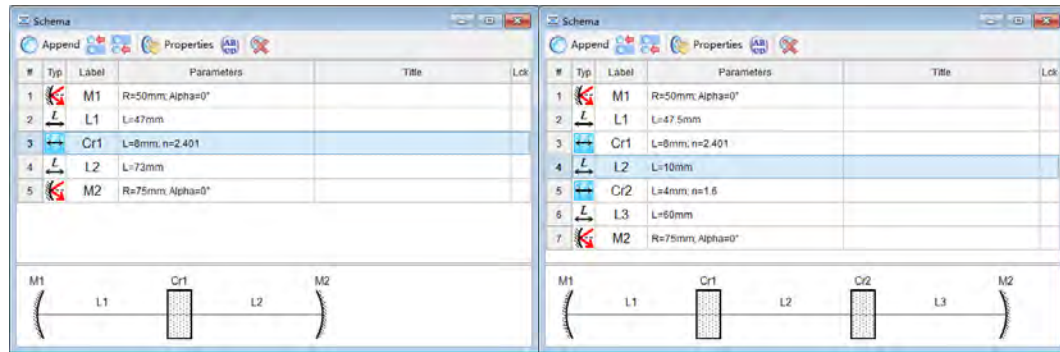


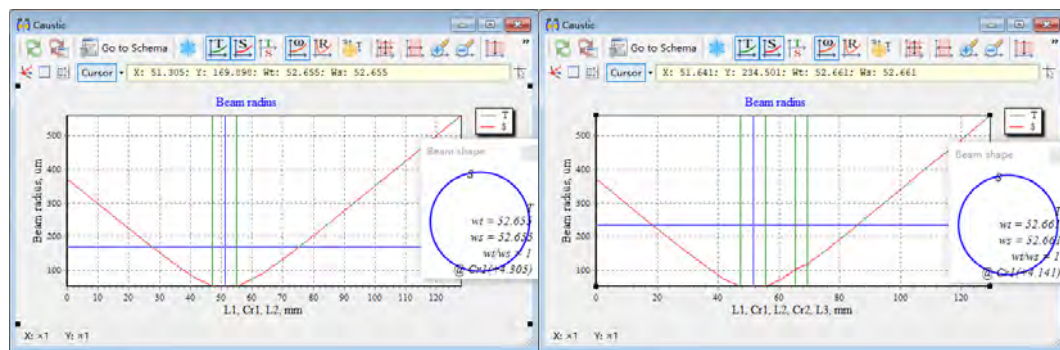
Figure 5-2 Comparison of 2-mirror setup (top) and 3-mirror setup (bottom).

For the mirror curvatures, we chose a 50 mm IC, which allowed for a small pump spot size and a 75 mm OC to have extra space for the LBO



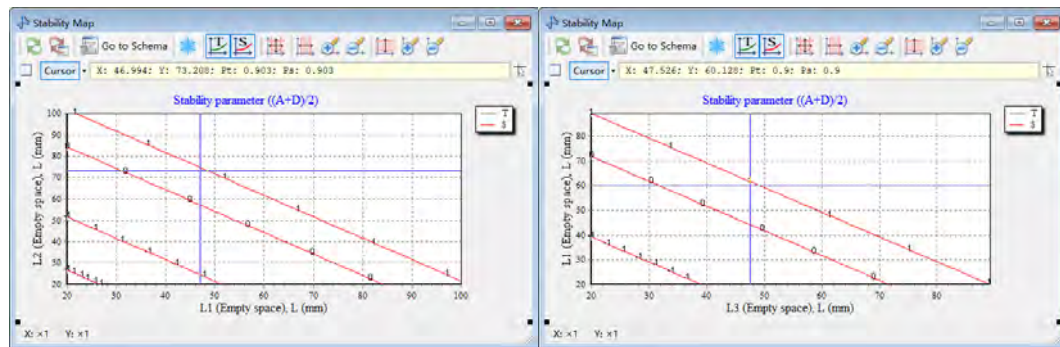
(a) Cavity setup without LBO

(b) Cavity setup with LBO



(c) Beam diameter simulation without LBO

(d) Beam diameter simulation with LBO



(e) Stability map without LBO

(f) Stability map with LBO

Figure 5-3 The cavity setup (a,b) the beam size simulation (c,d) and stability map (e,f) in the reZonator, where (b), (d) and (f) is the cavity design with LBO in.

The cavity design is shown in Figure 5-3. The waist radius in diamond is 52  $\mu\text{m}$ , and it is 110  $\mu\text{m}$  in the middle of the LBO. To characterize the performance of the cavity without SHG conversion we also designed a cavity without the LBO crystal. The length of the cavity was chosen so that the waist size in the diamond was identical, as the Figure 5-3(c) and Figure 5-3(d) shows.

A longer cavity makes Stokes waist smaller, however, it will move the cavity towards the edge of the stability, which can deteriorate the Stokes stability. Thus we choose a mirror distance producing a 52  $\mu\text{m}$  radius in the diamond, where the stability of cavity without LBO (0.903) and with LBO (0.9) is 1.5 mm from the stability edge. We matched the pump size to this cavity waist to encourage TEM00 mode operation of the Stokes.

### 5.2.2 Setup overview

Here we describe the setup of the linear cavity Raman laser shown in Figure 5-4. The pump was a cw 1064 nm Precilaser fiber laser with 60 W of maximum output power. An isolator at the output port of the pump source was necessary to prevent back reflections causing catastrophic damage to the fiber amplifier. After the isolator a telescope system expanded the pump beam to 8 mm in size. A halfwave plate was used to rotate the pump polarization and align it with the diamond crystallographic orientation.

The resonator was a two-mirror linear resonator with double-passed pump, where the input coupler M1 had 50 mm curvature and was HT at 1064 nm and HR at 1240 nm, and the output coupler M2 had 75 mm curvature and was HR at 1064 nm and had 0.5% transmission at 1240 nm, which is appropriate for efficient conversion of a 60 W laser [18]. For stability, M1 and M2 were fixed on stable pedestal posts with 1 inch diameter, on translation stages to have flexible cavity length adjustment. The diamond was 2×2×8 mm in size with AR coating at 1064 nm and 1240 nm on the 2×2 mm faces. The diamond was cut for propagation along the [110] direction to get the highest gain for the pump polarization aligned with the [111] direction (See Ref. [108]). The diamond was placed on a water-cooled holder at the focus point of the cavity. The pump was focussed into the crystal using a 50 mm lens. The pump focusing lens was also on a Z translation stage and placed in a XY translation mount. The spot radius of Stokes and pump are similar at about 50  $\mu\text{m}$  in order to suppress the higher transverse modes of the Stokes field. A 5×5×5 mm cube shaped LBO designed for SHG conversion of 1240 nm light at the temperature of 70 °C was AR coated at 1064 nm and 1240 nm. The position and height of the diamond and LBO was controlled by separate XYZ stages for independent control of their positions.

As the powers involved are significantly higher compared to the ring cavities in previous chapters, the setup required a cooling system. The diamond holder (similar to Chapter 3) and the hot side of the thermo-electric cooler (TEC) controlling the LBO temperature were connected to a “quiet” cooling loop with minimal vibrations. The pump laser was water cooled using a commercial chiller (NESLAB CFT-25) separated from the laser laboratory to prevent vibrations from affecting the laser system.

The TEC used for temperature stabilization of the LBO was controlled with temperature stability better than 0.1 °C. A resistor was added to the LBO mount to provide additional heating assistance.

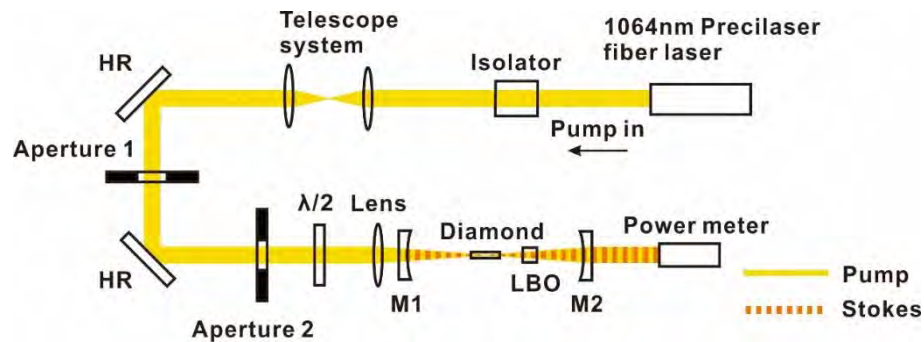


Figure 5-4 The linear cavity setup. Note that the beam path of SHG from Stokes is ignored.

Compared to the ring cavity, the linear cavity is more difficult due to align due to the lack of the reference of the pump inside the cavity. In the coarse-tuning stage, we can align the feedback of pump field to ensure M1 and M2 are close to parallel, and back reflections off crystals can be used to get them close to normal incidence. We aligned the cavity first without the LBO, and then inserted the LBO with an appropriate increase in the mirror separation to allow for the refractive index of the crystal. Figure 5-5 shows the lasing cavity.

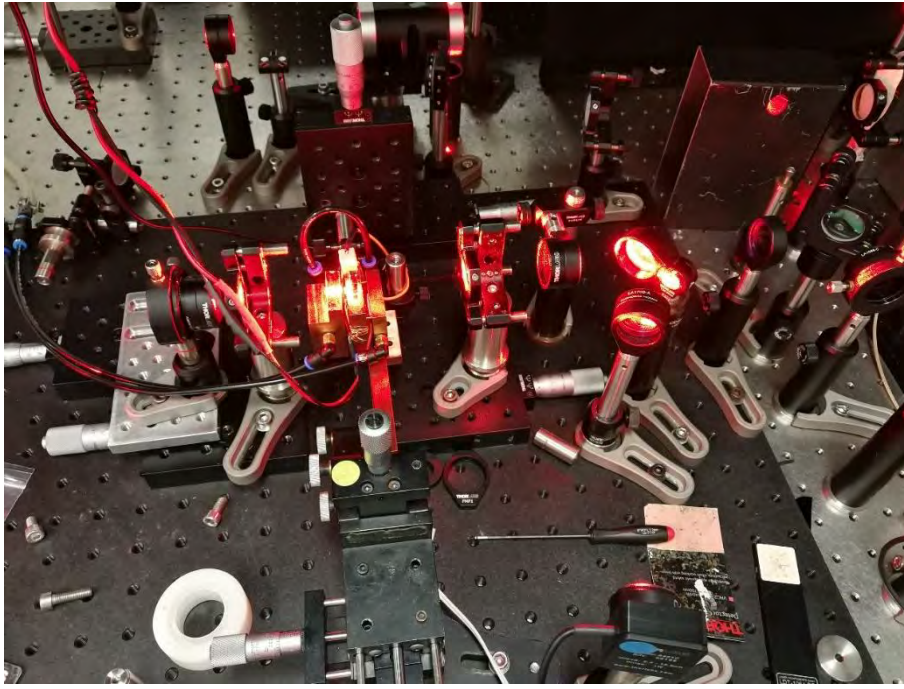


Figure 5-5 The SHG light in the cavity

## 5.3 Results and discussion

### 5.3.1 Output power

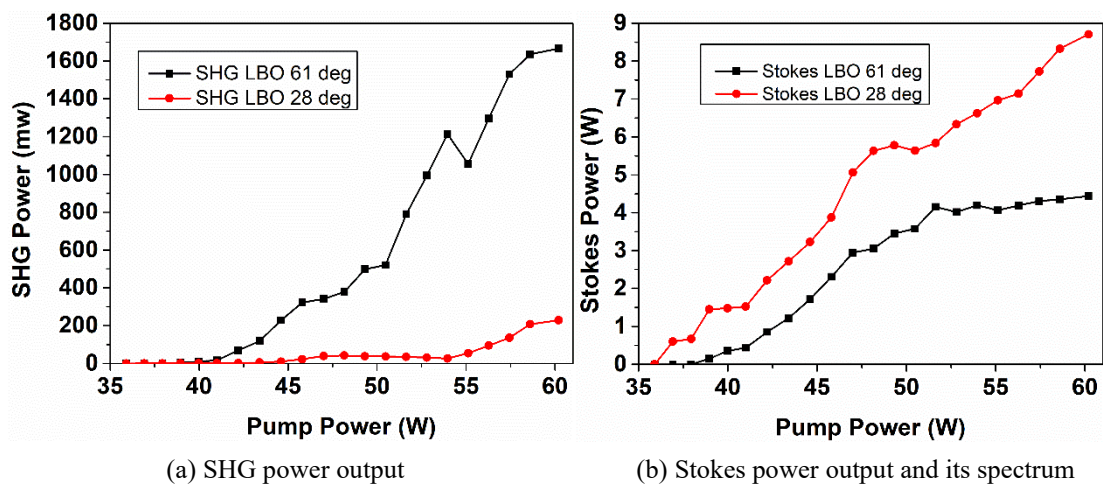


Figure 5-6 Power input/output curve of SHG (a) and Stokes power (b) with different LBO temperatures.



The SHG and Stokes outputs were separated using dichroic mirrors and filters and measured using calibrated power meters. The powers were corrected for loss due to the filtering optics, and in the case of SHG, we doubled the one-way power to account for backward conversion (assuming identical forward and backward conversion).

Figure 5-6 shows the SHG and Stokes output power as function of pump power for phase matched LBO temperature of 61 °C (found to maximise the conversion) and phase mismatched temperature of 28 °C. When LBO temperature was mismatched, the SHG power was suppressed below 200 mW and the Stokes output power reached 8.7 W at 60.2 W of pump with slope efficiency of 35.8%. When LBO was phase matched, the Stokes power reached 4.4 W with 19.9% slope efficiency and the corresponding SHG power was 1665.4 mW.

As the diamond and LBO AR coatings were not optimized at 620 nm and the crystals were not perfectly perpendicular to the pump beam, there were multiple reflections of the 620 nm beam inside the cavity (see Figure 5-7). Thus we suspect that the actual generated SHG output power was somewhat higher than shown in Figure 5-6.

Comparing our results to similar previously-published lasers shows that our laser had a high threshold and was less efficient compared to [89,95], but quite similar to [99]. Comparison of the different configurations listed in Table 5-1 reveals that the main difference was the AR coating of diamond. The reflection of the diamond coating at the Stokes wavelength was 0.06% in the case of the low threshold lasers [89,95] but was about 0.3% here and in [99] where threshold was higher and conversion efficiency was lower. As the typical output coupling in these systems is only 0.5%, the conversion efficiency is very sensitive to extra passive loss inside the cavity [18] introduced by imperfect AR coatings.

So while our Stokes lasing efficiency was not as good compared to the best other lasers, the purpose of this laser setup was to investigate the axial mode suppression effect of SHG, and so we are not too concerned with our understood lower power and efficiency.

Table 5-1 The comparison of our laser to similar other lasers

	Lux's setup[95]	Yang's setup [99]	Yang's second setup[89]	Our setup
Threshold	12 W	50 W	13 W	35.9 W
Slope efficiency	62%	43%	34.9%(*)	35.8%
M <sup>2</sup> factor	1.05	-	1.23 Pump 1.08 SHG	1.16
cavity mirror curvature(M1-M2)	50-50 mm	50-50 mm	50-50 mm	50-75 mm
IC mirror coating	97.2% T-pump 99.9% R-Stokes	99.2% T-pump 99.98% R-Stokes 65% T-SHG	98% T-pump 99.9% R-Stokes 35% T-SHG	98% T-pump 99.9% R-Stokes
OC mirror coating	99.9% R-pump, 0.43% T-Stokes	99.8% R-pump 99.6% R-Stokes, 30% T-SHG	99.9% R-pump and Stokes, 39% T-SHG	HR-pump 99.5% R-Stokes
waist radius	40 μm of pump 50 μm of Stokes	45 μm of pump 53 μm of Stokes	27 μm of pump 32 μm of Stokes	about 50 μm of pump and Stokes
Diamond coating	AR 0.06% at pump and Stokes	AR 0.3% at pump and Stokes	AR 0.06% at pump and Stokes	AR 0.3% at pump and Stokes

\* conversion efficiency from pump to doubled Stokes.

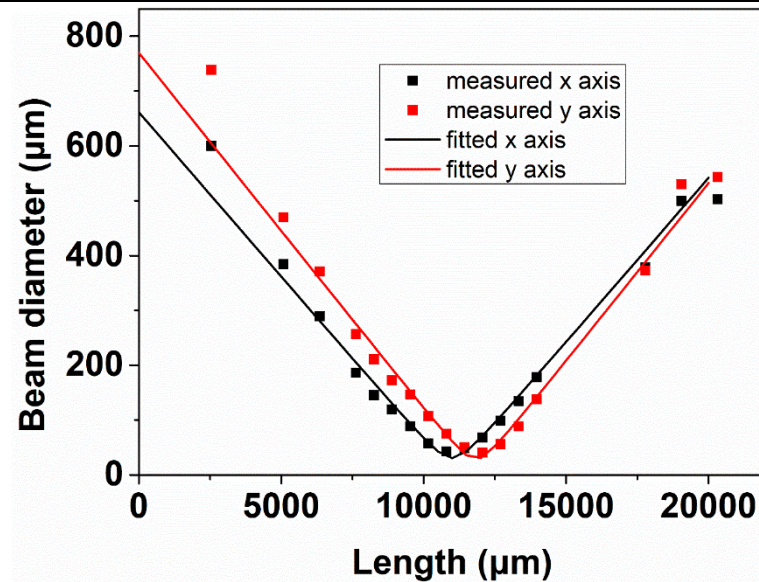
### 5.3.2 Stokes beam quality

The M squared factor of the Stokes beam was measured by fitting the caustic of a 50-mm-focal length lens by Eq. (5-2) [120]

$$\omega^2(z) = \omega_0^2 \left[ 1 + \left( \frac{z-z_0}{\frac{\lambda M^2}{\theta^2 \pi}} \right)^2 \right], \quad (5-2)$$

where  $z$  is the location of sampled cross-section of beam,  $z_0$  is the location of the waist.  $\omega$  is the beam waist and  $\omega_0$  is the focus beam waist,  $\theta$  is the divergence angle, and  $\lambda$  is the wavelength of the laser field.

The beam quality with the phase-mismatched LBO was measured to be 1.16 as shown in Figure 5-7. The excellent beam quality of the diamond Raman laser is caused by Raman self-cleaning effect and excellent thermal properties of diamond [81].

Figure 5-7  $M^2$  for Stokes beam size

With phase-matched LBO the Stokes spatial mode became slightly distorted, as shown in Figure 5-8 and the beam quality dropped to an  $M^2$  of 2.5. Thermal effects in the LBO crystal may play a role, but we attribute this to the LBO changing the balance of the transverse mode competition: higher order mode experiences lower loss due to lower SHG conversion than TEM<sub>00</sub>, but can have similar gain if pump and Stokes waist sizes are similar (or if the pump is larger). This can shift the balance in favour of higher order modes. This issue can be mitigated by stronger focussing of the pump beam to smaller than the Stokes waist size to lower the gain for higher transverse modes [13].

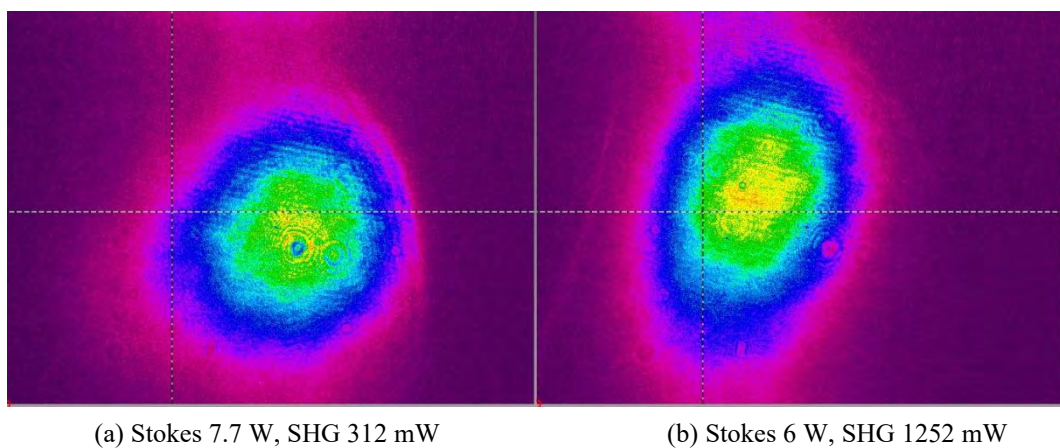


Figure 5-8 The Stokes beam shape for different SHG powers



### 5.3.3 Spectrum analysis

As observed in literature [89,95,99] and our experiments, the Stokes output of DRLs doesn't remain SLM at higher output powers. We see the same in our current experiment. An example, measured by a F-P interferometer with a 10 GHz FSR, is shown in Figure 5-9, where close to threshold (point a, 0.6 W of Stokes output power) the output is SLM, but progressively becomes MLM at higher powers (point b, 7.76 W of Stokes output power).

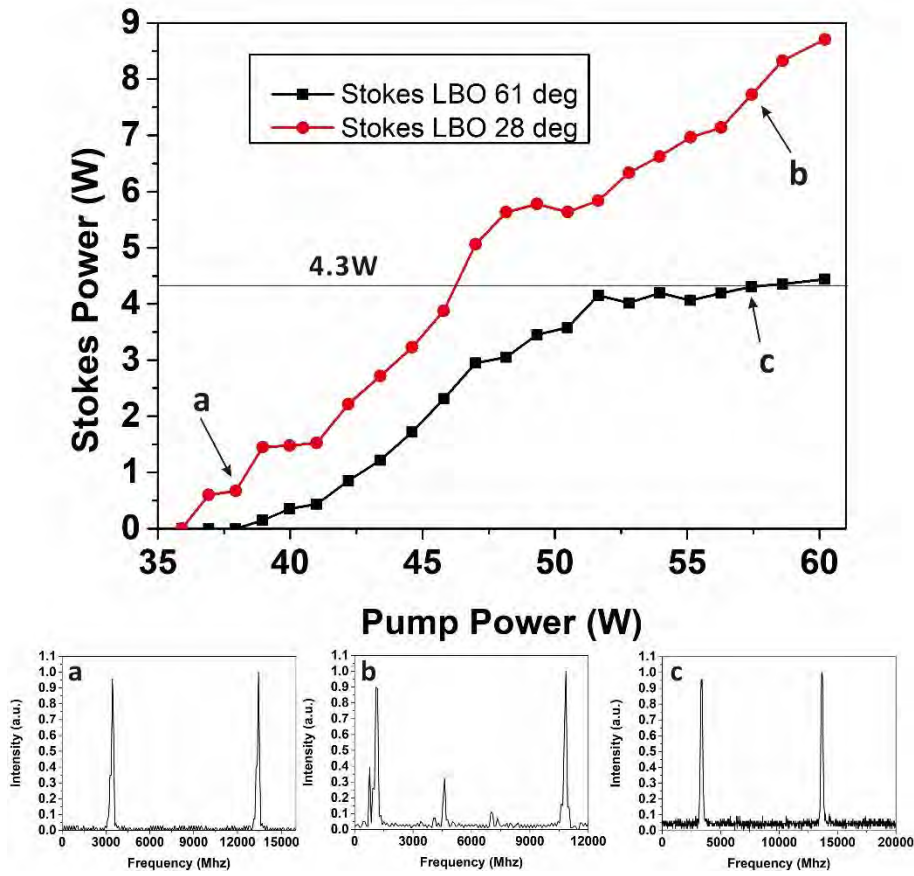


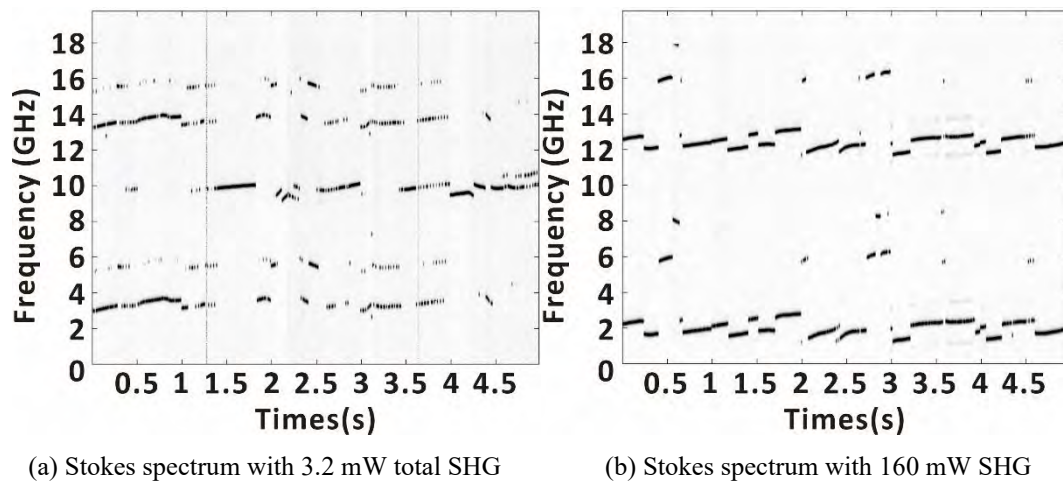
Figure 5-9 Stokes longitudinal mode spectrum at different output powers.

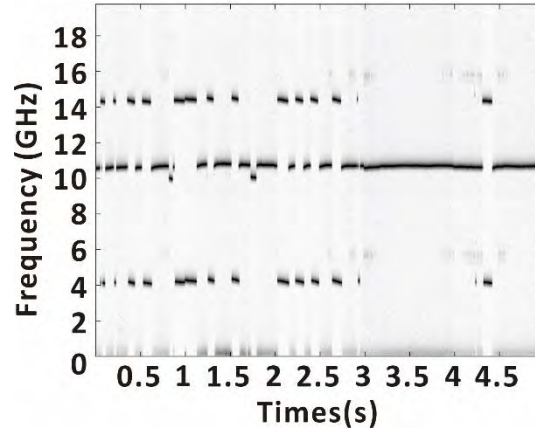
In order to demonstrate the evolution of the Stokes spectrum as a function of SHG conversion we eliminated most possible sources of noise in the system, including mechanical vibrations and acoustic noise. We also kept the Stokes power constant at 4.3 W throughout the measurements to ensure consistent intracavity thermal conditions: By tuning the

temperature of the LBO and changing the pump power, the effectiveness of the SHG axial mode suppression effect is explored at the same Stokes power level.

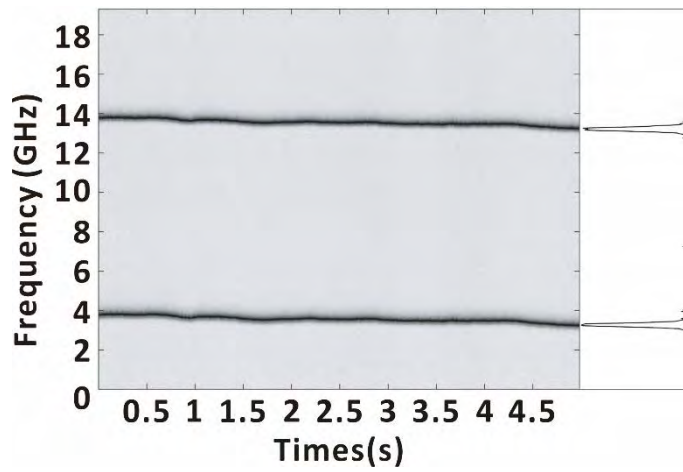
Figure 5-10 shows a time series of 1000 consecutive F-P scans collected over 5 s. At negligible SHG conversion (Figure 5-10a) the Stokes field oscillated on multiple longitudinal modes with frequent mode-hops. As the SHG conversion increased the number of modes decreased and hopping became less frequent (Figure 5-10b,c). Finally, when the SHG power reaches 1250 mW (about 0.14% conversion, counting all SHG output), we observed a stable SLM output over 5 seconds (see Figure 5-10d). It confirms that SHG generation inside a Raman cavity helps to stabilize Stokes SLM operation, however, the amount of SHG required in this case is about 23% of the Stokes output power out-coupled by SHG and OC.

The horizontal lines representing the position of the modes in Figure 5-10 are not horizontal, but often slope up or down indicating changes in the optical length of the cavity. We attribute this to drifts of the temperatures in the crystals. Although the temperature of both crystals was stabilized (diamond passively, LBO actively) rapid changes in the number of modes may cause changes in depletion and thus power deposited in the diamond. Similar effects were observed in [95].





(c) Stokes spectrum with 940 mW SHG



(d) Stokes spectrum with 1250 mW SHG

Figure 5-10 The waterfall diagram of the Stokes spectrum with different powers of SHG. The FSR is 10 GHz, so SLM operation will show two approximately horizontal lines.

We believe that the longitudinal mode instability is mostly caused by fast mode-hopping. To determine whether the Stokes lased at multiple modes simultaneously or hopping between single modes, we used a Hyperfine spectrometer with 0.15 GHz resolution (our cavity FSR was about 1 GHz). However, even on the shortest exposure time of 20 ms, multiple peaks were present at the same time. Therefore, we used a F-P interferometer with a high scanning speed of 10  $\mu$ s, which can measure consecutive spectra fast enough to resolve the mode changes, and a fast oscilloscope with 4 GHz bandwidth and enough sampling resolution to collect consecutive scans over 5 s. It can be seen in Figure 5-10a-c and Figure 5-11 that mostly a single longitudinal mode changes position between the scans. Occasionally, the mode seemingly changed position by less than the 1 GHz FSR of the cavity

(see spot C and D in Figure 5-11, while the gap between A, B and C are about 1 GHz). This could be caused the Stokes spatial mode changing to a higher order transverse mode with difference Gouy phase.

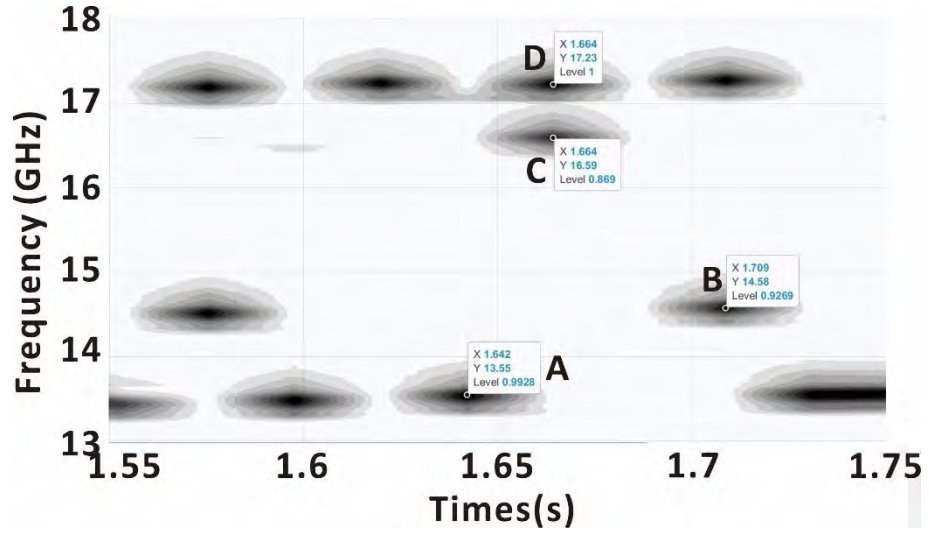


Figure 5-11 The waterfall picture of the Stokes spectrum under 3.6 W Stokes power and 1250 mW SHG power. The greyscale shows the height of the peak.

### 5.3.4 Stability analysis discussion

Although we confirmed the axial mode suppression effect of SHG to control the longitudinal modes, the instabilities in the system still caused occasional mode hops when measured over longer periods of time.

The temperature control system (TEC plus a resistor) of the LBO was rather slow to react to changes in pump power and Stokes intracavity and SHG power. Even with the temperature probe close to the crystal, the system needed several seconds to react and affect the temperature of LBO.

We kept the Stokes average output power stable, however, due the Stokes transverse mode profile and power fluctuated on a ms time scale. This caused fast changes in depletion of the pump and thus power deposition into the diamond. As the specific heat capacity of diamond is relatively low (0.5 J/(g K)) these changes can cause enough temperature and thus refractive index change to perturb the optical length of the cavity [95]. While we carefully

mitigated sources of mechanical and acoustic noise, some vibrations still might have been transmitted to the floated optical table through air and tubing of the cooling system. As crystals were inserted in the cavity from the side and required XYZ positioning they were the most vibration susceptible components.

When diagnosing the Stokes stability, we also measured the stability of the pump source as shown in Figure 5-12. Although the pump power changed only by about  $\pm 1\%$ , it caused fluctuations in the Stokes power and the SHG conversion associated with all the detrimental effects mentioned above. These fluctuations limited the collection of reliable data to about a minute at a time.

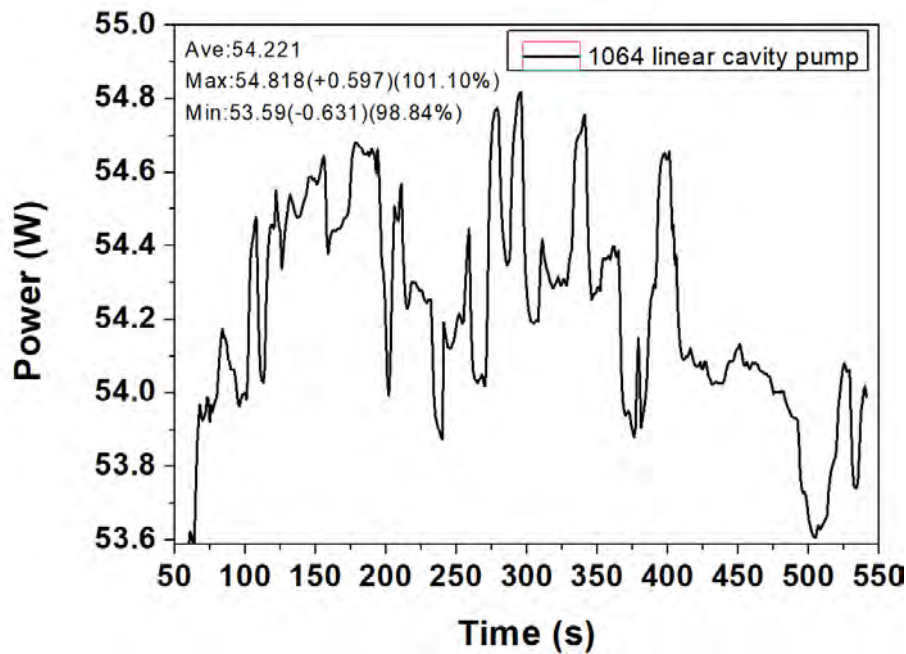


Figure 5-12 The pump power fluctuation in 500 seconds

During the cavity alignment we found that occasionally multiple nonlinear effects were observed at the same time (see Figure 5-13). An orange beam results from the SFM between pump (1064 nm) and Stokes (1240 nm), while the green beam is the SHG of the pump source. When changing the temperature, it was possible to phase match these other nonlinear effects. Only the SFM between the different Stokes modes contributes to the suppression of the weaker Stokes modes [100], so ideally these other processes should be suppressed.

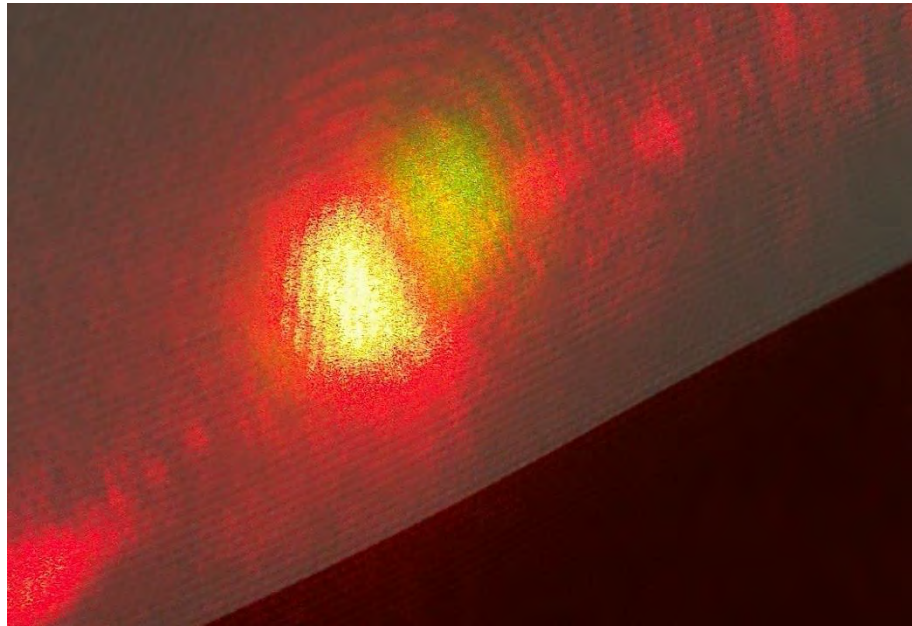


Figure 5-13 The red, orange and green beams leaking from the cavity

## 5.4 Conclusion

We performed a study of the axial mode suppression effect due to intracavity harmonic generation in an efficient DRL. We built a linear Raman cavity DRL with intracavity LBO and achieved 4.3 W of Stokes output power with stable SLM output. By comparing the Stokes output spectrum with different SHG output powers and constant Stokes output, we demonstrated that about 0.15% of SHG conversion (one third of Stokes output power) is enough to suppress the axial modes and force the Stokes into SLM operation. This confirms that the method outlined in [100] is suitable for stabilising not only strongly-doubled lasers [89], but also for lasers designed for non-doubled output. It seems possible that SHG stabilisation may play an important role in stabilising a range of lasers of this type. With lower environmental and thermal noise, it is likely that the amount of SHG required may be substantially reduced.



# 6

## Chapter 6. Conclusion

Raman lasers, as a method to shift the laser wavelength, play an important role for applications of lasers: especially since the breakthrough of diamond growth technology, which has arguably brought the study of Raman laser into a new stage. Because of its excellent Raman gain, large Raman shift, and superlative thermal performance, diamond has brought substantial developments in continuous wave regime particularly in higher power output external cavity Raman laser designs. In this thesis, we have made advances in the design of cascaded cavity-enhanced designs.

### 6.1 Summary

The thesis presented here has mainly completed exploration of two aspects of DRLs. The first is investigating the pump resonant Raman cavity, including developing a model to describe the behavior of Stokes and reflected pump. Ring cavity lasers were designed and constructed, and achieved second Stokes operation. The second is realizing the single longitudinal mode operation of Raman lasers using two novel methods.

We developed the pump resonant Raman model by combining the theory of resonant laser enhancement with theory of stimulated Raman scattering. The model is written in terms of practical parameters, such as mirror reflectivity, beam radius and passive loss, which makes the model readily applied to real lasers. The model successfully predicts the output

Stokes power and reflected pump power for lasers with different pump wavelengths and different Raman crystals, which signifies the validity of the model. By exploring the relationship of parameters in the model, we explained the mechanisms underpinning the operation of the pump resonant Raman laser. We found that the reflected pump power was much higher than might be expected, and included the  $\gamma$  ‘mode matching’ fraction value, which became a crucial parameter for characterization of real lasers. By comparison with experiments, we found that this correction plays an important role for correct modelling of the reflected pump and correctly estimating other laser parameters, such as loss. Furthermore, we derived the equations for optimum mirror reflectivity to achieve the maximum Stokes output for a given pump power, which is critical for designing efficient pump resonant Raman lasers. Consideration of the importance of crystal length made us realize that the crystal length has an optimum that depends on crystal quality.

We successfully designed and built ring cavities to generate stable second Stokes output in the cw regime. Based on the model, we designed different input/output mirrors to achieve the highest output Stokes power. Experimental results show that our designs were quite close to the theoretical limit. During the experiments, we gained experience of aligning and adjusting the laser so that we have a further understanding of factors influencing the performance of pump resonant lasers.

For the pump resonant vanadate Raman laser, with the aid of the model, we designed and built a laser that reached the second Stokes output with imperfect continuous wave output. We explored and improved the stabilization of the laser output by reducing the thermal lensing effect by using a larger spot size. Troubleshooting of the pump power coupling problem revealed an issue with the linewidth of the pump source being too large. This section of work was most affected by the COVID situation, with the SolsTiS laser that we wanted to use being broken, and the replacement experiments being quite disrupted.

Meanwhile, in the diamond Raman ring cavity laser, we observed the SLM operation of second Stokes field, which is the first time this was seen in a ring cavity. The counter-propagation of laser fields in the cavity effectively suppresses noise transfer between fields, which encourages the SLM lasing. We did not have perfect unidirectional counter-



propagation which we attributed to insufficient leakage through the feedback mirror which made the SLM operation limited to the low second Stokes power regime.

We also explored the use of sum-frequency mixing to use an axial mode suppression method to achieve SLM operation in a standing wave cavity. We built a linear cavity under quite noisy environmental conditions that operated multimode. We inserted an LBO crystal to convert portion of the Stokes through SHG, and by tuning the phase matching of the LBO, we investigated the conditions leading to SLM Stokes output. The results show the generation of SHG suppresses axial modes and we observed stable SLM operation Stokes output of 4.3 W for 1.26 W of SHG (about 23% of total out coupled power).

## 6.2 Implications and future work

### 6.2.1 Raman laser model

In chapter 2 we compare the pump resonant Raman laser model and external cavity Raman laser model and find the outstanding output performance of the pump resonant Raman laser, not only for smaller pump powers, but also at quite high pump powers when the external cavity lasers are well above threshold. However, the model is only valid in the low power regime, and in this comparison we are at the edge of its validity. Given resonant lasers seem useful at much higher pump powers than we thought, it is necessary to expand the model to the high-power regime, to further compare the performance of the ring cavity laser and external cavity Raman laser. This can provide further guidance for the design of the ring cavity under higher pump powers.

Another area still not fully understood is the oscillation of the a high number of longitudinal modes in various scenarios. Basic theory dictates that due to a lack of spatial hole burning, a single longitudinal mode should oscillate and be stable, however, that is obviously not the case. Our experimental data add to the evidence found with externally pumped Raman lasers, which suggests that the hole burning free Raman gain is not sufficient to keep the SLM operation, especially at higher powers, and other axial mode suppressing

techniques are required. We also cannot fully explain how the counter-propagation of laser fields suppresses noise, and helps to achieve SLM operation, nor why this collapses when the output power reaches some threshold. As same unexplained multimode operation is seen in external cavity lasers, the fact that counter propagation helps may give a clue that four-wave mixing plays a role once the fields are multimode, but the first step from single mode to multimode is still unexplained. Environmental noise and thermal instability may be important factors, but it is not clear that SLM operation would be maintained if stability could be achieved and further research is required.

### 6.2.2 SLM operation of Raman laser

In chapter 5 we achieved SLM Stokes operation in a linear cavity by using LBO to suppress axial modes via SHG. So far there is only a phenomenological explanation of the axial suppression effect due to SHG. A quantitative model, which can help us measure the axial mode suppression strength, is still to be done. Meanwhile, a standard of evaluation of the “SLM stability” is needed, as we can only simply classify a laser as “single mode” and “multi-mode” at present, which does not sufficiently distinguish between a single mode quickly changing position and frequency, and simultaneous lasing of multiple modes. As the next step, we will develop a model to quantitatively measure the strength of the axial suppression to explore the relationship between the LBO power and power distribution among longitudinal modes.

For the ring cavity, it is necessary to further explore the mechanism which encourages SLM operation when using counter-propagating fields. We can change the relative directions of pump field, first Stokes and second Stokes field, to investigate the modes behavior. We can also monitor the noise transfer between these modes, try to study the relationship between noise transfer and SLM control. The axial suppression effect of SHG can also be applied in the ring system. However, it may induce new complexities in the fields and compete with the mechanism counter-propagating the pump and Stokes fields.

### 6.2.3 Stabilization of Raman lasers

The stabilization of lasers is crucial for their commercialization. The lasers we studied in this thesis, the temporal stability of the output power cannot be called excellent. For a ring cavity, the stability of the output power depends on the locking configuration, which is sensitive to the surroundings. Furthermore, the pump source also needs precise linewidth stabilization to ensure good and reliable coupling into the cavity. In the case of the linear cavity, the resonator was not actively stabilized, which certainly impacted the output performance. This highlights the fact that even for non-resonant lasers, it is likely that active cavity stabilization will be necessary regardless, and so we may as well design resonant lasers.

One mechanism we can think about for the stabilization of output power is the Stokes clamping effect: by generating a higher order Stokes field, the Stokes field pumping it can be clamped, which was observed and mentioned in chapter 4. This could act as a power stabilizing method.

The frequency linewidth and stabilization at the MHz level and below was unknown during the experiments in the project, due to the lack of a measuring equipment. We could only monitor the SLM operation with a F-P interferometer with a 70MHz resolution. For further investigation and modelling of laser stabilization and SLM mechanisms, it is necessary to measure the linewidth of the lasing mode and quantitatively evaluate the effects of the methods leading to SLM operation.

## 6.3 Closing words

In summary, the achievements demonstrated in this PhD thesis are milestones on the way to fill the knowledge gaps in the areas of pump resonant Raman laser and SLM operation in Raman laser. Our models will guide future development of lasers. We have made advances here, and generated new questions and guidance for the Raman laser technologies in the future.



## General effective area derivation

In Chapter 1, we derived the equations that predict exponential gain for the Stokes field. These equations deal with intensity, but in real lasers we want to deal with beam power, and so we need to consider the transverse extent of the beams. In practice, especially when laser incident into the diamond with Brewster's angle, the beam shape will be an ellipse, while the confocal length of the focus may be comparable to the length of the Raman medium. We need a way to describe the power gain of a real beam through a crystal.

We start with the equation (1-31) for Stokes gain:

$$\frac{dI_s(r,z)}{dz} = g_s I_p I_s - \alpha I_s, \quad (\text{A-1})$$

where  $r$  is the radial coordinate,  $z$  is the propagation coordinate,  $g_s I_p I_s$  is the gain of Stokes while  $\alpha I_s$  is the loss of Stokes. By using relation that beam power  $P = \int I dA$ , we get

$$\frac{dP_s(z)}{dz} = g_s \int I_p I_s dA - \alpha P_s, \quad (\text{A-2})$$

$$\frac{dP_s(z)}{dz} = \left( g_s \int \bar{I}_p \bar{I}_s dA P_p \right) P_s - \alpha P_s, \quad (\text{A-3})$$

where  $\bar{I}$  is a normalized intensity profile. Defining the Stokes gain as  $g_s P_p / A_{eff}$  we find an effective beam area

$$A_{eff} = \frac{1}{\int \bar{I}_p \bar{I}_s dA}. \quad (\text{A-4})$$

Assuming the transverse mode of beams are all TEM<sub>00</sub>, from the TEM<sub>00</sub> equation

$$I_{P,S}(r, z) = P_{P,S} \frac{2}{\pi} \frac{1}{\omega_{P,S}^2(z)} \exp[-2(\frac{r}{\omega_{P,S}(z)})^2], \quad (\text{A-5})$$

we can extract the form  $I_{P,S} = \overline{I_{P,S}} * P_{P,S}$  to get

$$\overline{I_{P,S}(r, z)} = \frac{2}{\pi} \frac{1}{\omega_{P,S}^2(z)} \exp[-2(\frac{r}{\omega_{P,S}(z)})^2]. \quad (\text{A-6})$$

Note that the eq. (A-6) is only fit for circle beam shapes. The equation for elliptical beams is:

$$\overline{I_{P,S}(r, z)} = \frac{2}{\pi} \frac{1}{\omega_{Px,Sx}(z) * \omega_{Py,Sy}(z)} \exp(-2(\frac{x^2}{\omega_{Px,Sx}(z) * \omega_{Px,Sx}(z)} + \frac{y^2}{\omega_{Py,Sy}(z) * \omega_{Py,Sy}(z)})). \quad (\text{A-7})$$

Diffraction of Gaussian beams give the development of spot size with distance as:

$$\omega_{P,S}(z) = \omega_{P,S}(0) \sqrt{1 + (\frac{z}{z_{p,s}})^2}, \quad (\text{A-8})$$

where  $\omega_{P,S}(0)$  is the waist radius of beam, and  $z_{p,s}$  is respective Rayleigh range defined as

$$z_{p,s} = \frac{\pi n_{P,S} \omega_{P,S}^2(0)}{M_{P,S}^2 \lambda_{P,S}}. \quad (\text{A-9})$$

We now have enough information to calculate  $A_{eff}$ , from which we can predict power gain for Stokes and pump beams with different spot sizes. This can be a calculated numerically, or there are simple cases: particularly, if the beams are circular, the Stokes beam and pump beam have the same confocal parameter  $b_P = b_S = b$  (which is valid when they share the same cavity). When integrating the Eq. (A-3), we can get

$$[\ln(P_S(L)) - \ln(P_S(0))] = \left( \frac{g_S^{PP}}{A_{eff}} - \alpha \right) L. \quad (\text{A-10})$$

Here the  $A_{eff}$  is the average value as

$$\frac{1}{A_{eff}} = \frac{1}{A_{efocus}} \left( \frac{b}{L} \tan^{-1} \frac{L}{b} \right), \quad (\text{A-11})$$

where  $A_{efocus}$  is the effective area in the focal plane, and  $L$  is the crystal length. For tight focusing,  $b \ll L$ , the bracket of Eq. (A-11) is close to  $\pi b / (2L)$ , For loose focusing,  $b \gg L$ , the correction factor in the bracket of Eq. (A-11) is unity, and the beams passing through the crystal can be regard as the collimated beam, the Eq. (A-11) is further simplified as

$$A_{eff} = \frac{\pi}{2} (\omega_P^2 + \omega_S^2), \quad (\text{A-12})$$

# B

## List of Publications

This appendix includes the following list of all publications and conference presentations that I have authored/co-authored during this PhD project:

### Journal articles

1. M. Li, O. Kitzler, R. P. Mildren, and D. J. Spence, "Modelling and characterisation of continuous wave resonantly pumped diamond Raman lasers," *Opt. Express* 29(12), 18427 (2021).
2. M. Li, O. Kitzler, and D. J. Spence, "Investigating single-longitudinal-mode operation of a continuous wave second Stokes diamond Raman ring laser," *Opt. Express* 28(2), 1738 (2020).

### Conference presentations

3. M. Li, O. Kitzler, and D. Spence, "Continuous Wave Resonantly Pumped Second Stokes Diamond Raman Laser," 2020 Conf. Lasers Electro-Optics Pacific Rim, CLEO-PR 2020 - Proc. 6–7 (2020). *Oral presentation*
4. O. Kitzler, M. Li, and D. J. Spence, "High Raman gain directions in diamond," 2020 Conf. Lasers Electro-Optics Pacific Rim, CLEO-PR 2020 - Proc. 110–111 (2020). *Poster presentation*

Appendix B of this thesis has been removed as it contains published material. Please refer to the following citations for details of the articles contained in these pages.

Li, M., Kitzler, O., Mildren, R. P., & Spence, D. J. (2021). Modelling and characterisation of continuous wave resonantly pumped diamond Raman lasers. *Optics Express*, 29(12), 18427-18436.

DOI: [10.1364/OE.426067](https://doi.org/10.1364/OE.426067)

Li, M., Kitzler, O., & Spence, D. J. (2020). Investigating single-longitudinal-mode operation of a continuous wave second Stokes diamond Raman ring laser. *Optics Express*, 28(2), 1738-1744.

DOI: [10.1364/OE.380644](https://doi.org/10.1364/OE.380644)

## References

1. T. H. MAIMAN, "Stimulated Optical Radiation in Ruby," *Nature* **187**(4736), 493–494 (1960).
2. M. A. Wulder, J. C. White, R. F. Nelson, E. Næsset, H. O. Ørka, N. C. Coops, T. Hilker, C. W. Bater, and T. Gobakken, "Lidar sampling for large-area forest characterization: A review," *Remote Sens. Environ.* **121**, 196–209 (2012).
3. G. Chryssolouris, N. Anifantis, and S. Karagiannis, "Laser assisted machining: An overview," *J. Manuf. Sci. Eng. Trans. ASME* **119**(4B), 766–769 (1997).
4. D. Radtke and U. D. Zeitner, "Laser-lithography on non-planar surfaces," *Opt. Express* **15**(3), 1167 (2007).
5. D. C. Hanna, "Foundations of laser spectroscopy," *Opt. Laser Technol.* **16**(6), 325–326 (1984).
6. H.-E. Albrecht, M. Borys, N. Damaschke, and C. Tropea, *Laser Doppler and Phase Doppler Measurement Techniques* (Springer Berlin Heidelberg, 2003), **114**.
7. P. F. Moulton, "Spectroscopic and laser characteristics of Ti:Al<sub>2</sub>O<sub>3</sub>," *J. Opt. Soc. Am. B* **3**(1), 125 (1986).
8. H. M. Pask, D. C. Hanna, A. C. Tropper, C. J. Mackechnie, P. R. Barber, J. M. Dawes, and R. J. Carman, "Ytterbium-Doped Silica Fiber Lasers: Versatile Sources for the 1–1.2  $\mu\text{m}$  Region," *IEEE J. Sel. Top. Quantum Electron.* **1**(1), 2–13 (1995).
9. J. A. Giordmaine and R. C. Miller, "Optical Parametric Oscillators," *IEEE J. Quantum Electron.* **2**(4), 106 (1966).
10. M. Ebrahim-Zadeh, S. C. Kumar, A. Esteban-Martin, and G. K. Samanta, "Breakthroughs in photonics 2012: Breakthroughs in optical parametric oscillators," *IEEE Photonics J.* **5**(2), 700105 (2013).
11. G. Eckhardt, R. W. Hellwarth, F. J. McClung, S. E. Schwarz, D. Weiner, and E. J. Woodbury, "Stimulated Raman Scattering From Organic Liquids," *Phys. Rev. Lett.* **9**(11), 455–457 (1962).
12. A. Penzkofer, A. Laubereau, and W. Kaiser, "High intensity Raman interactions," *Prog. Quantum Electron.* **6**(2), 55–140 (1979).
13. J. T. Murray, W. L. Austin, and R. C. Powell, "Intracavity Raman conversion and Raman beam cleanup," *Opt. Mater. (Amst.)* **11**(4), 353–371 (1999).
14. L. Schoulepnikoff and V. Mitev, "High-gain single-pass stimulated Raman scattering and four-wave mixing in a focused beam geometry: A numerical study," *Pure Appl. Opt. (Print Ed. (United Kingdom))* **6**(2), 277–302 (1997).



15. R. W. Boyd, *Nonlinear Optics, Third Edition*, 3rd ed. (Academic Press, Inc., 2008).
16. J. Brandmüller, "Rayleigh-Streuung und Rotations-Raman-Effekt von Flüssigkeiten," *Zeitschrift für Phys.* **140**(1), 75–91 (1955).
17. R. L. Sutherland, *Handbook of Nonlinear Optics*, 2nd ed. (CRC Press, 2003).
18. O. Kitzler, A. McKay, D. J. Spence, and R. P. Mildren, "Modelling and optimization of continuous-wave external cavity Raman lasers," *Opt. Express* **23**(7), 8590 (2015).
19. S. Ding, X. Zhang, Q. Wang, F. Su, S. Li, S. Fan, S. Zhang, J. Chang, S. Wang, and Y. Liu, "Theoretical models for the extracavity Raman laser with crystalline Raman medium," *Appl. Phys. B Lasers Opt.* **85**(1), 89–95 (2006).
20. D. J. Spence, P. Dekker, and H. M. Pask, "Modeling of continuous wave intracavity Raman lasers," *IEEE J. Sel. Top. QUANTUM Electron.* **13**(3), 756–763 (2007).
21. S. Ding, X. Zhang, Q. Wang, J. Chang, S. Wang, and Y. Liu, "Modeling of actively Q-switched intracavity Raman lasers," *IEEE J. Quantum Electron.* **43**(8), 722–729 (2007).
22. J. H. Liu, U. Griebner, V. Petrov, H. J. Zhang, J. X. Zhang, and J. Y. Wang, "Efficient continuous-wave and Q-switched operation of a diode-pumped Yb : KLu(WO<sub>4</sub>)<sub>2</sub> laser with self-Raman conversion," *Opt. Lett.* **30**(18), 2427–2429 (2005).
23. A. A. Demidovich, A. S. Grabtchikov, V. A. Lisinetskii, V. N. Burakevich, V. A. Orlovich, and W. Kiefer, "Continuous-wave Raman generation in a diode-pumped Nd<sup>3+</sup>:KGd(WO<sub>4</sub>)<sub>2</sub> laser," *Opt. Lett.* **30**(13), 1701 (2005).
24. A. J. Lee, D. J. Spence, J. A. Piper, and H. M. Pask, "A wavelength-versatile, continuous-wave, self-Raman solid-state laser operating in the visible," *Opt. Express* **18**(19), 20013 (2010).
25. P. Dekker, H. M. Pask, D. J. Spence, and J. A. Piper, "Continuous-wave, intracavity doubled, self-Raman laser operation in Nd:GdVO<sub>4</sub> at 586.5 nm," *Opt. Express* **15**(11), 7038 (2007).
26. P. Dekker, H. M. Pask, and J. A. Piper, "All-solid-state 704 mW continuous-wave yellow source based on an intracavity, frequency-doubled crystalline Raman laser," *Opt. Lett.* **32**(9), 1114–1116 (2007).
27. A. J. Lee, H. M. Pask, J. A. Piper, H. Zhang, and J. Wang, "An intracavity, frequency-doubled BaWO<sub>4</sub> Raman laser generating multi-watt continuous-wave, yellow emission," *Opt. Express* **18**(6), 5984 (2010).
28. A. J. Lee, H. M. Pask, D. J. Spence, and J. a Piper, "Efficient 5.3 W cw laser at 559 nm by intracavity frequency summation of fundamental and first-Stokes wavelengths in a self-Raman Nd:GdVO<sub>4</sub> laser," *Opt. Lett.* **35**(5), 682–684 (2010).
29. J. T. Murray, D. Smith, R. A. Stolzenberger, W. Austin, R. C. Powell, and N. Peyghambarian, "Generation of 1.5-μm radiation through intracavity solid-state Raman shifting in Ba(NO<sub>3</sub>)<sub>2</sub> nonlinear crystals," *Opt. Lett.* **20**(9), 1017 (1995).
30. J. A. Piper and H. M. Pask, "Crystalline Raman lasers," *IEEE J. Sel. Top. Quantum Electron.* **13**(3), 692–704 (2007).
31. H. M. Pask, "The design and operation of solid-state Raman lasers," *Prog. Quantum Electron.* **27**(1), 3–56 (2003).
32. A. S. Grabtchikov, V. A. Lisinetskii, V. A. Orlovich, M. Schmitt, R. Maksimenka, and W. Kiefer, "Multimode pumped continuous-wave solid-state Raman laser," *Opt. Lett.* **29**(21), 2524 (2004).
33. C. A. Yuk-Sun, Y. Jing-Guo, and C. Mau-Hing, "High Efficiency Pulse Acetone Liquid Raman Laser Using DCM Fluorescent Dye as the Enhancement Medium," *Chinese Phys. Lett.* **23**(1), 135–138 (2006).
34. H. B. Wang, H. M. Liang, Z. H. Wang, S. R. Luo, J. G. Yang, W. G. Zheng, X. F. Wei, S. B. He, and Y. Bin

- Chen, "High efficient C<sub>6</sub>H<sub>12</sub> raman laser enhanced by DCM fluorescence," *Chinese Phys. Lett.* **24**(1), 119–122 (2007).
35. J. K. Brasseur, R. F. Teehan, P. A. Roos, B. Soucy, D. K. Neumann, and J. L. Carlsten, "High-power deuterium Raman laser at 632 nm," *Appl. Opt.* **43**(5), 1162–1166 (2004).
  36. J. K. Brasseur, K. S. Repasky, and J. L. Carlsten, "Continuous-wave Raman laser in H<sub>2</sub>," *Opt. Lett.* **23**(5), 367 (1998).
  37. K. S. Repasky, J. K. Brasseur, L. Meng, and J. L. Carlsten, "Performance and design of an off-resonant continuous-wave Raman laser," *J. Opt. Soc. Am. B-OPTICAL Phys.* **15**(6), 1667–1673 (1998).
  38. Y. Wang, M. K. Dasa, A. I. Adamu, J. E. Antonio-Lopez, M. S. Habib, R. Amezcua-Correa, O. Bang, and C. Markos, "High pulse energy and quantum efficiency mid-infrared gas Raman fiber laser targeting CO<sub>2</sub> absorption at 4.2  $\mu$ m," *Opt. Lett.* **45**(7), 1938 (2020).
  39. F. Couny, B. J. Mangan, A. V. Sokolov, and F. Benabid, "High power 55 watts CW Raman fiber-gas-laser," *Opt. InfoBase Conf. Pap.* 3–4 (2010).
  40. V. R. Supradeepa, Y. Feng, and J. W. Nicholson, "Raman fiber lasers," *J. Opt. (United Kingdom)* **19**(2), (2017).
  41. E. A. Zlobina, "Multimode Fiber Raman Lasers Directly Pumped by Laser Diodes," **24**(3), (2018).
  42. Y. Shamir, Y. Glick, M. Aviel, A. Attias, and S. Pearl, "250 W clad pumped Raman all-fiber laser with brightness enhancement," *Opt. Lett.* **43**(4), 711 (2018).
  43. N. Optical and C. A. Complete, "Rarely Used and Archive Crystals," in *Nonlinear Optical Crystals: A Complete Survey* (Springer-Verlag, 2005), pp. 319–398.
  44. Jones. J. D. C. Webb C., *Handbook of Laser Technology and Applications*, 1st ed. (CRC Press, 2020).
  45. A. A. Kaminskii, H. J. Eichler, K. Ueda, N. V. Klassen, B. S. Redkin, L. E. Li, J. Findeisen, D. Jaque, J. García-Sole, J. Fernández, and R. Balda, "Properties of Nd<sup>3+</sup>-doped and undoped tetragonal PbWO<sub>4</sub>, NaY(WO<sub>4</sub>)<sub>2</sub>, CaWO<sub>4</sub>, and undoped monoclinic ZnWO<sub>4</sub> and CdWO<sub>4</sub> as laser-active and stimulated Raman scattering-active crystals," *Appl. Opt.* **38**(21), 4533 (1999).
  46. P. G. Zverev, T. T. Basiev, V. V. Osiko, A. M. Kulkov, V. N. Voitsekhovskii, and V. E. Yakobson, "Physical, chemical and optical properties of barium nitrate Raman crystal," *Opt. Mater. (Amst.)* **11**(4), 315–334 (1999).
  47. T. T. Basiev, A. A. Sobol, P. G. Zverev, V. V. Osiko, and R. C. Powell, "Comparative spontaneous Raman spectroscopy of crystals for Raman lasers," *Appl. Opt.* **38**(3), 594 (1999).
  48. I. V. Mochalov, "Laser and nonlinear properties of the potassium gadolinium tungstate laser crystal KGd(WO<sub>4</sub>)<sub>2</sub>:Nd<sup>3+</sup>-(KGW:Nd)," *Opt. Eng.* **36**(6), 1660 (1997).
  49. A. A. Kaminskii, K. ichi Ueda, H. J. Eichler, Y. Kuwano, H. Kouta, S. N. Bagaev, T. H. Chyba, J. C. Barnes, G. M. A. Gad, T. Murai, and J. Lu, "Tetragonal vanadates YVO<sub>4</sub> and GdVO<sub>4</sub> - New efficient  $\chi^{(3)}$ -materials for Raman lasers," *Opt. Commun.* **194**(1–3), 201–206 (2001).
  50. P. G. Zverev, A. Y. Karasik, A. A. Sobol, D. S. Chunaev, T. T. Basiev, A. I. Zagumennyi, Y. D. Zavartsev, S. A. Kutovoi, V. V. Osiko, and I. A. Shcherbakov, "Stimulated Raman Scattering of picosecond pulses in GdVO<sub>4</sub> and YVO<sub>4</sub> crystals," *TuB10* (2014).
  51. T. T. Basiev, "New crystals for raman lasers," *Phys. Solid State* **47**(8), 1400–1405 (2005).
  52. W. Ge, H. Zhang, J. Wang, J. Liu, H. Li, X. Cheng, H. Xu, X. Xu, X. Hu, and M. Jiang, "The thermal and optical properties of BaWO<sub>4</sub> single crystal," *J. Cryst. Growth* **276**(1–2), 208–214 (2005).
  53. G. M. Bonner, H. M. Pask, A. J. Lee, A. J. Kemp, J. Wang, H. Zhang, and T. Omatsu, "Measurement of thermal lensing in a CW BaWO<sub>4</sub> intracavity Raman laser," *Opt. Express* **20**(9), 9810 (2012).
  54. R. P. Mildren, "Intrinsic Optical Properties of Diamond," in *Optical Engineering of Diamond* (John

Wiley & Sons, Ltd, 2013), pp. 1–34.

55. I. Friel, S. L. Geoghegan, D. J. Twitchen, and G. A. Scarsbrook, "Development of high quality single crystal diamond for novel laser applications," in *Optics and Photonics for Counterterrorism and Crime Fighting VI and Optical Materials in Defence Systems Technology VII*, C. Lewis, D. Burgess, R. Zamboni, F. Kajzar, and E. M. Heckman, eds. (2010), **7838**, p. 783819.
56. A. A. Kaminskii, V. G. Ralchenko, and V. I. Konov, "Observation of stimulated raman scattering in CVD-diamond," *JETP Lett.* **80**(4), 267–270 (2004).
57. M. Jelínek, O. Kitzler, H. Jelínková, J. Šulc, and M. Němec, "CVD-diamond external cavity nanosecond Raman laser operating at 1.63  $\mu\text{m}$  pumped by 1.34  $\mu\text{m}$  Nd: YAP laser," *Laser Phys. Lett.* **9**(1), 35–38 (2012).
58. A. McKay, O. Kitzler, H. Liu, D. Fell, and R. P. Mildren, "High average power (11 W) eye-safe diamond Raman laser," *High-Power Lasers Appl. VI* **8551**(November 2012), 85510U (2012).
59. A. McKay, H. Liu, O. Kitzler, and R. P. Mildren, "An efficient 14.5 W diamond Raman laser at high pulse repetition rate with first (1240 nm) and second (1485 nm) Stokes output," *Laser Phys. Lett.* **10**(10), (2013).
60. A. M. Warrier, J. Lin, H. M. Pask, R. P. Mildren, D. W. Coutts, and D. J. Spence, "Highly efficient picosecond diamond Raman laser at 1240 and 1485 nm," *Opt. Express* **22**(3), 3325 (2014).
61. M. Murtagh, J. Lin, R. P. Mildren, and D. J. Spence, "Ti:sapphire-pumped diamond Raman laser with sub-100-fs pulse duration," *Opt. Lett.* **39**(10), 2975 (2014).
62. E. Granados, D. J. Spence, and R. P. Mildren, "Deep ultraviolet diamond Raman laser," *Opt. Express* **19**(11), 10857 (2011).
63. J. Nikkinen, A. Härkönen, and M. Guina, "Sub-50 ps pulses at 620 nm obtained from frequency doubled 1240 nm diamond Raman laser," *Opt. Express* **25**(24), 30365 (2017).
64. V. P. Pashinin, V. G. Ralchenko, A. P. Bolshakov, E. E. Ashkinazi, and V. I. Konov, "Diamond Raman laser emitting at 1194, 1419, and 597 nm," *Quantum Electron.* **48**(3), 201–205 (2018).
65. A. Sabella, J. A. Piper, and R. P. Mildren, "Diamond Raman laser with continuously tunable output from 3.38 to 3.80  $\mu\text{m}$ ," *Opt. Lett.* **39**(13), 4037 (2014).
66. K. Chrysalidis, V. N. Fedosseev, B. A. Marsh, R. P. Mildren, D. J. Spence, K. D. A. Wendt, S. G. Wilkins, and E. Granados, "Continuously tunable diamond Raman laser for resonance laser ionization," *Opt. Lett.* **44**(16), 3924 (2019).
67. A. McKay, O. Kitzler, and R. P. Mildren, "Simultaneous brightness enhancement and wavelength conversion to the eye-safe region in a high-power diamond Raman laser," *Laser Photonics Rev.* **8**(3), 37–41 (2014).
68. Z. Bai, R. J. Williams, H. Jasbeer, S. Sarang, O. Kitzler, A. McKay, and R. P. Mildren, "Large brightness enhancement for quasi-continuous beams by diamond Raman laser conversion," *Opt. Lett.* **43**(3), 563 (2018).
69. H. Jasbeer, R. J. Williams, O. Kitzler, A. McKay, and R. P. Mildren, "Wavelength diversification of high-power external cavity diamond Raman lasers using intracavity harmonic generation," *Opt. Express* **26**(2), 1930 (2018).
70. Z. Bai, R. J. Williams, O. Kitzler, S. Sarang, D. J. Spence, and R. P. Mildren, "302 W quasi-continuous cascaded diamond Raman laser at 1.5 microns with large brightness enhancement," *Opt. Express* **26**(16), 19797 (2018).
71. A. McKay, R. P. Mildren, D. W. Coutts, and D. J. Spence, "SRS in the strong-focusing regime for Raman amplifiers," *Opt. Express* **23**(11), 15012 (2015).

72. G. Demetriou, A. J. Kemp, and V. Savitski, "100 kW peak power external cavity diamond Raman laser at 2.52  $\mu\text{m}$ ," *Opt. Express* **27**(7), 10296 (2019).
73. S. Reilly, V. G. Savitski, H. Liu, E. Gu, M. D. Dawson, and A. J. Kemp, "Monolithic diamond Raman laser," *Opt. Lett.* **40**(6), 930 (2015).
74. V. G. Savitski, G. Demetriou, S. Reilly, H. Liu, E. Gu, M. D. Dawson, and A. J. Kemp, "Energy scaling, second stokes oscillation, and raman gain-guiding in monolithic diamond raman lasers," *IEEE J. Quantum Electron.* **54**(6), 1–8 (2018).
75. J. Trägårdh, M. Murtagh, G. Robb, M. Parsons, J. Lin, D. J. Spence, and G. McConnell, "Two-color, two-photon imaging at long excitation wavelengths using a diamond raman laser," *Microsc. Microanal.* **22**(4), 803–807 (2016).
76. A. McKay, D. J. Spence, D. W. Coutts, and R. P. Mildren, "Diamond-based concept for combining beams at very high average powers," *Laser Photonics Rev.* **11**(3), (2017).
77. O. Kitzler, A. McKay, and R. P. Mildren, "Continuous-wave wavelength conversion for high-power applications using an external cavity diamond Raman laser," *Opt. Lett.* **37**(14), 2790 (2012).
78. R. J. Williams, O. Kitzler, A. McKay, and R. P. Mildren, "Investigating diamond Raman lasers at the 100 W level using quasi-continuous-wave pumping," *Opt. Lett.* **39**(14), 4152 (2014).
79. R. J. Williams, J. Nold, M. Strecker, O. Kitzler, A. McKay, T. Schreiber, and R. P. Mildren, "Efficient Raman frequency conversion of high-power fiber lasers in diamond," *Laser Photon. Rev.* **9**(4), 405–411 (2015).
80. R. J. Williams, D. J. Spence, O. Lux, and R. P. Mildren, "High-power continuous-wave Raman frequency conversion from 1.06  $\mu\text{m}$  to 1.49  $\mu\text{m}$  in diamond," *Opt. Express* **25**(2), 749 (2017).
81. S. Antipov, A. Sabella, R. J. Williams, O. Kitzler, D. J. Spence, and R. P. Mildren, "1.2 kW quasi-steady-state diamond Raman laser pumped by an  $M^2 = 15$  beam," *Opt. Lett.* **44**(10), 2506 (2019).
82. S. Antipov, R. J. Williams, A. Sabella, O. Kitzler, A. Berhane, D. J. Spence, and R. P. Mildren, "Analysis of a thermal lens in a diamond Raman laser operating at 1.1 kW output power," *Opt. Express* **28**(10), 15232 (2020).
83. M. Heinzig, G. Palma-Vega, T. Walbaum, T. Schreiber, R. Eberhardt, and A. Tünnermann, "Diamond Raman oscillator operating at 1178 nm," *Opt. Lett.* **45**(10), 2898 (2020).
84. D. C. Parrotta, A. J. Kemp, M. D. Dawson, and J. E. Hastie, "Multiwatt, Continuous-Wave, Tunable Diamond Raman Laser With Intracavity Frequency-Doubling to the Visible Region," *IEEE J. Sel. Top. Quantum Electron.* **19**(4), 1400108–1400108 (2013).
85. R. Casula, J.-P. Penttinen, A. J. Kemp, M. Guina, and J. E. Hastie, "1.4  $\mu\text{m}$  continuous-wave diamond Raman laser," *Opt. Express* **25**(25), 31377 (2017).
86. O. Lux, S. Sarang, R. J. Williams, A. McKay, and R. P. Mildren, "Single longitudinal mode diamond Raman laser in the eye-safe spectral region for water vapor detection," *Opt. Express* **24**(24), 27812 (2016).
87. C. G. Carlson, P. D. Dragic, R. K. Price, J. J. Coleman, and G. R. Swenson, "A narrow-linewidth, Yb fiber-amplifier-based upper atmospheric Doppler temperature lidar," *IEEE J. Sel. Top. Quantum Electron.* **15**(2), 451–461 (2009).
88. P. W. Milonni, R. Q. Fugate, and J. M. Telle, "Analysis of measured photon returns from sodium beacons," *J. Opt. Soc. Am. A* **15**(1), 217 (1998).
89. X. Yang, O. Kitzler, D. J. Spence, Z. Bai, Y. Feng, and R. P. Mildren, "Diamond Sodium Guide Star Laser," 2020 Conf. Lasers Electro-Optics Pacific Rim, CLEO-PR 2020 - Proc. **45**(7), 1898–1901 (2020).
90. D. J. Wineland and W. M. Itano, "Laser cooling of atoms," *Phys. Rev. A* **20**(4), 1521–1540 (1979).

91. R. Yamamoto, J. Kobayashi, T. Kuno, K. Kato, and Y. Takahashi, "An ytterbium quantum gas microscope with narrow-line laser cooling," *New J. Phys.* **18**(2), (2016).
92. J. E. Curtis, B. A. Koss, and D. G. Grier, "Dynamic holographic optical tweezers," *Opt. Commun.* **207**(1–6), 169–175 (2002).
93. Y. Nishigata, C.-Y. Lee, Y. Miyamoto, K. Miyamoto, Y.-F. Chen, and T. Omatsu, "Optical vortex pumped solid-state Raman laser," *Solid State Lasers XXVI Technol. Devices* **10082**(February 2017), 1008203 (2017).
94. A. Sabella, D. J. Spence, and R. P. Mildren, "Pump-Probe Measurements of the Raman Gain Coefficient in Crystals Using Multi-Longitudinal-Mode Beams," *IEEE J. Quantum Electron.* **51**(12), (2015).
95. O. Lux, S. Sarang, O. Kitzler, D. J. Spence, and R. P. Mildren, "Intrinsically stable high-power single longitudinal mode laser using spatial hole burning free gain," *Optica* **3**(8), 876 (2016).
96. S. Sarang, O. Kitzler, O. Lux, Z. Bai, R. J. Williams, D. J. Spence, and R. P. Mildren, "Single-longitudinal-mode diamond laser stabilization using polarization-dependent Raman gain," *OSA Contin.* **2**(4), 1028 (2019).
97. T. W. Hänsch and B. Couillaud, "Laser frequency stabilization by polarization spectroscopy of a reference cavity," *Opt. Commun.* **35**(3), 441–444 (1980).
98. O. Kitzler, J. Lin, H. M. Pask, R. P. Mildren, S. C. Webster, N. Hempler, G. P. A. Malcolm, and D. J. Spence, "Single-longitudinal-mode ring diamond Raman laser," *Opt. Lett.* **42**(7), 1229 (2017).
99. X. Yang, O. Kitzler, D. J. Spence, R. J. Williams, Z. Bai, S. Sarang, L. Zhang, Y. Feng, and R. P. Mildren, "Single-frequency 620 nm diamond laser at high power, stabilized via harmonic self-suppression and spatial-hole-burning-free gain," *Opt. Lett.* **44**(4), 839 (2019).
100. K. I. Martin, W. A. Clarkson, and D. C. Hanna, "Self-suppression of axial mode hopping by intracavity second-harmonic generation," *Opt. Lett.* **22**(6), 375 (1997).
101. D. J. Spence, P. Dekker, and H. M. Pask, "Modeling of Continuous Wave Intracavity Raman Lasers," *IEEE J. Sel. Top. Quantum Electron.* **13**(3), 756–763 (2007).
102. B. Min, T. J. Kippenberg, and K. J. Vahala, "Compact, fiber-compatible, cascaded Raman laser.," *Opt. Lett.* **28**(17), 1507–1509 (2003).
103. B. Feigel, H. Thienpont, and N. Vermeulen, "Modeling and design of infrared and ultraviolet integrated diamond ring Raman lasers," in *Nonlinear Optics and Its Applications IV*, B. J. Eggleton, N. G. R. Broderick, and A. L. Gaeta, eds. (2016), **9894**(April 2016), p. 989414.
104. A. E. Siegman, *Lasers* (University Science Books, 1986).
105. D. J. Spence, "Spectral effects of stimulated Raman scattering in crystals," *Prog. Quantum Electron.* **51**, 1–45 (2017).
106. J.-P. M. Feve, K. E. Shortoff, M. J. Bohn, and J. K. Brasseur, "High average power diamond Raman laser," *Opt. Express* **19**(2), 913–922 (2011).
107. G. Turri, "Optical absorption, depolarization, and scatter of epitaxial single-crystal chemical-vapor-deposited diamond at 1.064 $\mu\text{m}$ ," *Opt. Eng.* **46**(6), 064002 (2007).
108. A. Sabella, J. A. Piper, and R. P. Mildren, "1240 nm diamond Raman laser operating near the quantum limit," *Opt. Lett.* **35**(23), 3874 (2010).
109. R. W. P. Drever, J. L. Hall, F. V. Kowalski, J. Hough, G. M. Ford, A. J. Munley, and H. Ward, "Laser phase and frequency stabilization using an optical resonator," *Appl. Phys. B Photophysics Laser Chem.* **31**(2), 97–105 (1983).
110. Z. Bai, H. Yuan, Z. Liu, P. Xu, Q. Gao, R. J. Williams, O. Kitzler, R. P. Mildren, Y. Wang, and Z. Lu,

- "Stimulated Brillouin scattering materials, experimental design and applications: A review," *Opt. Mater. (Amst)*. **75**, 626–645 (2018).
111. M. Li, O. Kitzler, and D. J. Spence, "Investigating single-longitudinal-mode operation of a continuous wave second Stokes diamond Raman ring laser," *Opt. Express* **28**(2), 1738 (2020).
112. D. J. Spence, "Spectral effects of stimulated Raman scattering in crystals," *Prog. Quantum Electron.* **51**(November 2016), 1–45 (2017).
113. R. Le Targat, J. J. Zondy, and P. Lemonde, "75%-Efficiency blue generation from an intracavity PPKTP frequency doubler," *Opt. Commun.* **247**(4–6), 471–481 (2005).
114. N. Ismail, C. C. Kores, D. Geskus, and M. Pollnau, "Fabry-Pérot resonator: spectral line shapes, generic and related Airy distributions, linewidths, finesse, and performance at low or frequency-dependent reflectivity," *Opt. Express* **24**(15), 16366 (2016).
115. Q. Sheng, R. Li, A. J. Lee, D. J. Spence, and H. M. Pask, "A single-frequency intracavity Raman laser," *Opt. Express* **27**(6), 8540 (2019).
116. C. Y. Lee, C. C. Chang, P. H. Tuan, C. Y. Cho, K. F. Huang, and Y. F. Chen, "Cryogenically monolithic self-Raman lasers: observation of single-longitudinal-mode operation," *Opt. Lett.* **40**(9), 1996 (2015).
117. D. J. Spence, "Spatial and spectral effects in continuous-wave intracavity Raman lasers," *IEEE J. Sel. Top. Quantum Electron.* **21**(1), (2015).
118. Y. R. Shen, *The Principles of Nonlinear Optics* (John Wiley & Sons Inc, 2002).
119. SNLO nonlinear optics code available from A. V. Smith, AS-Photonics, Albuquerque, NM.
120. B. Feigel, H. Thienpont, and N. Vermeulen, "Modeling and design of infrared and ultraviolet integrated diamond ring Raman lasers," in *Laser Resonators and Coherent Optics: Modeling, Technology, and Applications*, B. J. Eggleton, N. G. R. Broderick, and A. L. Gaeta, eds. (2016), **1868**(August 1993), p. 989414.